Year : 2021

Steady-state anatomical and quantitative magnetic resonance imaging of the heart using RF-frequency modulated techniques

Masala Nemanja

UNIL | Université de Lausanne

Faculté de biologie et de médecine

Département de radiodiagnostic et radiologie interventionnelle,
Centre hospitalier universitaire vaudois (CHUV)

Steady-state anatomical and quantitative magnetic resonance imaging of the heart using RF-frequency-modulated techniques

Thèse de doctorat ès sciences de la vie (PhD)

présentée à la

Faculté de biologie et de médecine
de l'Université de Lausanne

par

Nemanja MASALA

Master de l'Ecole polytechnique fédérale de Lausanne (EPFL), Suisse
Bachelor de l'Université de Calgary, Canada

Jury

Prof. Françcois Bochud, Président
Prof. Matthias Stuber, Directeur de thèse
Dr Ruud van Heeswijk, Co-directeur de thèse
Prof. Dimitri Van De Ville, Expert
Prof. Oliver Bieri, Expert

Lausanne
2021

Imprimatur

Vu le rapport présenté par le jury d'examen, composé de

Président·e	Monsieur	Prof.	François	**Bochud**
Directeur·trice de thèse	Monsieur	Prof.	Matthias	**Stuber**
Co-directeur·trice	Monsieur	Dr	Ruud	**Van Heeswijk**
Expert·e·s	Monsieur	Prof.	Dimitri	**Van De Ville**
	Monsieur	Prof.	Oliver	**Bieri**

le Conseil de Faculté autorise l'impression de la thèse de

Monsieur Nemanja Masala

Master of Science en bioingénierie, EPFL - Ecole Polytechnique Fédérale de Lausanne, Suisse

intitulée

Steady-state anatomical and quantitative magnetic resonance imaging of the heart using RF-frequency-modulated techniques

Date de l'examen : 23 août 2021

Date d'émission de l'imprimatur : Lausanne, le 25 août 2021

pour le Doyen
de la Faculté de biologie et de médecine

Prof. Niko GELDNER
Directeur de l'Ecole Doctorale

They did not know it was impossible, so they did it.

ACKNOWLEDGMENTS

I have come to think of a PhD as passing a milestone rather than scaling a summit, even though in my case I would also say it changed my perspective. A previous milestone on this journey had been my internship in Zürich from 2012 to 2013, which had made me aware that there was more than just what I had grown used to. What I learned during the PhD is that you need to have the confidence, self-understanding, and self-assertion to make the journey enjoyable and fulfilling for you, regardless of the eventual destination. You can (and I did) find positives in everything to motivate you to push through, even if they are very small positives. I did not do it alone, however, and I would like to acknowledge those people who have helped me get to this point.

I would first like to thank my two supervisors, Matthias and Ruud. Matthias supervised me during the LIBRE project and guided me through the tedious revision process of the LIBRE paper. Thank you for your time and guidance, which helped me develop as a scientist and engineer, and thank you for your understanding and flexibility in the last few months of my PhD. Ruud was my supervisor during the PLANET project. Thank you for your time and mentoring, which helped me become a better MRI scientist, a better whisky connoisseur, and a better Dutchman.

I would like to thank all my other lab colleagues for their help and for all the good times at Friday beers, lab retreats, and conferences: Jérôme, Davide, Jessica, Andrew, Chris, Jean, Emeline, Roberto, Lorenzo, John, Veronica, Simone, Mariana, Adèle, Giulia, Ludovica, Eleonora, Aurélien, Mario, Eliane, Lionel, Hélène (who also helped me with translating parts of the thesis to French), Solange, Pauline, and Simon. I want to single out Lionel, Solange, and Jean for being there to listen. Thanks to all the other colleagues in the open space and elsewhere over the years for the coffee breaks, drinks, and parties.

I want to thank the following people for enlightening discussions and help on the PLANET project in addition to those with Matthias and Ruud: Jérôme, Chris, Aurélien,

The quotation on the previous page was one I had seen in a hallway during my undergraduate studies at the University of Calgary, and it stayed with me. It nicely summarizes the mindset I have found one should have in engineering research, especially as a PhD student. It was retrieved from *https://www.buboquote.com/en/quote/5204-twain-they-did-not-know-it-was-impossible-so-they-did-it* on September 9th, 2021, and is widely attributed to Mark Twain although without a source.

ABSTRACT

Cardiovascular disease (CVD) is the leading cause of death in the United States and Europe and generates healthcare costs of hundreds of billions of dollars annually. Conventional methods of diagnosing CVD are often invasive and carry risks for the patient. For example, the gold standard for diagnosing coronary artery disease, a major class of CVD, is x-ray coronary angiography, which has the disadvantages of being invasive, being expensive, using ionizing radiation, and having a risk of complications. Conversely, coronary MR angiography (MRA) does not use ionizing radiation, can effectively visualize tissues without the need for exogenous contrast agents, and benefits from an adaptable temporal resolution. However, the acquisition time of cardiac MRI is far longer than the temporal scales of cardiac and respiratory motion, necessitating some method of compensating for this motion. The free-running framework is a novel development in our lab, benefitting from advances over the past three decades, that attempts to address disadvantages of previous cardiac MRI approaches: it provides fully self-gated 5D cardiac MRI with a simplified workflow, improved ease-of-use, reduced operator dependence, and automatic patient-specific motion detection. Free-running imaging increases the amount of information available to the clinician and is flexible enough to be translated to different applications within cardiac MRI. Moreover, the self-gating of the free-running framework decoupled the acquisition from the motion compensation and thereby opened up cardiac MRI to the wider class of steady-state-based techniques utilizing balanced steady-state free precession (bSSFP) sequences, which have the benefits of practical simplicity and high signal-to-noise ratio. The focus of this thesis was therefore on the application of steady-state techniques to cardiac MRI.

The first part addressed the long acquisition time of the current free-running framework and focused on anatomical coronary imaging. The published protocol of the free-running framework used an interrupted bSSFP acquisition where CHESS fat saturation modules were inserted to provide blood-fat contrast, as they suppress the signal of fat tissue surrounding the coronary arteries, and were followed by ramp-up pulses to

reduce artefacts arising from the return to steady-state. This interrupted acquisition, however, suffered from an interrupted steady-state, reduced time efficiency, and higher specific absorption rate (SAR). Using novel lipid-insensitive binomial off-resonant RF excitation (LIBRE) pulses developed in our lab, the first project showed that LIBRE pulses incorporated into an uninterrupted free-running bSSFP sequence could be successfully used for 5D cardiac MRI at 1.5T. The free-running LIBRE approach reduced the acquisition time and SAR relative to the previous interrupted approach while maintaining image quality and vessel conspicuity. Furthermore, this had been the first successful use of a fat-suppressing RF excitation pulse in an uninterrupted bSSFP sequence for cardiac imaging, demonstrating that uninterrupted bSSFP can be used for cardiac MRI and addressing the problem of clinical sequence availability.

Inspired by the feasibility of uninterrupted bSSFP for cardiac MRI, the second part investigated the potential of PLANET, a novel 3D multiparametric mapping technique, for free-running 5D myocardial mapping. PLANET utilizes a phase-cycled bSSFP acquisition and a direct ellipse-fitting algorithm to calculate T_1 and T_2 relaxation times, which suggested that it could be readily integrated into the free-running framework without interrupting the steady-state. After initially calibrating the acquisition, the possibility of accelerating the static PLANET acquisition was explored prior to applying it to the moving heart. It was shown that PLANET accuracy and precision could be maintained with two-fold acceleration with a 3D Cartesian spiral trajectory, suggesting that PLANET for myocardial mapping with the free-running 5D radial acquisition is feasible. Further work should investigate optimizing the reconstruction scheme, improving the coil sensitivity estimate, and examining the use of the radial trajectory with a view to implementing free-running 5D myocardial T_1 and T_2 mapping.

This thesis presents two approaches utilizing RF-frequency-modulated steady-state techniques for cardiac MRI. The first approach involved the novel application of an uninterrupted bSSFP acquisition with off-resonant RF excitation for anatomical coronary imaging. The second approach investigated the use of phase-cycled bSSFP for free-running 5D myocardial T_1 and T_2 mapping. Both methods addressed the challenge of clinical availability of sequences in cardiac MRI, by showing that a common and simple sequence like bSSFP can be used for acquisition while the steps of motion compensation and reconstruction can be handled offline, and thus have the potential to improve adoption of cardiac MRI.

RÉSUMÉ

Les maladies cardiovasculaires (MCV) représentent la principale cause de décès aux États-Unis et en Europe et génèrent des coûts de santé de plusieurs centaines de milliards de dollars par an. Les méthodes conventionnelles de diagnostic des MCV sont souvent invasives et comportent des risques pour le patient. Par exemple, la méthode de référence pour le diagnostic de la maladie coronarienne, une catégorie majeure de MCV, est la coronarographie par rayons X qui a comme inconvénients son caractère invasif, son coût, l'utilisation de rayonnements ionisants et le risque de complications. A l'inverse, l'angiographie coronarienne par résonance magnétique (ARM) n'utilise pas de rayonnements ionisants, permet de visualiser efficacement les tissus sans avoir recours à des agents de contraste exogènes et bénéficie d'une résolution temporelle ajustable. Cependant, le temps d'acquisition en IRM cardiaque est bien plus long que les échelles temporelles des mouvements cardiaques et respiratoires en jeu, ce qui rend la compensation de ces mouvements indispensable. Le cadre dit de « free-running » est un nouveau développement de notre laboratoire qui bénéficie des progrès réalisés au cours des trois dernières décennies et tente de remédier aux inconvénients des approches précédentes pour l'IRM cardiaque : il fournit une IRM cardiaque en cinq dimensions (5D) complètement « self-gated » , c'est-à-dire capable de détecter les mouvements cardiaques et respiratoires, forte d'une implémentation simplifiée, d'une plus grande facilité d'utilisation, d'une dépendance réduite vis-à-vis de l'opérateur et d'une détection automatique des mouvements spécifiques du patient. L'imagerie « free-running » augmente la quantité d'informations à disposition du clinicien et est suffisamment flexible pour être appliquée à différents domaines de l'IRM cardiaque. De plus, le « self-gating » du cadre « free-running » a découplé l'acquisition de la compensation de mouvement et a ainsi ouvert l'IRM cardiaque à la classe plus large des techniques basées sur l'état stationnaire utilisant des séquences de précession libre équilibrée en état stationnaire (bSSFP), qui se distinguent par leur simplicité d'utilisation et leur rapport signal sur bruit élevé. Le thème de cette thèse est donc l'application des techniques basées sur l'état stationnaire à l'IRM cardiaque.

La première partie porte sur le long temps d'acquisition de l'actuel cadre « free-running » et se concentre sur l'imagerie anatomique coronaire. Le protocole publié utilise une acquisition bSSFP interrompue où des modules de saturation de graisse (CHESS) sont insérés de façon à fournir un contraste sang-graisse puisqu'ils suppriment le signal du tissu graisseux entourant les artères coronaires, et sont suivis par des impulsions en rampe pour réduire les artefacts résultant du retour à l'état stable. Cette acquisition interrompue souffre cependant d'un état d'équilibre interrompu, d'une efficacité temporelle réduite et d'un débit d'absorption spécifique (DAS) plus élevé. En utilisant les nouvelles impulsions d'excitation radiofréquence (RF) binomiales hors-résonance insensibles aux lipides (LIBRE) développées dans notre laboratoire, ce premier projet montre que les impulsions LIBRE incorporées dans une séquence bSSFP ininterrompue et « free-running » peuvent être utilisées avec succès pour l'IRM cardiaque 5D à 1,5 T. L'approche « free-running LIBRE » permet de réduire le temps d'acquisition et le DAS par rapport à l'approche interrompue précédente, tout en maintenant la perceptibilité des artères coronariennes. En outre, il s'agit de la première utilisation réussie d'une impulsion d'excitation RF supprimant la graisse dans une séquence bSSFP ininterrompue pour l'imagerie cardiaque, ce qui démontre le potentiel d'utilisation de la séquence bSSFP ininterrompue pour l'IRM cardiaque et résout le problème de la disponibilité de la séquence en clinique.

Inspirée par la faisabilité d'utilisation de la séquence bSSFP ininterrompue pour l'IRM cardiaque, la deuxième partie étudie le potentiel de PLANET, une nouvelle technique de cartographie 3D multiparamétrique, pour la cartographie 5D du myocarde via l'imagerie « free-running ». PLANET utilise une acquisition bSSFP à cycle de phase et un algorithme d'ajustement d'ellipse direct pour calculer les temps de relaxation T1 et T2, ce qui suggère que cette méthode pourrait être facilement intégrée au cadre « free-running » sans interruption de l'état d'équilibre. Après calibration de l'acquisition, nous explorons la possibilité d'accélérer l'acquisition statique de PLANET pour l'appliquer au cœur. Nous démontrons que l'exactitude et la précision de PLANET peuvent être maintenues pour une accélération double avec une trajectoire 3D cartésienne en spirale, ce qui suggère que PLANET est réalisable pour la cartographie du myocarde avec une acquisition radiale 5D « free-running ». D'autres travaux devraient porter sur l'optimisation du schéma de reconstruction, l'amélioration de l'estimation de la sensibilité de l'antenne et l'examen de l'utilisation de la trajectoire radiale en vue de la mise en œuvre de la cartographie 5D « free-running » T1 et T2 du myocarde.

Cette thèse présente deux approches utilisant des techniques de modulation de fréquence radio en état stationnaire pour l'IRM cardiaque. La première approche implique l'application nouvelle d'une acquisition bSSFP ininterrompue avec une excitation RF hors résonance pour l'imagerie anatomique coronaire. La seconde approche porte sur l'utilisation d'une séquence bSSFP à cycle de phase pour la cartographie 5D T1 et T2 du myocarde. Ces deux méthodes permettent de répondre au défi posé par la disponibilité des séquences en IRM cardiaque en montrant qu'une séquence commune et simple comme la bSSFP peut être utilisée pour l'acquisition, tandis que les étapes de compensation du mouvement et de reconstruction peuvent être traitées hors ligne. Ainsi, ces méthodes ont le potentiel de favoriser l'adoption de l'IRM cardiaque.

LIST OF ABBREVIATIONS

3D-QALAS	3D-QuAntification using an interleaved Look-Locker Acquisition Sequence with T2 preparation pulse
ADMM	alternating direction method of multipliers
ATR	alternating TR
BORR	binomial off-resonant rectangular
bSSFP	balanced steady-state free precession
CABIRIA	cardiac balanced-SSFP inversion recovery with interleaved sampling acquisition
CAD	coronary artery disease
CHESS	chemical-shift-selective
CoV	coefficient of variation
CS	compressed sensing
CVD	cardiovascular disease
CRLB	Cramer-Rao lower bound
DESS	double-echo steady-state
Δf_0	off-resonant precession frequency in Hz
ECG	electrocardiogram
fNAV	focused navigation
FISS	fast interrupted steady-state
FOV	field-of-view
FS-TIDE	fat-saturated transition into driven equilibrium
FT-PC	Fourier transform regularization applied along the phase cycle dimension
GRE	gradient-recalled echo
GM	grey matter
IDEAL	iterative decomposition of water and fat with echo asymmetry and least-squares estimation
IFR	interrupted free-running
IR	inversion recovery

IR-SE	inversion recovery spin-echo
ISMRM	International Society for Magnetic Resonance in Medicine
LIBRE	lipid-insensitive binomial off-resonant RF excitation
ME-SE	multi-echo spin-echo
M_{eff}	effective magnitude (PLANET)
MIRACLE	motion-insensitive rapid configuration relaxometry
MOLLI	modified Look-Locker inversion recovery
MPME	multipathway multi-echo
MRA	magnetic resonance angiography
MRI	magnetic resonance imaging
PCA	principal component analysis
QuICS	quantitative imaging using configuration states
RF	radiofrequency
ROI	region of interest
S5FP	spectrally selective suppression with SSFP
SAR	specific absorption rate
SCMR	Society for Cardiovascular Magnetic Resonance
SENSE	sensitivity encoding
SI	superior-inferior
SNR	single-to-noise ratio
SPIR	spectral presaturation with inversion recovery
STEM	stimulated-echo-based mapping
STIR	short TI inversion recovery
T_1	longitudinal relaxation time
T_2	transverse relaxation time
TE	echo time
TESS	triple-echo steady-state
TI	inversion time
TR	repetition time
TVs	spatial total variation
WE	water excitation
WM	white matter
XD-GRASP	extra-dimensional golden-angle radial sparse parallel MRI

CONTENTS

LIST OF FIGURES

would correspond to the phase-cycled bSSFP signal of a single voxel in stationary tissue.

LIST OF TABLES

1   INTRODUCTION

1.1   Preamble

This thesis assumes knowledge of the basics of magnetic resonance (MR) physics, k-space, and magnetic resonance imaging (MRI) hardware. The reader should also be familiar with compressed sensing (CS), for which a good introduction in the context of MRI can be found in (1). This chapter will motivate cardiac MRI and provide a brief state-of-the-art description, including a development from our lab, free-running cardiac imaging, before culminating with the motivation and outline of the thesis.

1.2   Clinical relevance of coronary MRA and quantitative cardiac MRI

Cardiovascular disease (CVD) is the leading cause of death in the USA and Europe (2,3), with coronary artery disease (CAD), also known as ischaemic heart disease, accounting for almost half of CVD-related deaths among both regions. The total cost of CVD was approximately \$550 billion annually in the USA (2). In the European Union, CVD cost €210 billion in 2015 and ranged from 6% to 19% of national healthcare expenditure among member nations (3).

As will be shown in the rest of this section, cardiac MRI has the potential to provide multiple types of information for the diagnosis of CVD in a non-invasive manner. For the purposes of conciseness, this section will focus on two domains of cardiac MR relevant to this thesis: coronary MRA, and cardiac MR mapping of T_1 and T_2 relaxation times.

Selective x-ray coronary angiography is the gold standard for assessing CAD, although it is invasive and expensive, involves ionizing radiation, and has a small risk of complications (4). Coronary MRA is a promising alternative technique with several advantages (4–6) over x-ray angiography: it does not involve ionizing radiation; it

provides high soft-tissue contrast without the need for exogenous contrast agent; it enables diagnosis of even heavily calcified plaques; and its temporal resolution is adaptable and robust to differences in heartrate. However, coronary MRA suffers from longer acquisition times (approximately 10-15 minutes for 3D Cartesian free-breathing navigator-gated acquisitions versus seconds for coronary computed tomography angiography), operator-dependance, and lower study success rate (6). In addition, coronary MRA is technically challenging, requiring adequate spatial resolution and coverage, contrast between blood and surrounding tissues, and compensation of cardiac ("beating") and respiratory (breathing) motion (4). Since the initial study showing the clinical viability of coronary MRA (7), the specificity and sensitivity of coronary MRA have improved to the point that coronary MRA was recently recommended by the Society for Cardiovascular Magnetic Resonance (SCMR) as a "first line imaging technique" for three out of four classes of CAD (8). The SCMR's recommended MRA protocol is a 3D free-breathing navigator-gated ECG-triggered acquisition (9). Outstanding challenges with coronary MRA are operator-dependance, long acquisition times, pulse sequence availability across different MR scanner manufacturers, and automatic determination of patient-specific cardiac acquisition windows (6).

Cardiac T_1 and T_2 mapping has several potential diagnostic uses (10). Cardiac non-contrast T_1 mapping has potential for diagnosing acute myocardial infarction (11), myocardial edema (12), myocarditis (13,14), and amyloidosis (15). In the case of myocarditis and amyloidosis, for example, the gold standard for diagnosis is an endomyocardial biopsy (16), which has the disadvantages of invasiveness and sampling errors; T_1 mapping would eliminate the invasiveness and required preparation. Moreover, even though late gadolinium enhancement can serve as a non-invasive alternative for detecting amyloidosis, its diffusivity leads to errors in interpretation (16) and the administration of gadolinium has the potential for health complications (17), which are both avoided with non-contrast T_1 mapping (15). Cardiac T_2 mapping has potential for diagnosing myocarditis (13,14,18) and edema due to acute myocardial infarction (19,20). Although there exist guidelines for diagnosing myocarditis with cardiac MRI – the Lake Louise Criteria (21) – they involve T_1-weighted, T_2-weighted, and late gadolinium enhanced images that are subject to interpretation and suffer from poor accuracy (22). In contrast, T_1 and T_2 myocardial mapping provide quantitative results and were shown to improve diagnostic accuracy for acute myocarditis (23). In particular, the SCMR states that cardiac T_1 and/or T_2 mapping have "proven clinical utility" for detecting myocarditis and amyloidosis (10). However, current disadvantages of standard T_1 and T_2 cardiac mapping techniques (10,24,25) include the use of mono-

exponential models that do not account for complex tissue composition, confounders such as B_0 and B_1 inhomogeneities, the need for breath-holds, limited spatial coverage, partial volume effects, and limitations with both map generation and map analysis (refer to Section 3.2.1 for more details).

Cardiac multiparametric mapping, involving the determination of multiple parameters from the same acquisition, has both technical and clinical advantages over single-parameter techniques. Multiparametric mapping avoids the need for co-registration of maps from separate techniques, and thereby facilitates the combination of different maps, which may have complementary or synergistic value for diagnoses. In fact, T_1 and T_2 mapping were found to have complementary information in detection of acute myocarditis in adult (26) and pediatric (22) patients, and in detection of myocardial edema due to acute myocardial infarction in a canine model (27). The combination of T_1 and T_2 maps synergistically improved sensitivity and specificity in detection of cardiac allograft rejection (28). Section 3.2.3 will discuss current cardiac T_1 and T_2 multiparametric mapping techniques and their strengths and drawbacks from a technical perspective.

1.3 Don't plan it, just scan it! A brief history of free-running cardiac MRI

After the first report of an MR image in 1973 by Lauterbur (29), one of the earliest coronary MRA studies was performed in 1991 by Edelman et al. (30) using a 2D Cartesian breath-held electrocardiogram (ECG)-gated gradient-recalled echo (GRE) sequence. The k-space acquisition was divided into segments, with each segment acquired during the diastolic phase of the cardiac cycle. This technique had the disadvantages of requiring breath-holds, which can be difficult for some patients (31), ECG set-up, which takes time and is prone to failure (32), and limited spatial coverage of the coronary artery tree. By 1996, respiratory navigator-gating (33) had enabled free-breathing 3D coronary MRA (34,35), which became and remains the reference technique for coronary MRA (9,36). Navigator-gating tracked respiratory motion of the heart by using the vertical motion of the lung-liver interface, detected by additional navigator echoes, as a proxy, and imaging data was only acquired when the vertical position was within a predefined window. Although this technique removed the required breath-holding effort on the part of the patients, it suffered from an unpredictable acquisition time, due to a low respiratory gating acceptance rate (37), sensitivity to the navigator position (38) and respiratory (39) and cardiac (40) cycle variability, and limited spatial

coverage (41). Other technical factors, such as the need to position the ECG leads and navigator and perform preparatory scout scans to determine the quiescent cardiac phase, led to operator-dependance and a complicated workflow. The poor spatial coverage and long acquisition time led to the development of double-oblique imaging (42), where the left and right coronary artery trees were imaged with two targeted 3D volumes, which required dedicated scan planning and still did not cover the entire coronary tree (41). Another approach around this time provided fully cardiac- and respiratory-motion-corrected real-time 2D coronary MRA using an adaptive averaging technique that used cross-correlation to collect motion-consistent data and correct for respiratory-induced translation (43). This technique did not require ECG set-up or breath-holding, but still had limited spatial coverage due to the use of a 2D acquisition. The advent of balanced steady-state free precession (bSSFP) sequences improved SNR and blood-myocardium contrast (44), while the development of sensitivity encoding (SENSE) (45) allowed acceleration of MRI scans. These developments were critical in enabling whole-heart coverage in free-breathing 3D coronary MRA (41) in 2003. The whole-heart approach improved delineation of distal parts of the coronary arteries and reduced workflow complexity. Concurrently, Larson et al. derived cardiac motion signals directly from radial imaging data for self-gated breath-held 2D cine (32) in 2004, although Kim et al. had shown in 1990 that motion signals could be derived from radial projections (46) and were the first to use the term "free running." Cardiac self-gating removed the need for ECG set-up and potential difficulties of ECG use (32). 3D coronary MRA with respiratory self-navigation (47) followed soon after, which tracked vertical respiratory motion of the heart directly from imaging data using the superior-inferior (SI) readout of the 3D radial trajectory, and corrected the acquired k-space data using this signal. The 3D radial trajectory regularly sampled the SI readout, which had not been possible with conventional 3D Cartesian trajectories. The use of a spiral phyllotaxis pattern (48) reduced eddy current effects with 3D radial acquisitions, and was readily adapted for 3D whole-heart self-navigated coronary MRA (37), showing a two-fold reduction in scan time compared to navigator gating. Self-navigation obviated the need for separate navigator echoes and their associated drawbacks in terms of scan time variability. The first cardiac and respiratory self-gated (hereon in referred to as fully self-gated) 3D cardiac MRI study was performed in 2014 by Pang et al. (49). This study used a contrast-enhanced GRE acquisition at 3T with binomial water excitation and a 3D radial trajectory, where PCA was applied to the SI projections (Fourier-transformed SI readouts) to extract cardiac and respiratory motion, which were used to bin the data and subsequently reconstruct respiratory-motion-corrected 4D cardiac-resolved images. XD-GRASP was developed in 2016 (50), and enabled the acceleration

of dynamic MRI and improvement of apparent SNR by exploiting sparsity along the dynamic dimensions using a CS reconstruction (51), which had only been developed in 2006. XD-GRASP was successfully used for 4D respiratory-motion-resolved coronary MRA (52), which improved coronary artery delineation compared to self-navigated acquisitions. The addition of a cardiac dimension to XD-GRASP led to 5D motion-resolved cardiac MRI (53) using ECG-gating and a free-running 3D radial acquisition (40).

The free-running framework culminated in the combination of several of these developments (54) around the start of my PhD. It replaced the ECG-gating of the 5D technique (53) with automated cardiac and respiratory self-gating (54), combining it with the free-running 3D radial acquisition (40) and motion-resolved XD-GRASP reconstruction (50). The free-running framework enabled fully self-gated 5D cardiac MRI at high isotropic resolution with minimal set-up and scan planning. The acquisition consisted of a periodically-interrupted bSSFP acquisition, where chemical-shift-selective (CHESS) fat saturation modules (55) were inserted to provide blood-fat contrast followed by linearly-increasing ramp-up pulses to reduce artefacts in the return to steady-state, with the 3D radial spiral phyllotaxis trajectory (48). Physiological cardiac and respiratory motion signals were extracted by applying principal component analysis (PCA) to the SI projections (54) and were used to bin the acquired k-space data. In effect, this way of obtaining the motion signals decoupled the acquisition from the motion compensation, which had not been achievable with any other previous technique. Cardiac-and-respiratory-motion-resolved images were reconstructed using XD-GRASP.

Referring to the afore-mentioned outstanding challenges with cardiac MRI (6), the free-running framework reduced operator-dependance and automated subject-specific cardiac motion compensation through its data-driven cardiac self-gating. Furthermore, the reduction of preparation time and operator-dependance may help to improve the efficiency of the clinical routine by increasing the number of patients who can be examined and, thereby, reduce medical costs. Additionally, the free-running framework drastically improved the duty cycle – the amount of imaging data concerning the heart sampled per unit time – to about 30%, compared to a few percent with ECG-triggered self-navigated approaches.

Although it was developed for coronary MRA, the free-running framework has been adapted to multiple purposes in the lab over the course of my PhD. The interested reader

is referred to the thesis of Lorenzo Di Sopra (56) for a more comprehensive description of the developments leading up to the free-running framework and its initial applications.

1.4   Balanced steady-state free precession imaging

Given its importance in the development of the free-running framework, a brief technical overview of the balanced steady-state free precession (bSSFP) sequence is given below. Useful review articles that were consulted included Bieri et al. (57), Scheffler et al. (58), and Hargreaves et al. (59).

bSSFP is a gradient echo sequence with zero gradient moment across each TR – hence the descriptor "balanced" – that, under the condition TR << T_2 < T_1, generates high signal with T_2/T_1 contrast and a relative insensitivity to flow and motion (57). bSSFP sequences can be used with either non-selective or slice-selective excitation. The choice of TE is usually set to TR/2, at which time the transverse magnetization from all isochromats regardless of off-resonance is refocused and this accounts for the spin-echo-like behaviour of bSSFP (57).

bSSFP transverse magnetization, or signal, over time is characterized by an initial transient phase and a steady-state (Figure 1A). The transient phase consists of signal oscillations that are affected by, among other things, the off-resonance of the voxel, and that gradually settle around the equilibrium transverse magnetization, referred to as the steady-state signal. Various strategies exist to mitigate these signal oscillations, such as adding linearly-increasing (ramp-up) pulses (Figure 1B) (60), or using an α/2-TR/2 preparation scheme (61). Based on experience with numerical simulations, steady-state is reached after approximately 200 to 2000 excitations depending on the off-resonance.
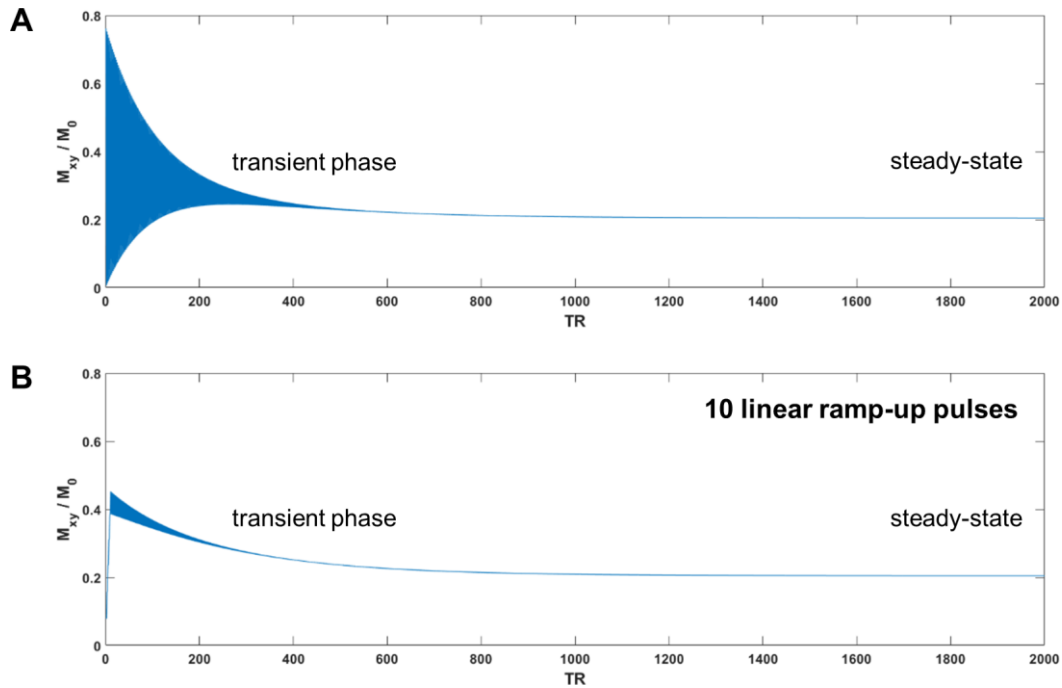
Figure 1. bSSFP relative signal magnitude, M_{xy}/M_0, (A) without and (B) with 10 linear ramp-up pulses. The signal initially oscillates during the transient phase before settling towards its steady-state value.

The steady-state signal shows a characteristic periodic variation with off-resonance (Figure 2A), with relatively broad regions of high signal magnitude punctuated by abrupt "stopbands," or losses of signal. This behaviour is independant of RF excitation angle, and is also characterized by constant signal phase in-between stopbands and jumps of $\pi/2$ rad at stopbands. Figure 2A and 2B display the off-resonance-related precession, $\theta_0 = 2\pi\Delta f_0 TR$, in radians, while off-resonance Δf_0 is in Hz. Isochromats that precess a multiple of 2π rad during a TR fall within this stopband, and therefore the distance between stopbands in Hz is 1/TR. These stopbands manifest as sharp banding artefacts in images (Figure 2C). Since the likelihood of bands occurring is proportional to TR, TR is recommended to be no more than 6 ms for conventional applications (57). As a matter of fact, bSSFP sequences gained popularity in the early 2000s after the development of gradient systems with higher slew rates that were able to keep TR within a range that minimized the risk of banding artefacts. In theory, the TR can be tuned so that the band falls on the off-resonance frequency of fat tissue. Furthermore, it can be seen that the on-resonant signal in Figure 2A, at 0 rad, is in a stopband, which serves to introduce another concept: phase cycling. Phase cycling refers to incrementing the radiofrequency (RF) excitation (B_1) phase from excitation to excitation by $\Delta\theta_{RF}$ during a bSSFP acquisition. Phase cycling shifts the frequency response profile of bSSFP by $\Delta\theta_{RF}$, and RF phase alternation with $\Delta\theta_{RF}$ = 180° (or -180°

to be consistent with Chapter 3) is typically used for scans to maximize on-resonance signal (Figure 2B) (57). The concepts discussed in this paragraph form the basis of the work in Chapter 2, where the tissue frequency response of a specific RF pulse is manipulated in order to suppress the signal of isochromats with specific tissue frequencies.
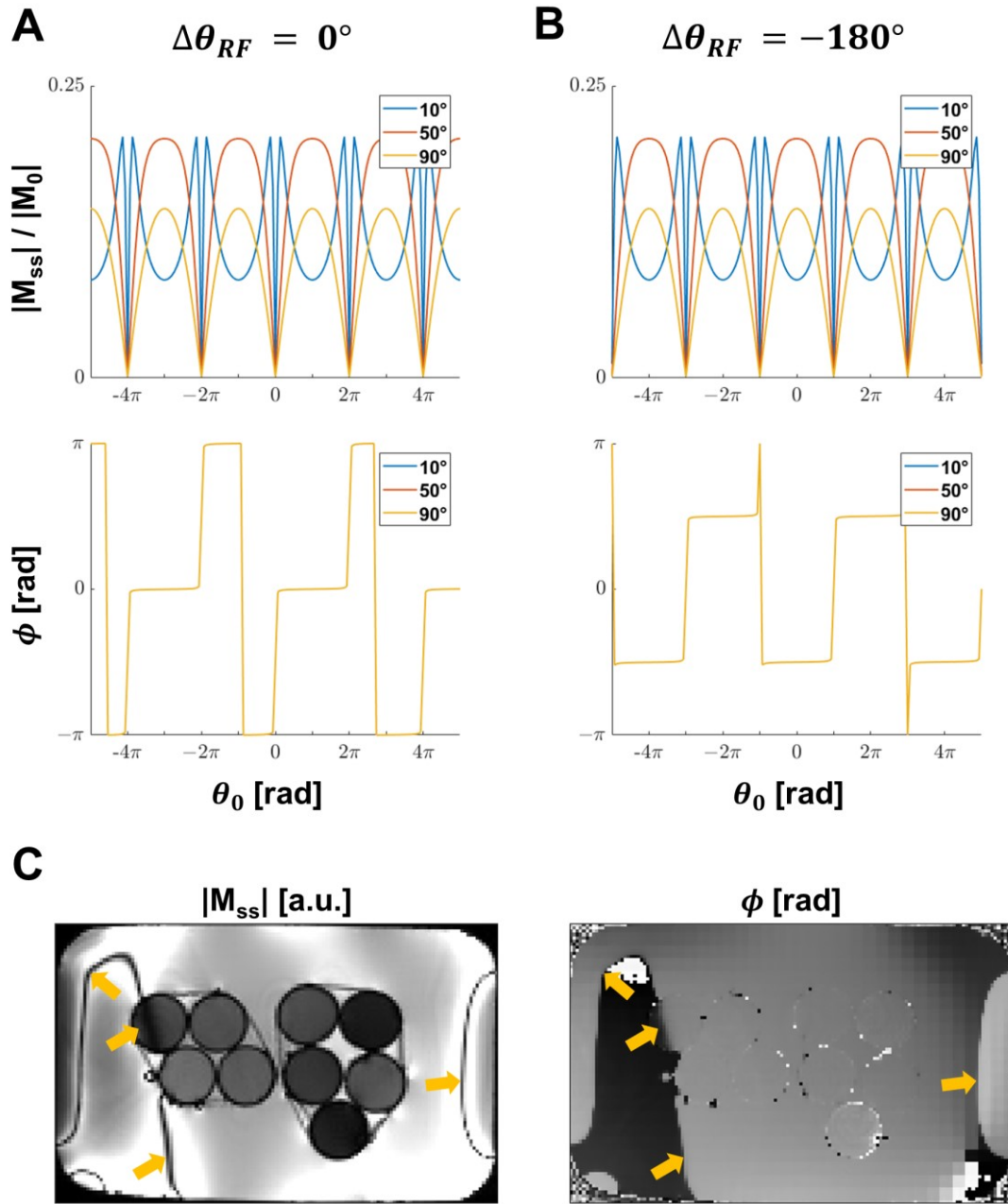
Figure 2. Steady-state magnetization as a function of off-resonance precession, θ_0 [rad], (A) without and (B) with RF phase alternation for different RF excitation angles (see legend). Shown are the relative magnitude, $|M_{ss}|/|M_0|$, and the phase, ϕ. (C) Magnitude and phase images of a phantom acquired with bSSFP at 3T with TR = 10 ms (with RF phase alternation). Orange arrows indicate banding artefacts; the lack of discontinuities in the bands is due to the general smoothly-varying nature of B_0 inhomogeneities.

As can be seen in Figure 2, phase cycling affects both the magnitude and phase of the bSSFP signal. In the complex plane, the trajectory of the steady-state signal follows an ellipse as $\Delta\theta_{RF}$ is varied (Figure 3). This property forms the basis of the work in Chapter

3, which provides a published theoretical model for the steady-state signal that takes into account all the variables discussed so far.
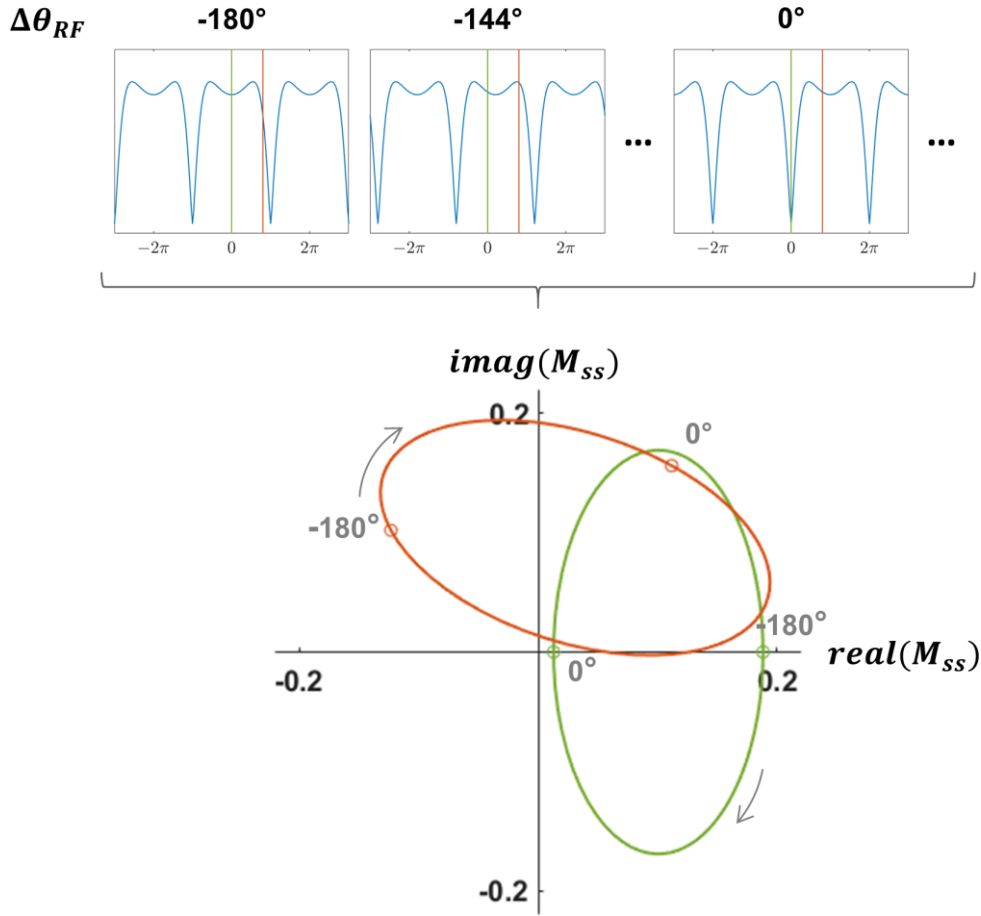
Figure 3. Steady-state signal, M_{ss}, as a function of RF phase increment, $\Delta\theta_{RF}$. The signal magnitude is shown at the top as a function of off-resonance for a few different $\Delta\theta_{RF}$: phase cycling with $\Delta\theta_{RF}$ induces a shift of the off-resonance profile by $\Delta\theta_{RF}$ rad. In the complex plane, the trajectory of M_{ss} traces an ellipse as $\Delta\theta_{RF}$ is varied, and the effect of off-resonance is to rotate this ellipse. The green and red lines and ellipses correspond to the signal for 0 and 40 Hz, respectively. The grey arrows indicate the direction the signal vector moves along the ellipse as $\Delta\theta_{RF}$ is increased.

It should be noted that the figures assume idealized instantaneous pulses, which in reality would have a finite duration. A detailed discussion can be found in (62).

1.5   Thesis motivation and outline

The free-running framework incorporating a 3D radial trajectory, motion extraction, and compressed sensing reconstruction represented a significant advancement in ease-

of-use of cardiac MRI. As will be motivated by this thesis, it enabled using uninterrupted bSSFP sequences for cardiac MRI and opened up the possibility of bSSFP-based techniques. Therefore, the focus of this thesis was applying steady-state imaging techniques to the free-running framework to enable anatomical coronary and quantitative myocardial imaging without interrupting the steady-state, in order to improve ease-of-use and sequence availability compared to current techniques. Specifically, the techniques investigated here modulated the RF excitation frequency and, moreover, constituted a rarely-investigated class of techniques within MRI.

The free-running framework provided fully self-gated cardiac MRI without the need for ECG set-up and with minimal scan planning. While the insertion of CHESS fat saturation pulses between bSSFP readouts enabled effective coronary artery visualization, the periodically-interrupted acquisition had the disadvantages of a reduced duty cycle, time inefficiency, and increased SAR (53). Recent work in our lab at the time had led to the development of lipid-insensitive binomial off-resonant RF excitation (LIBRE) pulses (63), and suggested that LIBRE had potential for integration in the free-running framework. My first project was, therefore, to investigate whether LIBRE integrated into an uninterrupted bSSFP sequence would remove the need for the CHESS modules and ramp-up pulses, improving time efficiency and reducing SAR. I did so using numerical simulations, in vitro phantom acquisitions, and in vivo volunteer acquisitions. This project and a relevant background are described in Chapter 2.

It was also during this first project that I was exposed to the theory and benefits of bSSFP sequences and current work in cardiac MRI. When I happened to read the PLANET paper (64), it appeared that the technique could be readily translated to the free-running framework for myocardial T_1 and T_2 mapping, as PLANET required an uninterrupted bSSFP acquisitions and my work had shown that such steady-state acquisitions were feasible for free-running imaging. The goal was free-running 5D motion-resolved mapping of myocardial tissue of the heart, which had never been accomplished before. While the LIBRE technique manipulated the RF frequency during excitation to obtain a specific tissue frequency response profile, this technique maintained a constant frequency during excitation but manipulated it across acquisitions by manipulating the RF phase increment, and exploited the elliptical signal model of phase-cycled bSSFP to recover tissue relaxation times. My efforts to achieve free-running 5D PLANET mapping are documented in Chapter 3.

2 FREE-RUNNING bSSFP CORONARY MRA WITH LIBRE PULSES

2.1 Outline

This chapter will present work on optimizing lipid-insensitive binomial off-resonant RF excitation (LIBRE) pulses in bSSFP for free-running 5D coronary angiography. A literature overview of previous techniques for obtaining fat-free MR images will be briefly discussed, followed by the context and purpose of the project. A copy of the published article resulting from this work is given, followed by a conference abstract submitted by a colleague that addresses one of the limitations – namely, image reconstruction time – of the free-running LIBRE technique. The chapter concludes with a discussion and outlook.

2.2 Fat suppression techniques

This section will present an abbreviated overview of the general classes of fat suppression techniques, as well as their previous applications to coronary MRA of the heart. A very informative review article was that by Bley et al. (65).

Since the coronary arteries are embedded in epicardial fat (Figure 4), some way of generating blood-fat contrast is necessary to visualize them with MRI. This contrast can be either extrinsic, such as the use of contrast agents that increase blood signal, or intrinsic, where the sequence itself reduces fat signal and hence reduces the invasiveness of the technique.
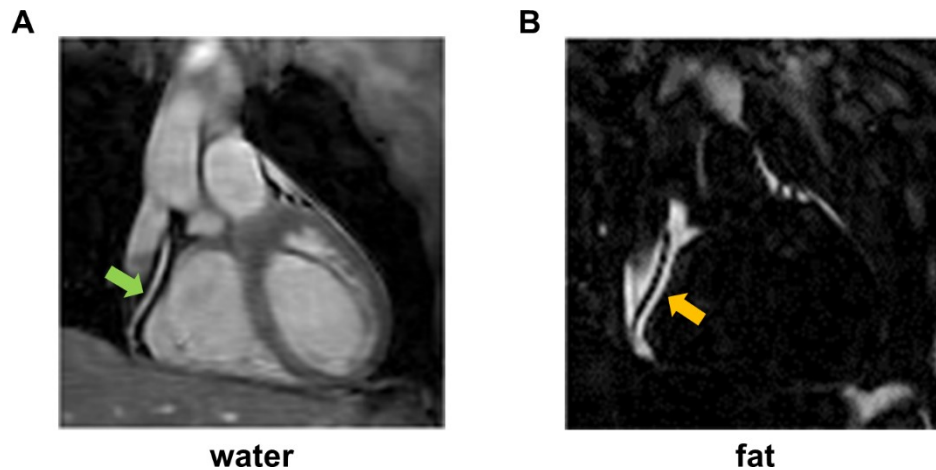
Figure 4. Corresponding A) water-only and B) fat-only images of the heart of a healthy volunteer. The right coronary artery (green arrow, A) is surrounded by fat (yellow arrow, B). Figure adapted from (66), which was published under a Creative Commons CC BY license.

Fat suppression techniques can be classified into a) those that separate fat from water based on its different T_1 relaxation time (Section 2.2.1), and b) those that separate fat based on its chemical shift or resonant frequency offset relative to that of water (Section 2.2.2).

2.2.1 T_1-based approaches

The original technique in this category is called short TI inversion recovery (STIR) (65,67). An inversion RF pulse is applied and the tissue signals evolve based on their T_1 relaxation time. At one point, at an inversion time (TI) after the pulse of approximately 200 ms at 1.5T (65), the longitudinal magnetization of fat will be zero, and an image acquired at this point will have no contribution from fat signal. The main advantage of STIR is uniform fat suppression that is robust to even high B_0 inhomogeneities (65). However, STIR nulls the signal of any short T_1 tissue, such as those that take up contrast agents, meaning it is clinically used for T_2-weighted or proton-density-weighted imaging, and SNR is generally reduced as the water longitudinal magnetization is reduced by the inversion pulse (65). Due to the long TI, it is also time-inefficient (65). The B_1 sensitivity of the technique depends on the type of inversion pulse used (65).

A further development combines STIR with elements of the CHESS technique below: spectral presaturation with inversion recovery (SPIR) (68). SPIR uses a frequency-selective inversion pulse to selectively saturate the fat longitudinal magnetization not only based on T_1 but also chemical shift, such that other short-T_1 contrast-enhanced tissues are not saturated (68) and the SNR reduction present with STIR is avoided.

STIR has not been widely used for fat suppression in coronary MRA applications. Ginami et al. used it for fat suppression, with TI = 110 ms, prior to Cartesian bSSFP readouts in odd heartbeats as part of a combined bright-blood and black-blood technique (69). This study also used image-based navigators (70) that included linear ramp-up pulses, indicating that the ramp-up pulses do not disturb the required T_1-weighted fat suppression of STIR. It may be that the prescribed TI reduces the amount of k-space data that can be acquired per heartbeat in segmented cardiac acquisitions, which renders STIR techniques time-inefficient for cardiac imaging in general. It may also be that the prescribed TI makes it more difficult to do systolic imaging, as would be needed for patients with heartbeats over 70 beats per minute (36,49). With regards to radial imaging, every readout samples the centre of k-space, meaning that fat would need to be suppressed for every excitation by applying STIR prior to every radial readout, which would have the disadvantage of being time-inefficient and perhaps SAR-intensive. As an aside, a similar concept as STIR has been used for detection of myocardial infarction in gadolinium-enhanced MRI (71,72), where the TI is set to null normal myocardium and thereby enhance contrast with infarcted myocardium (73).

2.2.2 Chemical-shift-based approaches

This class of techniques relies on the different positions of fat and water in the tissue frequency domain.

2.2.2.1 Chemical shift selective (CHESS) imaging

The chemical shift selective (CHESS) (55,65) technique involves using an RF excitation pulse that selectively excites fat followed by a dephasing gradient. The RF carrier frequency is centred on the resonance frequency of fat, and the pulse shape is such that its spectral excitation profile (of resonance frequencies) encompasses the fat frequencies but not the on-resonant water frequencies, as the Fourier transform of the RF pulse envelope is approximately equal to its excitation profile in the spectral domain (74). An RF excitation angle of 90° will tip all fat spins into the transverse plane, and the dephasing gradient will spoil it, leaving no longitudinal fat magnetization for subsequent RF pulses to excite for imaging (65). This reliance on the properties of the RF excitation leaves the method sensitive to B_1 inhomogeneities (65). Moreover, it is also sensitive to B_0 inhomogeneities, since they can shift the positions of the fat and water peaks (65).

With regards to their use in bSSFP sequences, inserting CHESS pulses into every TR would be time-inefficient, and would disturb or potentially destroy the steady-state behaviour. Alternatively, they could be inserted periodically, which would require a method for maintaining the steady state. One such approach, referred to as the magnetization-prepared approach, was to apply an $\alpha/2$ pulse after TR/2 to store the steady-state transverse magnetization as longitudinal magnetization, then apply a CHESS pulse to saturate fat transverse magnetization, and then apply a "flipback" $\alpha/2$ pulse applied after TR/2 to restore the transverse steady-state magnetization (75). This approach had only a 5% to 15% percent acquisition time penalty compared to a normal bSSFP sequence (75), but was susceptible to off-resonant transient-phase artefacts in the return to steady-state (76).

CHESS has been commonly used for ECG-triggered coronary MRA, such as in one of the earliest clinical studies to show the feasibility of cardiac MRI for detecting coronary stenosis (7), as well as in 3D radial self-navigated acquisitions (37) and the original free-running study (53). As well, Deshpande et al. adapted the magnetization-prepared approach (75) et al. to 3D Cartesian ECG-triggered breath-held coronary MRA (44).

2.2.2.2 Water excitation

Water excitation techniques incorporate RF excitation pulses that directly excite only water isochromats (65,77).

A common example of this class are binomial water excitation (WE) pulses. Although not the earliest reporting of this technique, Hore (78) mathematically explained why a binomial pattern of the RF amplitude could generate the desired spectral selectivity. Briefly, the simplest case is a 1-180°-1 water excitation pulse. It consists of two identical RF excitation pulses separated in time by a duration τ that would result in a 180° phase difference between water and fat isochromats. For the case of a 90° excitation angle and infinitesimal-duration pulses, the first pulse will tip both water and fat magnetization by 45°, and, after a time τ, fat will have precessed by 180° relative to water. At this point, the second pulse will have the effect of tipping water by another 45° into the transverse plane, whereas the fat magnetization will be tipped back to the z-axis. Water will then have a net RF excitation angle of 90°, whereas the fat signal will be unaffected. This example illustrates that the total duration of these pulses decreases with field strength, as fat will achieve the required precession faster at higher field strengths, yet it also show one of the disadvantages of these pulses, namely their sensitivity to B_0

inhomogeneities, as fat isochromats with slightly different tissue frequencies from the expected one will have non-zero transverse magnetization. The B_0-sensitivity can be reduced, and the fat suppression band width increased, by using more binomial pulses (78) at the expense of total pulse duration. These pulses can be spatially-selective (79) or non-spatially-selective.

Recent developments have retained the binomial nature but used off-resonant pulses, which have a centre frequency different from the Larmor frequency. Ye et al. described a water excitation technique consisting of two consecutive off-resonant pulses with opposed phase, termed the binomial off-resonant rectangular (BORR) pulse (80). Spins to be suppressed precess for one or more complete cycles and return to the z-axis. BORR pulses are relatively B_0- and B_1-insensitive (80). Jessica Bastiaansen from our lab developed the lipid-insensitive binomial off-resonant RF excitation (LIBRE) technique (63), which functions on a similar principle but with no difference in phase between the two pulses. LIBRE is relatively insensitive to B_0 and B_1 inhomogeneities, and has reduced SAR compared to conventional 1-180°-1 pulses (63). The use of off-resonant pulses limits these methods to 3D applications, as the RF frequency of the pulse is exploited for spectral rather than spatial selectivity. Both methods also required numerical simulations to tune their parameters, suggesting that re-tuning for a different application might require such preparation.

A specific case of water excitation are spatial-spectral pulses that are simultaneously spatially- and spectrally-selective. Meyer et al. invented the method and initially derived the required RF and gradient waveforms (77). The original method used a train of varying-amplitude RF pulses in tandem with an oscillating z-gradient (77). Unlike the BORR and LIBRE techniques, they can be used for slice-selective or multi-slice acquisitions. Spatial-spectral pulses are insensitive to B_1 inhomogeneities (81) but are sensitive to B_0 imhomogeneities like the conventional binomial pulses (65), and off-centre slice positions require complicated RF waveform calculations (79). Furthermore, the pulse train increases acquisition time. Spatial-spectral pulses are both shorter and more B_0-insensitive at higher field strengths (65), as water and fat are separated more in the spectral domain.

Binomial pulses or pulse trains are not required. Long rectangular RF pulses have been used for 3D echo planar imaging of the brain (82), providing lower SAR and less B_0-sensitivity compared to conventional 1-180°-1 binomial pulses.

Of these pulses, the basic binomial pulses and LIBRE have been used in coronary MRA applications. LIBRE was used in an ECG-triggered self-navigated T_2-prepared acquisition in a GRE sequence at 3T, where it was compared to CHESS and 1-180°-1 WE (83). LIBRE reduced fat signal significantly compared to CHESS, and improved vessel sharpness and length compared to both pulses. In a GRE acquisition at 3T, a spatial-spectral pulse with a 1-2-1 pattern with optimized RF waveform and spiral readouts was used to demonstrate improved image quality and blood SNR compared to 1.5T (84). In an ECG-triggered navigator-gated 3D spiral study at 1.5T, SPIR and 1-1 spatial-spectral pulses were shown to generate similar image quality for coronary MRA, although the SPIR acquisition had a shorter scan time (85). 1-2-1 WE pulses were used in a contrast-enhanced self-gated 4D cardiac-resolved GRE acquisition at 3T to show that both coronary anatomy and cardiac function information could be obtained from the same scan (49).

2.2.2.3 Sequence-based fat suppression

This class of techniques suppresses fat by manipulating the properties of the sequence in order to manipulate the tissue frequency profile.

Certain techniques exploit the bSSFP sequence. Quist et al. used two phase-cycled bSSFP acquisitions, with large RF excitation angles above 50° and two acquisitions with $\theta_{RF} = 0°$ and $\theta_{RF} = 180°$, for simultaneous banding artefact reduction and fat suppression in peripheral angiography (86). The bSSFP spectral response is sinusoidal at such large angles, and was used to synthesize and shift a spectral profile for each voxel such that water signal was maximized (86). A region-growing algorithm was used to synthesize an off-resonance map from those two acquisitions, which avoided the extra time needed to acquire such a map separately. However, partial volume effects could cause this algorithm to fail, in which case the separate map would be required, yet the method was not otherwise sensitive to partial volume effects (86). It was also unclear how the method would perform in the presence of other fat peaks (86), making it potentially sensitive to B_0 inhomogeneities. Alternating TR bSSFP (ATR) used a sequence consisting of a constant phase cycling scheme but two different alternating TRs, where imaging readouts were only run during the first TR, to modify the frequency response of bSSFP (87). The resulting frequency response of ATR had similar on-resonant magnetization as bSSFP but a broader stopband around fat, at a cost of a 33% increase in acquisition time over bSSFP (87). The ATR technique had a relatively narrow fat suppression band, making it susceptible to B_0 inhomogeneities, although a robustness

to the value of the first TR provided flexibility for applications requiring different scan times (87). A further development reduced the B_0 sensitivity by adding a second ATR acquisition with a different RF phase cycle (88). Some other techniques will be briefly summarized. Using periodically variable RF angles (89) provided effective B_0-robust fat suppression, but was limited to a TR of 2.2 ms and suffered from reduced SNR. Using a specific sequence of RF angles (FS-TIDE) enabled fat suppression with transient-state artefact reduction (90,91), but required a calibration step and a specific trajectory, and may not be easily adaptable to 3D trajectories. The spectrally-selective wideband bSSFP approach (92) used 1-2-1 excitation pulses with no phase cycling and an appropriately modified system Larmor frequency, providing effective B_0- and B_1-insensitive fat suppression, at the cost of an increased TR. Spectrally selective suppression with SSFP (S5FP) replaced the $\alpha/2$ pulses of the magnetization-prepared approach above with opening and closing trains of pulses, and incorporated RF spoiling, for efficient fat-suppressed imaging; correction factors allowed data collected during the opening and closing trains to be used for imaging (76). Its B_0-sensitivity depended on TR (76).

Another sequence whose properties can be tuned to suppress fat is the fast interrupted steady-state (FISS) sequence (93). This sequence is composed of repeated FISS modules, which each consist of a bSSFP readout train, with balanced gradients and 180° RF phase cycling, preceded and followed by $\alpha/2$ pulses, and have a non-zero zeroth gradient moment in the slice direction (93). Thus, FISS combines the high on-resonant signal of bSSFP and the B_0-insensitvity of GRE. The fat suppression "valleys" of the FISS sequence are wider than the bands of the bSSFP sequence in the frequency response profile (93), but such fat suppression requires a narrow range of TRs of the bSSFP readout train, which puts constraints on spatial resolution and gradient hardware. Furthermore, the Cartesian version of FISS with more than one bSSFP readout per module had ghost artefacts in the phase-encoding direction caused by signal fluctuations due to the interruption of the steady state, which limited its initial use to radial trajectories (93).

FISS has been used in both radial and cardiac free-running 5D motion-resolved acquisitions. Bastiaansen et al. (94) applied FISS at 1.5T and 3T with a radial phyllotaxis trajectory (48), and reported significantly decreased fat SNR relative to a bSSFP sequence with a time penalty of 25%. However, they also reported that effective fat suppression required a specific range of TRs. Kuestner et al. (95) reported the use of FISS in a spiral-like Cartesian trajectory, using dummy RF pulses to mitigate the ghosting artefacts in the phase-encoding direction. They reported reduced motion aliasing artefacts from fat and improved image quality.

2.2.2.4 Fat-water separation

Fat-water separation techniques produce both water-only and fat-only images (65), as opposed to the previously-discussed techniques that produce water-only images.

The main class of techniques within this category are Dixon techniques (65), which acquire images at different echo times (TE) to extract phase information related to the different resonant frequencies of water and fat. The original two-point Dixon method (96) acquired two images, one of which had water and fat in-phase (W+F) and the other out-of-phase (W-F), from which water-only and fat-only images could be generated. However, it had the disadvantage that B_0 inhomogeneities could lead to fat-water swapping (65) in cases when, for example, a predominantly-water voxel had an off-resonant frequency close to that of fat. The three-point Dixon method (97) was able to additionally generate a B_0 map that, combined with phase unwrapping, could be used to avoid fat-water swapping. Dixon techniques are B_1-insensitive but have an increased scan time (65), which can however be accelerated. Moreover, the key factor affecting the success of water-fat separation is the avoidance of fat-water swaps (65,98). A further improvement was iterative decomposition of water and fat with echo asymmetry and least-squares estimation (IDEAL) (99), which allows the TEs to be optimized to maximize SNR and which can also be modified to account for different fat models (100). Dixon techniques have been used with bSSFP sequences (99,101–103). A more detailed overview of Dixon techniques can be found in Ma (98).

A subclass in this category involves fat-water separation using the properties of bSSFP techniques. Phase-sensitive bSSFP (104) exploited the fact that the phase of the signal undergoes a jump of π every TR^{-1} Hz in the spectral domain, coinciding with the location of the banding artefacts, and therefore used a TR that achieved a 180° phase difference between water and fat. Fat-water separation was achieved with an identical scan time as normal bSSFP with an insensitivity to B_1 inhomogeneities (105). The B_0 sensitivity of the technique depended on the chosen TR; for example, the original study used a TR of 4.6 ms, meaning that all voxels with an off-resonance of 110 Hz on either side of the the Larmor frequency would be detected as water. However, phase-sensitive bSSFP was sensitive to partial-volume effects (104), since voxels were assumed to be either water or fat. A further development involved the use of two acquisitions with RF phase cycling of 0 and π (105), which improved the B_0-insensitivity at the cost of a doubled acquisition time and a sensitivity to B_1 inhomogeneities. Fluctuating equilibrium MRI (106) used a 0°-90° RF phase alternation to generate a double steady state, where the images from

odd and even excitations had orthogonal spectral profiles, and an appropriate TR could lead to separate water and fat images. This method was sensitive to B_0 inhomogeneities, and required an ideal TR of 2.2 ms at 1.5T (106). Two-phase linear combination SSFP (107) generated fat and water images by adding and subtracting, respectively, images from bSSFP sequences with 0° and 180° RF phase cycling. This method doubled the scan time of normal bSSFP, was B_1-sensitive, and required an ideal TR of 2.2 ms (107).

Fat-water separation techniques have often been applied to coronary imaging (108–113). Börnert et al. showed that an ECG-triggered navigator-gated 3D anisotropic Cartesian 2-point Dixon technique improved image quality for coronary MRA in 30 patients compared to a similar bSSFP acquisition with CHESS for fat saturation (108); specifically, the Dixon method had more consistent fat suppression in both static and moving tissue. The single-acquisition phase-sensitive bSSFP technique was applied to a 3D stack-of-stars breath-held acquisition for 4D cardiac-resolved coronary MRA (113).

2.2.2.5 Trajectory-based techniques

This technique uses the tissue frequency response of the trajectory to generate water and fat images. Aside from a use of stochastic trajectories that was impractical due to eddy currents (114), the only other example was the use of multishot rosette trajectories for both 2D (115) and 3D (116) GRE acquisitions. Fat suppression with rosette trajectories relied on the fact that the k-space centre and other points were repeatedly sampled during one excitation, leading to destructive interference among phases of certain off-resonance isochromats. Rosette trajectories provided for rapid imaging and could be customized according to the gradient hardware limitations of the scanner (116). The repeated sampling of the k-space centre permitted the determination of B_0 maps directly from the imaging data (115). However, SNR was inherently decreased because off-resonant energy was dispersed throughout the image (115), making them most suitable for low-SNR applications such as metabolite imaging, where other noise sources would dominate the off-resonant-induced noise. Moreover, irregular TEs were necessary to remove periodic off-resonant signal increases (115).

Rosette trajectories have in fact been used in 2D ECG-triggered breath-held magnetic resonance fingerprinting acquisitions at 1.5T and 3T for simultaneous T_1 and T_2 maps and water-fat separation (117), although this technique was sensitive to B_0 inhomogeneities and partial volume effects.

2.3   Free-running 5D bSSFP coronary MRA with LIBRE pulses

The original 5D study (53) achieved fully motion-resolved coronary MRA at 1.5T using a periodically-interrupted free-running bSSFP sequence (40) with a 3D radial phyllotaxis trajectory (48) in combination with a compressed sensing technique (50,51) called XD-GRASP that used total variation regularization along the cardiac and respiratory dimensions. Cardiac motion detection was done using the ECG signal, and respiratory motion was detected by applying principal component analysis (PCA) to the SI projections (37) and picking the component with the highest spectral information in the respiratory frequency range. The use of the ECG still necessitated a certain initial set-up time to position the ECG, and occasionally did not work properly, leading to a "missed" trigger. A further development led to a fully self-gated free-running framework (termed IFR to be consistent with the manuscript) (54). A temporal spectral analysis of the principal components of the SI projections showed which components had the greatest power in the respiratory and cardiac frequency ranges, which were used as the respective motion signals. However, the fully self-gated free-running framework still used the periodically-interrupted bSSFP acquisition, where the steady state was periodically interrupted to insert CHESS modules for fat suppression and subsequent linear ramp-up pulses to reduce artefacts in the return to the steady-state. A steady-state signal behaviour was also necessary to provide blood-myocardium contrast. This interruption reduced the duty cycle and, hence, time efficiency of the acquisition, and the inserted CHESS modules increased SAR (53). In our lab, we had shown that LIBRE could be successfully used for coronary MRA in an ECG-triggered self-navigated T_2-prepared bSSFP acquisition at both 1.5T (118) and 3T (83). Based on these findings, it was hypothesized that LIBRE could be integrated into an uninterrupted bSSFP sequence for 5D coronary MRA as part of the free-running framework, without the need for the CHESS modules and ramp-up pulses. The first project was, therefore, to mechanistically study and optimize LIBRE as part of an uninterrupted free-running bSSFP sequence for fat-suppressed coronary MRA at 1.5T.

The LIBRE pulse was numerically optimized for blood-fat contrast in a bSSFP sequence, and these parameters were then validated in vitro in a phantom with compartments whose relaxation times resembled those of heart tissues. After a quick optimization of the LIBRE RF frequency in vivo, LIBRE pulses in an uninterrupted bSSFP sequence were compared in vivo to non-fat-suppressing rectangular pulses (SP) and 1-2-1 water excitation pulses (WE) in uninterrupted bSSFP sequences and to the previously-published IFR sequence.

2.3.1 Personal contribution

I coded the bSSFP numerical simulations in MATLAB based upon initial non-bSSFP code provided by Jessica Bastiaansen and based upon (119), and performed the simulations. I had the insight to optimize the LIBRE pulse numerically, as I realized that its three parameters did not independently modify the MR signal, which necessitated a simultaneous numerical optimization that would have been too lengthy to perform in vitro. I performed the phantom and volunteer scans using LIBRE sequence code from Jessica Bastiaansen. I obtained and ran the motion signal extraction pipeline from Lorenzo di Sopra and the CS reconstruction pipeline from Jérôme Yerly, and performed the full analysis for the in vitro and in vivo data. I wrote the initial submitted draft of the manuscript, and implemented expansive modifications during the peer-review process. The manuscript was published in *Magnetic Resonance in Medicine*, one of the leading journals in our field. I had previously presented it in an oral Power Pitch presentation at the 27th Annual Meeting of the International Society for Magnetic Resonance in Medicine (ISMRM) in 2019 in Montréal, Canada, and received a *Magna Cum Laude* award.

2.3.2 Peer-reviewed journal publication

The article published in *Magnetic Resonance in Medicine* (120) is reproduced here with permission under a personal license from John Wiley & Sons, Inc.

FULL PAPER

Magnetic Resonance in Medicine

Free-running 5D coronary MR angiography at 1.5T using LIBRE water excitation pulses

Nemanja Masala[1] [iD] | Jessica A. M. Bastiaansen[1] [iD] | Lorenzo Di Sopra[1] [iD] | Christopher W. Roy[1] [iD] | Davide Piccini[1,2] [iD] | Jérôme Yerly[1,3] [iD] | Roberto Colotti[1] | Matthias Stuber[1,3] [iD] [twitter]

[1]Department of Diagnostic and Interventional Radiology, Lausanne University Hospital (CHUV) and University of Lausanne (UNIL), Lausanne, Switzerland

[2]Advanced Clinical Imaging Technology, Siemens Healthcare AG, Lausanne, Switzerland

[3]Center for Biomedical Imaging (CIBM), Lausanne, Switzerland

Correspondence
Matthias Stuber, Department of Diagnostic and Interventional Radiology, Lausanne University Hospital (CHUV) and University of Lausanne (UNIL), Lausanne, Switzerland.
Email: Matthias.Stuber@chuv.ch

Funding information
Schweizerischer Nationalfonds zur Förderung der Wissenschaftlichen Forschung, Grant/Award Number: 143923, 173129 and PZ00P3_167871; Fondation Emma Muschamp; Schweizerische Herzstiftung

Purpose: To implement, optimize, and characterize lipid-insensitive binomial off-resonant RF excitation (LIBRE) pulses for fat-suppressed fully self-gated free-running 5D cardiac MRI.

Methods: Bloch equation simulations were used to optimize LIBRE parameter settings in non-interrupted bSSFP prior to in vitro validation. Thus, optimized LIBRE pulses were subsequently applied to free-running coronary MRA in 20 human adult subjects, where resulting images were quantitatively compared to those obtained with non-fat-suppressing excitation (SP), conventional 1-2-1 water excitation (WE), and a previously published interrupted free-running (IFR) sequence. SAR and scan times were recorded. Respiratory-and-cardiac-motion-resolved images were reconstructed with XD-GRASP, and contrast ratios, coronary artery detection rate, vessel length, and vessel sharpness were computed.

Results: The numerically optimized LIBRE parameters were successfully validated in vitro. In vivo, LIBRE had the lowest SAR and a scan time that was similar to that of WE yet 18% shorter than that of IFR. LIBRE improved blood–fat contrast when compared to SP, WE, and IFR, vessel detection relative to SP and IFR, and vessel sharpness when compared to WE and IFR (for example, for the left main and anterior descending coronary artery, 51.5% ± 10.2% [LIBRE] versus 42.1% ± 6.8% [IFR]). Vessel length measurements remained unchanged for all investigated methods.

Conclusion: LIBRE enabled fully self-gated non-interrupted free-running 5D bSSFP imaging of the heart at 1.5T with suppressed fat signal. Measures of image quality, vessel conspicuity, and scan time compared favorably to those obtained with the more conventional non-interrupted WE and the previously published IFR, while SAR reduction offers added flexibility.

KEYWORDS
5D whole-heart imaging, bSSFP, coronary MRA, fat suppression, free-running framework, water excitation

1 | INTRODUCTION

Cardiovascular disease accounts for $350 billion in direct and indirect healthcare costs annually in the United States and accounts for more deaths than any other disease, with coronary artery disease (CAD) being the leading cause of cardiovascular disease-related deaths.[1] The gold standard for assessing CAD, x-ray coronary angiography, is invasive, uses ionizing radiation, and poses a small risk of complications.[2] Coronary magnetic resonance angiography (CMRA) is a potential alternative with several advantages: it does not generate ionizing radiation, it has high spatial resolution in all three dimensions, and it provides high soft-tissue contrast.[2,3] Recent CMRA approaches have used 3D whole-heart protocols[4] for adequate volumetric coverage, with electrocardiogram (ECG) triggering in mid-diastole accounting for cardiac motion, and both respiratory navigators[4] and, more recently, self-navigation[5] have been exploited to compensate for respiratory motion. However, these methods suffer from an inherent operator-dependence, time inefficiency, and complicated workflow.

Recently, a free-running 3D radial data acquisition[6] has been extended with XD-GRASP reconstruction[7] and developed into a fully self-gated free-running framework.[8] The free-running framework has been shown to effectively provide anatomical and functional images of the heart with a highly simplified workflow and high sampling efficiency. To suppress epicardial fat for improved visualization of the coronary arteries, previous work at 1.5T[6] integrated chemical shift-selective (CHESS)[9] fat saturation modules into a periodically interrupted balanced steady-state free precession (bSSFP) sequence, and linearly increasing RF pulses (ramp-up pulses) were added after each CHESS module to reduce artifacts present in the transient phase of bSSFP.[10] The disadvantages of such an approach include an interrupted steady state, a reduced duty cycle, a related time inefficiency, and a high specific absorption rate (SAR).[7]

Lipid-insensitive binomial off-resonant RF excitation (LIBRE) is a recently developed broadband fat suppression technique,[11] consisting of two non-selective off-resonant rectangular RF sub-pulses, which has been shown to provide effective fat suppression and insensitivity to main field (B_0) and RF field (B_1) inhomogeneities. At 3T, LIBRE improved cartilage delineation and the precision of T_2 measurements in vivo in human knees.[12] Furthermore, LIBRE was shown to attenuate lipid signal and improve vessel detection in ECG-triggered self-navigated T_2-prepared CMRA at 3T as part of a gradient-recalled echo imaging sequence.[13] Implemented at 1.5T as part of a bSSFP sequence, LIBRE exhibited robustness to RF field (B_1) inhomogeneities in simulations and in vitro, and it effectively suppressed epicardial fat in vivo in ECG-triggered self-navigated T_2-prepared CMRA.[14] These findings advance the hypothesis that LIBRE could further be integrated into a non-interrupted bSSFP sequence (Figure 1A), as part of the free-running framework, to provide fat-suppressed 5D cardiac images at 1.5T without the need for fat saturation and ramp-up pulses that adversely affect duty cycle, time efficiency, and SAR.

For these reasons, we wanted to implement and optimize LIBRE for non-interrupted free-running bSSFP 5D cardiac MRI at 1.5T, ascertain the magnitude of fat suppression that can be obtained, and test the hypothesis that it achieves quantitative performance comparable to conventional non-interrupted free-running water excitation (WE) and to that of the previously published interrupted free-running (IFR) approach[6] while reducing scan time and SAR. In pursuit of this goal, we performed numerical simulations and explored the parameter space of LIBRE, including the RF excitation angle, RF frequency, and RF pulse duration, to identify optimal LIBRE parameter settings for bSSFP. Subsequently, we performed in vitro experiments for validation of these simulations. We finally conducted an in vivo study where we quantitatively compared the LIBRE results to those obtained from a free-running bSSFP sequence without fat suppression, as a reference, to those obtained from a free-running bSSFP sequence incorporating a 1-2-1 WE, and to those obtained with the previously published IFR approach.[6] Non-interrupted free-running LIBRE results were also compared to conventional ECG-triggered self-navigated images obtained with fat saturation pre-pulses.[15]

2 | METHODS

2.1 | LIBRE background

The LIBRE pulse consists of two rectangular pulses having variable RF frequency (f_{RF}), defined relative to the Larmor frequency, sub-pulse duration (τ), and RF excitation angle (α).[11] Figure 1A contains a basic schematic of the LIBRE pulse, and additional details can be found in Bastiaansen and Stuber.[11] The LIBRE parameters are related by Equation 1[11]:

$$\tau = \sqrt{1 - \left(\frac{\alpha}{2\pi}\right)^2} / (\Delta f + \gamma \Delta B_0), \quad (1)$$

where Δf is the difference between f_{RF} and the precession frequency of the tissue to be suppressed, γ is the gyromagnetic ratio for protons, and ΔB_0 is the local magnetic field inhomogeneity.

2.2 | Pulse parameter optimization using Bloch equation simulations

Previously validated[14] Bloch equation simulations were performed to determine the LIBRE parameter ranges of f_{RF}, τ,
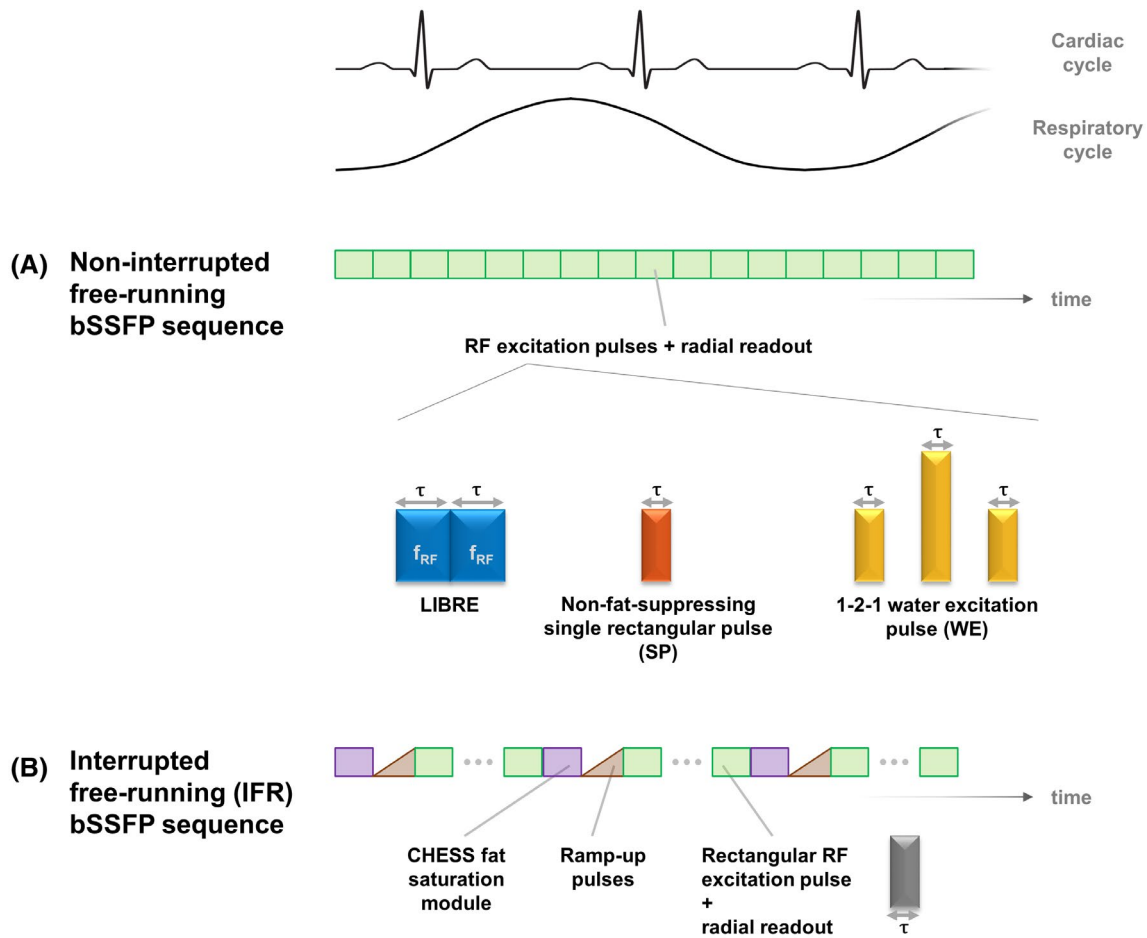
FIGURE 1 Schematic of the (A) non-interrupted and (B) interrupted free-running bSSFP sequences (not to temporal scale), with model cardiac and respiratory cycles. Each green box is symbolic of one repetition time: an RF excitation pulse followed by a radial readout in k-space. f_{RF}, RF frequency; τ, (sub)pulse duration

and α that maximize blood–fat contrast in bSSFP at 1.5T, while ensuring the simulated range for the TR was under 6 ms to minimize the risk of banding artifacts[10] in the heart. The blood–fat contrast was calculated as the difference between blood and fat signal. Blood signal was assumed to be on-resonant, whereas fat signal was modeled using a six-peak fat model as the weighted sum of signals from six chemical off-resonant species.[16,17] Identical relaxation times were assumed for each peak, and both off-resonant frequencies and relative amplitudes can be found in Table 1. The range of investigated τ values was determined by the restriction on TR, as discussed above. α was fixed to a range of 10° to 180°, as SAR limitations effectively prohibit higher RF excitation angles, and the range of f_{RF} values was informed by Equation 1, which was used to provide the midpoint of a 400-Hz-wide range for each value of τ. The LIBRE pulse simulations were compared to those from two other non-spatially-selective RF excitation pulses (Figure 1A): first, to a non-fat-suppressing rectangular excitation pulse (SP) to characterize the magnitude of fat suppression obtained with LIBRE; and second, to another water-selective approach that

permits a non-interrupted free-running acquisition, namely a spectrally-selective RF-phase-modulated 1-90°-2-90°-1 WE pulse. The independent variable was α for SP and WE. Blood–fat contrast was chosen as the optimization criterion for LIBRE and WE. SP was optimized for blood signal, because it does not provide inherent fat suppression. Simulation parameters are found in Table 1. The relaxation times (Table 1) used for the simulations were those of the corresponding compartments in the phantom.

The three optimized pulses were assessed for sensitivity to B_0 and B_1 inhomogeneities by simulating the steady-state transverse magnetization as a function of tissue frequency (Δf_{TISSUE}), which is the precession frequency relative to the Larmor frequency, and α. To measure the effective fat suppression capabilities, the fat suppression band width (FSBW) of each optimized pulse was calculated as the range of fat tissue frequencies encompassing −220 Hz, which corresponds to the dominant peak of the 6-peak fat model above, where the signal was <5% of the on-resonant blood signal. The simulated range of α was the same as in Table 1, and the simulated range of Δf_{TISSUE} was from −500 to +500 Hz.

TABLE 1 RF excitation pulse and sequence parameters for numerical simulations and in vitro and in vivo experiments

	Simulations	In vitro	In vivo
LIBRE			
α (°)	10 to 180	10 to 180	120
τ (ms)	0.5 to 1.5	1.3	1.3
Total excitation duration (ms)	1.0 to 3.0	2.6	2.6
f_{RF} (Hz)	220 to 1900	320 to 720	500
TE/TR (ms/ms)	1.88/3.76 to 2.88/5.76	2.69/5.36	2.75/5.48
Acquisition time (min:s)		00:39	11:33
SP			
α (°)	10 to 180	50	50
τ (ms)	0.3	0.3	0.3
TE/TR (ms/ms)	1.47/2.93	1.47/2.93	1.53/3.05
Acquisition time (min:s)		00:21	6:26
WE			
α (°)	10 to 60	40	40
τ (ms)	0.3	0.3	0.3
Total excitation duration (ms)	2.68	2.68	2.68
TE/TR (ms/ms)	2.66/5.31	2.66/5.31	2.72/5.43
Acquisition time (min:s)		00:39	11:27
IFR			
α (°)			90
τ (ms)			0.3
TE/TR (ms/ms)			1.53/3.05
Acquisition time (min:s)			14:06
Sequence			
Field of view (mm × mm × mm)		180 × 180 × 180	220 × 220 × 220
Iso voxel size (mm)		1.25	1.15
Receiver BW (Hz/pixel)		1021	1042
# radial readouts		7260	126,478
Simulation parameters			
Blood T_1/T_2 (ms/ms)	1439/244		
Fat T_1/T_2 (ms/ms)	154/44		
Fat sub-species resonant frequency [Hz] (relative amplitude [%])	38 (4.7), −32 (3.9), −125 (0.6), −166 (12), −217 (70), −243 (8.8)		
Myocardium T_1/T_2 [ms/ms]	989/33		
Step size [µs]	1		

Abbreviations: α, RF excitation angle; Receiver BW, receiver bandwidth; Iso voxel size, isotropic voxel size; min, minutes; f_{RF}, RF excitation frequency; τ, sub-pulse duration.

2.3 | In vitro experiments

2.3.1 | Data acquisition

To validate the numerically optimized LIBRE parameter ranges, scans were performed on a phantom containing compartments that mimic the relaxation times of blood, fat, and myocardial tissue. First, the in vitro LIBRE bSSFP signal was examined as a function of α and f_{RF}, for $\tau = 1.3$ ms, to ascertain the validity of the numerical simulations. Second, the signals of the different compartments obtained with the optimized LIBRE pulse were compared to those of the optimized SP and WE pulses; the scans were repeated six times for statistical analyses. Scans were performed on a 1.5T scanner (MAGNETOM Aera, Siemens Healthcare AG, Erlangen, Germany) with a prototype 3D radial[18] bSSFP sequence, which was identical

to the non-ECG-triggered free-breathing non-interrupted free-running bSSFP sequence used for the in vivo scans. The reconstruction of each static phantom image was performed using all radial readouts from all coils. RF excitation pulse and sequence parameter ranges are described in Table 1.

2.3.2 | Data analysis

The relative RF pulse performance was validated by measuring the SNR in the blood, fat, and myocardium compartments of the phantom, and the contrast-to-noise ratio (CNR) between blood and fat (blood–fat CNR) and blood and myocardium (blood–myocardium CNR). Regions of interest (ROIs) were manually selected in each of the three compartments in seven consecutive slices in a central region, where the signal appeared homogeneous, using a custom script in MATLAB (The MathWorks, Natick, MA). The SNR was calculated as the ratio of the mean signal over an ROI containing the tissue of interest and the SD of noise over an ROI drawn outside the phantom. The CNR was calculated as the difference of the SNRs of two tissues.

2.4 | In vivo experiments

2.4.1 | Data acquisition and imaging sequences

In this Institutional Review Board-approved study, whole-heart free-running data were collected at 1.5T (MAGNETOM Aera and MAGNETOM Sola, Siemens Healthcare AG) using a 32-channel spine coil array and an 18-channel chest coil array. Data were acquired during free-breathing in 21 volunteers (age: 29 ± 4 y; 11 male) using a fully self-gated prototype non-interrupted free-running 3D radial bSSFP sequence[8] (Figure 1A) incorporating the LIBRE pulse. In eleven of these volunteers, data were additionally acquired using the same sequence where LIBRE was replaced with SP and WE pulses, and, in ten other volunteers, data were collected using the previously published IFR approach[6] (Figure 1B).

The order of the acquisitions was randomly permutated among volunteers to avoid fatigue effects. RF pulse specifications and sequence parameters are provided in Table 1. Scan time and SAR as obtained from the "SAR" or "IEC_WHOLE_BODY" field in the DICOM file were recorded for each in vivo scan. In all cases, radial readouts were arranged in interleaves based on a spiral phyllotaxis pattern,[18] with successive interleaves rotated about the z-axis by the golden angle. The first readout in each interleave was oriented in the superior–inferior (SI) direction for subsequent physiological motion extraction[8] and binning into cardiac and respiratory phases.

In addition to the above non-triggered free-running acquisitions, a third set of images was acquired using a previously reported ECG-triggered self-navigated 3D radial sequence (FS)[15] with T_2-preparation[19] and CHESS fat saturation modules (isotropic field of view = 220 mm; isotropic voxel size = 1.15 mm; α = 90°; TR = 3.3 ms; ~12,000 radial readouts; receiver bandwidth = 685 Hz/pixel) in 2 volunteers (age: 26 and 32 y; 1 male) at 1.5T (MAGNETOM Aera, Siemens Healthcare AG).

2.4.2 | Physiological information extraction and binning

Physiological motion signal extraction was performed as previously described by Di Sopra et al[8] using MATLAB. Briefly, SI projections were obtained by applying the 1D Fast Fourier Transform to SI readouts,[20] which were sampled every 22 readouts, resulting in an effective temporal resolution of ~60 to 120 ms depending on the RF excitation pulse used. Principal component analysis was subsequently performed on these SI projections to extract respiratory signals in a frequency range from 0.1 to 0.7 Hz and cardiac signals in a range from 0.5 to 1.8 Hz. These signals were then used to sort the readouts into non-overlapping cardiac bins with a temporal width of 50 ms, and into four non-overlapping respiratory bins containing equal numbers of readouts, based on the amplitude of the respiratory signal.[8]

2.4.3 | Image reconstruction

The binned k-space data were then reconstructed into motion-resolved images using compressed sensing,[21] as described by Feng et al.[7] Specifically, XD-GRASP[22] solves the following optimization problem while enforcing sparsity along the cardiac and respiratory dimensions:

$$m = \underset{m}{\arg\min} \|F \cdot C \cdot m - d\|_2^2 + \lambda_c \|D_c m\|_1 + \lambda_r \|D_r m\|_1, \tag{2}$$

F is the non-uniform Fast Fourier transform, m is the motion-resolved 5D data set (x, y, z, cardiac, respiratory), C are the coil sensitivities, and d are the sorted k-space data (k_x, k_y, k_z, cardiac, respiratory, coil). D_c and D_r are the first-order difference operators along the cardiac and respiratory dimensions, respectively, and λ_c and λ_r are the respective regularization weights. Both λ_c and λ_r were set to 0.01 for all reconstructions to remove variation in regularization weights as an additional confounder; these values were experimentally found to provide a good trade-off between smoothness in the image domain and in the motion temporal domain in a lower-resolution data set (not shown). No spatial or wavelet

regularization was used. The optimization problem in Equation 2 was solved using the nonlinear conjugate gradient method with backtracking linesearch[7,23]; 36 iterations were used, and the algorithm was restarted every six iterations by taking a gradient step to compensate for the loss of conjugacy of successive gradients. Reconstructions were performed using MATLAB on a workstation with two six-core CPUs (Intel Xeon E5, Intel, Santa Clara, CA), 512 GB of RAM, and an NVIDIA Tesla K40 GPU (Nvidia, Santa Clara, CA).

2.4.4 | Data analysis

The combination of cardiac and respiratory binning resulted in 100 to 120 3D volumes reconstructed for each individual scan. Therefore, one end-expiratory volume corresponding to mid-diastolic quiescence was determined visually and retrospectively selected for subsequent analyses.

In lieu of SNR and CNR analyses, which would not have been feasible due to the noise distribution secondary to the compressed sensing reconstruction, a contrast ratio (CR) analysis was performed for blood–epicardial fat and blood–myocardium. The CR was calculated as the ratio of the mean signals over ROIs drawn in the respective tissues, the first tissue being blood for the case of this analysis. The blood ROI was drawn in the ascending aorta just above the ostium of the right coronary artery (RCA), the epicardial fat ROI was drawn in the fat surrounding the RCA, and the myocardium ROI was drawn in the interventricular septum approximately at mid-level between the RCA ostium and the apex. The ROIs were drawn using the Segment Editor extension in 3D Slicer[24] (http://www.slicer.org).

For LIBRE, SP, WE, and IFR, the number of volunteers in whom proximal segments of a minimum length for the following arteries could be visually identified were counted (minimum length given in parentheses): the RCA (2 cm), the combined left main and left anterior descending coronary arteries (LM + LAD, 2 cm), and the left circumflex coronary artery (LCX, 1 cm). Vessel length and vessel sharpness, both for the first 4 cm and the entire vessel, of the LIBRE, WE, and IFR data sets were determined using SoapBubble[25]; for the LCX, the vessel sharpness for the entire length was computed.

2.4.5 | Statistical analysis

A Wilcoxon rank-sum test, for unpaired data, was used to compare SAR and CR between LIBRE and SP, LIBRE and WE, and LIBRE and IFR; the Bonferroni correction for multiple comparisons was applied. The number of detected arteries between LIBRE and SP (in the subset of 11 volunteers in which both sets of images were acquired), LIBRE and WE (in the subset of 11 volunteers), and LIBRE and IFR (in the subset of 9 volunteers) was compared using NcMemar's test with the Bonferroni correction. Vessel length and vessel sharpness of the RCA, the LM + LAD, and the LCX obtained with LIBRE and WE and LIBRE and IFR were compared using a Wilcoxon rank-sum test with the Bonferroni correction. $P < .05$ was considered statistically significant, and the Bonferroni correction was used where appropriate.

3 | RESULTS

3.1 | Bloch equation simulations

Numerical simulations determined that the LIBRE parameters that optimize blood–fat contrast, while keeping the TR under 6 ms as recommended by Bieri and Scheffler,[10] occurred within a range from $\tau = 1.1$ ms to $\tau = 1.5$ ms (Figure 2), from which the midpoint τ and corresponding f_{RF} and α that maximized blood–fat contrast were taken. Therefore, the optimal parameters were $\tau = 1.3$ ms, $f_{RF} = 540$ Hz, and $\alpha = 120°$ (red dots, Figure 2); the α that maximized blood–fat contrast was 130° by a negligible margin, so 120° was chosen to reduce SAR. It was found that increasing the sub-pulse duration shifted the regions of high blood signal, high blood–fat contrast, and high blood–myocardium contrast toward lower RF excitation angles (Figure 2; full simulation data not shown) and lower SAR by extension. The myocardium signal did not vary significantly over the investigated LIBRE parameter range (Figure 2).

The results of the numerical simulations for WE and SP are shown in Figure 3, where the corresponding LIBRE simulations (for $\tau = 1.3$ ms and $f_{RF} = 540$ Hz) are also shown for the reader's reference. Optimal RF excitation angles of 40° for WE and 50° for SP were found (yellow and red dots, respectively, Figure 3). Although the fat signal for LIBRE and WE remained low and generally independent of the RF excitation angle (Figure 3B), it was similar to that of blood signal for SP over a relatively broad range of RF excitation angles, as fat signal is not suppressed. This can also be seen in Figure 3D, where the difference in signal response between blood and fat is provided as a function of the RF excitation angle: the blood–fat contrast was positive for LIBRE and WE but fluctuated around zero for SP. The myocardium signal for all three RF pulses remained relatively low over the investigated range of RF excitation angles (Figure 3C), leading to a high blood–myocardium signal difference around 50° for SP and WE (Figure 3E), where blood signal was high for both SP and WE, and around 160° for LIBRE, whose blood signal plateaued above 100°.
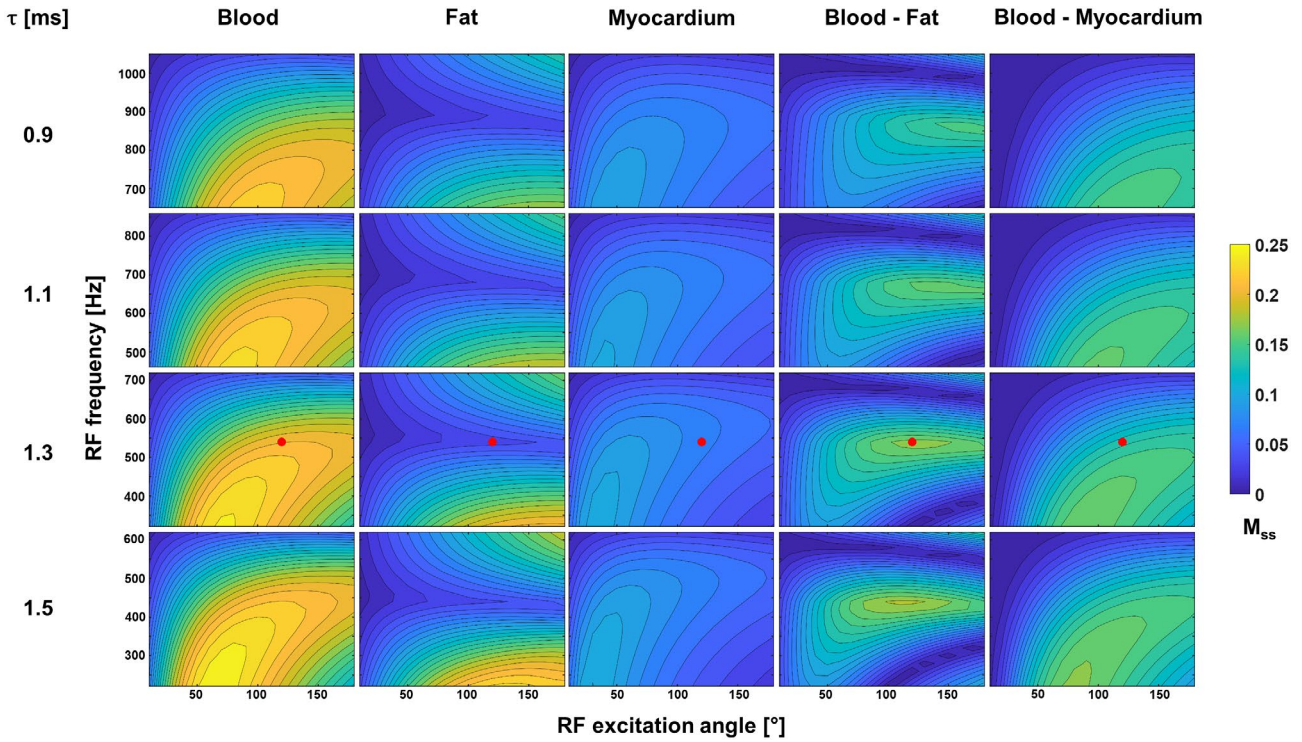
FIGURE 2 Theoretical LIBRE signal behavior. Transverse steady-state magnetization (M_{ss}), as a function of RF excitation angle and frequency (relative to the Larmor frequency) for different sub-pulse durations (τ) of the LIBRE pulse, for blood, fat (6-peak model), myocardium, blood–fat contrast, and blood–myocardium contrast. The red dot indicates the chosen optimal parameters, which maximize the blood–fat contrast
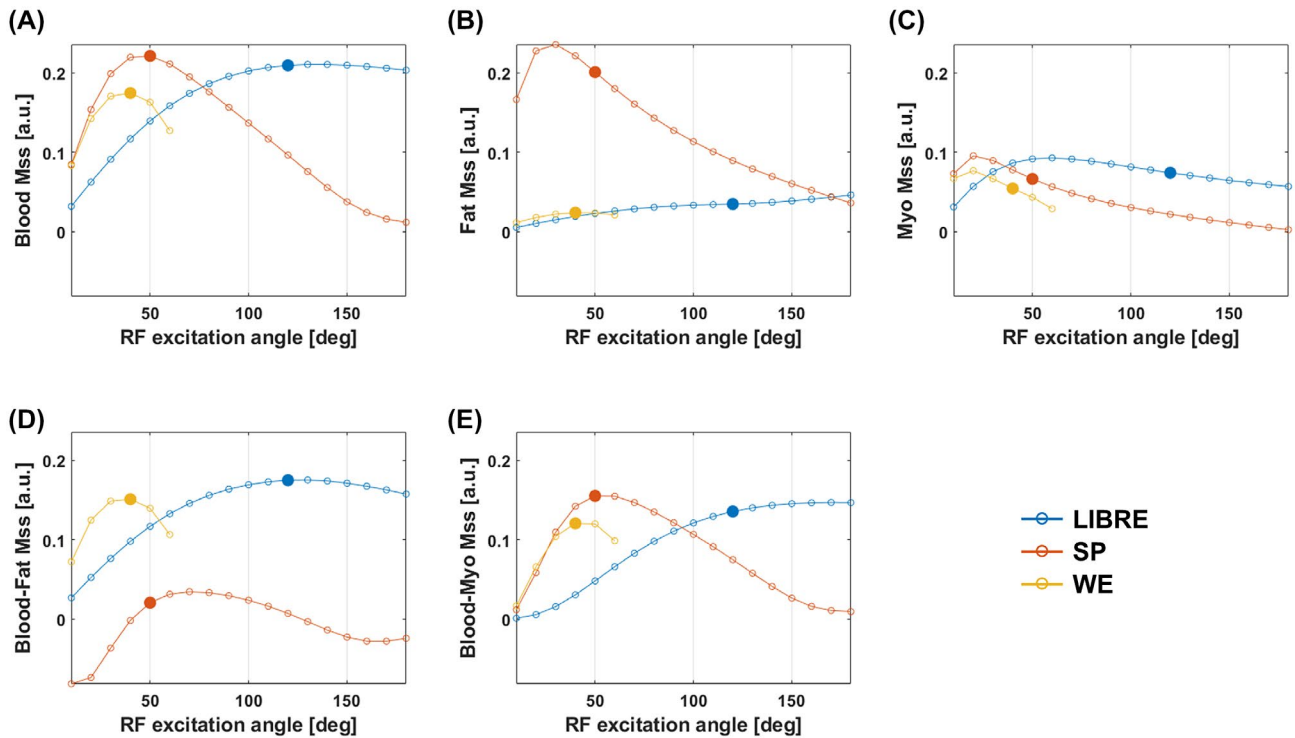
FIGURE 3 Theoretical LIBRE ($\tau = 1.3$ ms, $f_{RF} = 540$ Hz), SP, and WE signal behavior. Transverse steady-state magnetization (M_{ss}) as a function of RF excitation angle for (A) blood, (B) fat (6-peak model), (C) myocardium, (D) blood–fat contrast, and (E) blood–myocardium contrast. The blue and yellow dots indicate the LIBRE and WE parameters, respectively, that optimize blood–fat contrast, and the red dot indicates the SP parameters that optimize blood signal

Figure 4 presents the steady-state transverse magnetization of blood for the three numerically optimized pulses as a function of tissue frequency and RF excitation angle, to enable an assessment of their relative sensitivities to B_0 and B_1 inhomogeneities. Each pulse exhibited the TR-dependent signal dropout that leads to banding artifacts in bSSFP images (orange arrows, Figure 4). The white lines indicate the respective numerically optimized RF excitation angles for each pulse (Figure 4). Examining this signal profile around 0 Hz (water), we see that both LIBRE (Figure 4A) and WE (Figure 4C) possess a slight sensitivity to variations in tissue frequency (B_0 inhomogeneities). Following the black line labeled "water" or alternatively Figure 4D, which both show on-resonant signal variation due to changes in the RF excitation angle (B_1 inhomogeneities), we see that LIBRE signal exhibited the lowest RF excitation angle-dependence of the three pulses (Figure 4A). Both LIBRE and WE reduced signal around the fat frequency in an RF excitation angle-independent manner, as indicated by the region of reduced signal around the black line labeled "fat" (Figure 4A,C). The calculated FSBW values support this observation: SP had an FSBW of 0 Hz, whereas LIBRE had an FSBW of 21 Hz and WE had an FSBW of 58 Hz. In fact, the reported FSBW corresponds to the range of tissue frequencies along the white line, and centered around −220 Hz, where the signal is <5% of the water signal. Although SP does not suppress tissue around −220 Hz, there is a band at approximately −170 Hz (Figure 4B), which might cause signal reductions in fat regions in vivo.

3.2 | In vitro experiments

The results of the LIBRE optimization (Figure 5) and comparison of the optimized LIBRE, SP, and WE pulses (Figure 6) were highly consistent between simulations and in vitro
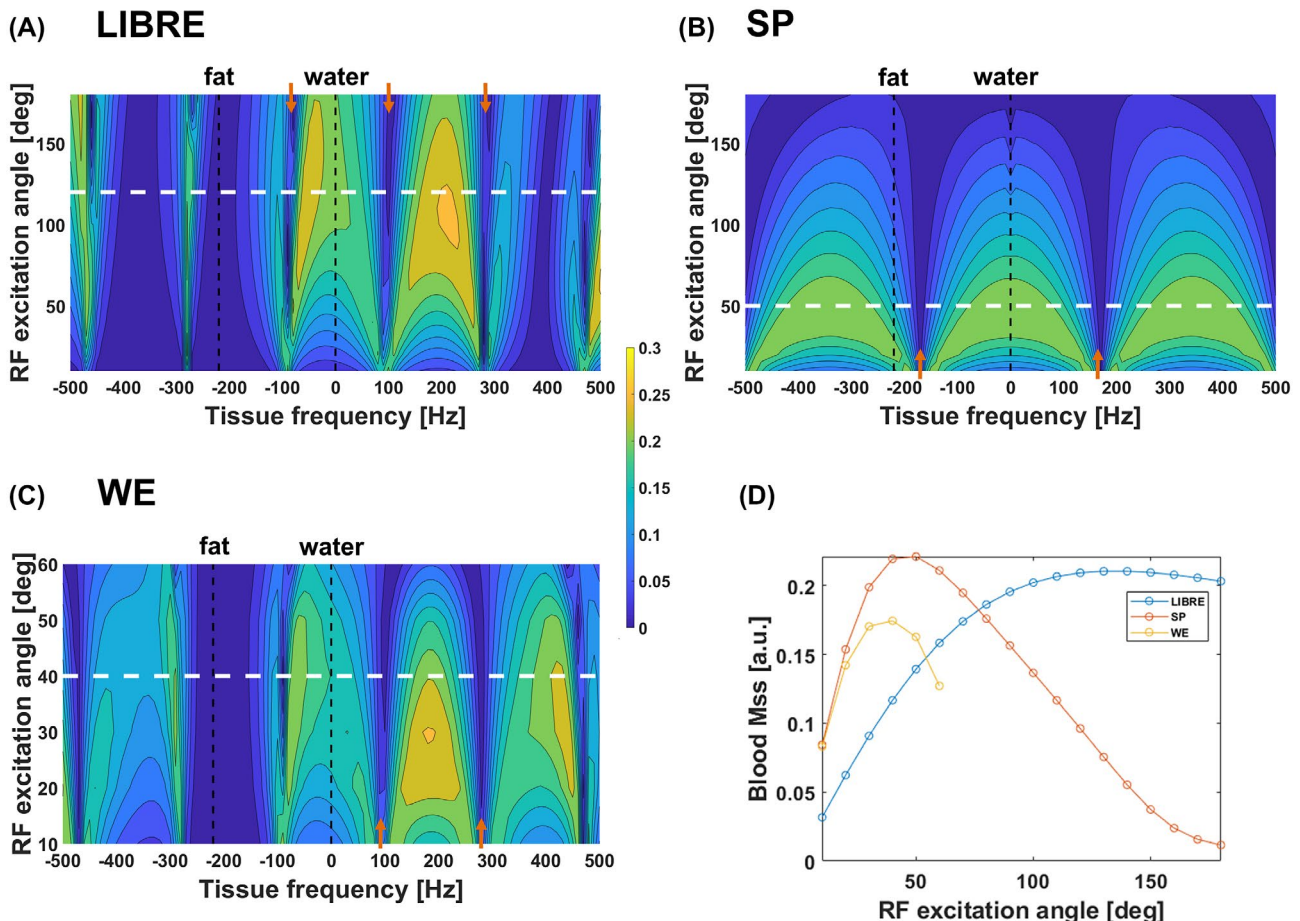
FIGURE 4 Effect of B_0 and B_1 inhomogeneities. Transverse steady-state magnetization as a function of tissue frequency and RF excitation angle for blood tissue, for the (A) LIBRE, (B) SP, and (C) WE RF excitation pulses. (D) Transverse steady-state magnetization (M_{ss}) as a function of RF excitation angle for on-resonant blood tissue for LIBRE, SP, and WE. In (A)-(C), water (0 Hz) and fat (−220 Hz) resonant frequencies are indicated with dashed black lines; the orange arrows indicate banding artifacts; and the numerically optimized RF excitation angle for each pulse is indicated by the white dashed lines. Pulse parameters are those found under "In vitro" in Table 1; specifically, for LIBRE, the RF frequency (f_{RF} = 540 Hz) and sub-pulse duration (τ = 1.3 ms) used the numerically optimized values

(A)

(B)

—○— **Simulation**   --◎-- **In vitro**
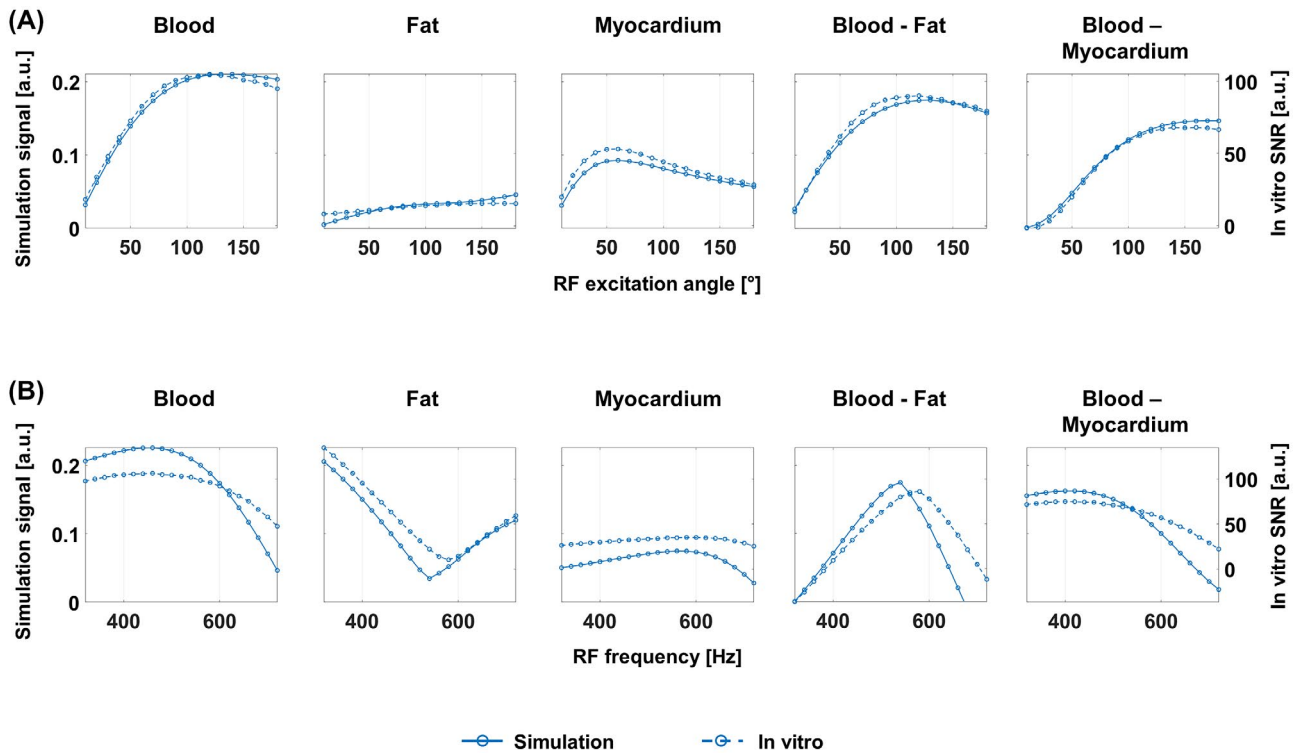
FIGURE 5 Comparison of simulated (transverse steady-state magnetization; solid line) and in vitro (dashed line) LIBRE bSSFP signal. Blood, fat, and myocardium signal, and blood–fat and blood–myocardium contrast, are shown as a function of (A) RF excitation angle and (B) RF frequency (relative to the Larmor frequency). The simulation scale is on the left side of the plots and the in vitro SNR scale is on the right side

■ **LIBRE**   ■ **SP**   ■ **WE**
□ **Simulation**   ▨ **In vitro**
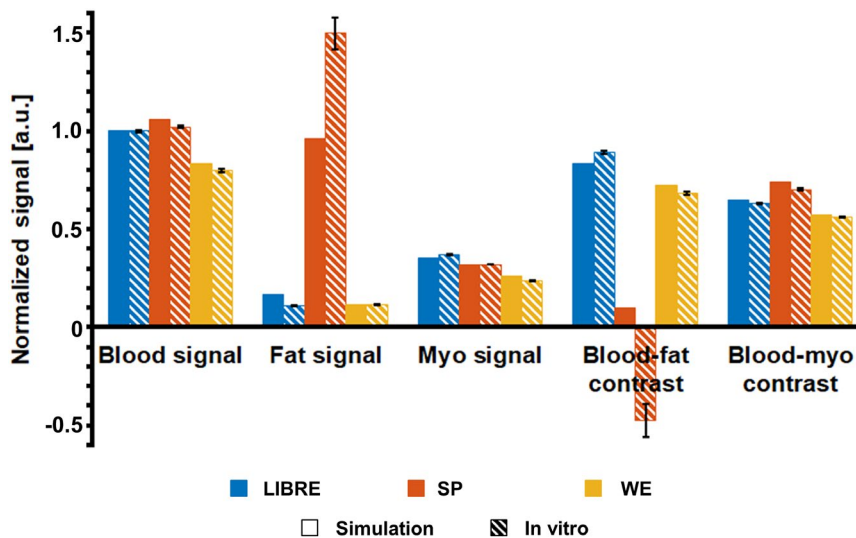
FIGURE 6 Comparison of simulated (transverse steady-state magnetization) and in vitro bSSFP signal. Blood, fat, and myocardium (myo) signal, and blood–fat and blood–myocardium contrast, are displayed for LIBRE, SP, and WE. Solid bars indicate simulation values and bars with white dashed lines indicate in vitro values. The mean value of the six in vitro repetitions is indicated by the bar height, and the standard deviation is indicated by the error bars. The data have been normalized to the blood signal of LIBRE for both cases: 0.2093 for the simulation data and 85.90 for the in vitro data

scans. The shapes of corresponding LIBRE signal profiles as functions of α (Figure 5A) and f_{RF} (Figure 5B) are similar between simulations and in vitro scans. In particular, the α and f_{RF} that were predicted by the simulations to maximize LIBRE blood–fat contrast had deviations of 0° and 40° Hz,

respectively, with respect to the in vitro scans (Figure 5A,B). The relative signal and contrast of the optimized pulses was generally consistent between simulations and in vitro scans (Figure 6). The only exception was that the fat signal of SP was higher in vitro than that of the simulations and higher

than in vitro blood signal, leading to a negative blood–fat contrast that contradicts the near-zero contrast predicted by simulations. Figure 6 indicates that LIBRE was the only pulse to simultaneously provide high blood signal and fat suppression and had, consequently, the highest blood–fat contrast.

3.3 | In vivo experiments

Fat-suppressed cardiac-and-respiratory-motion-resolved 3D images were successfully reconstructed from in vivo free-running whole-heart data (Supporting Information Videos S1 and S2), although the acquired data for one volunteer were discarded due to scanner malfunction. Therefore, the sample size was $N = 20$ for LIBRE and $N = 9$ for IFR. Reconstruction time ranged from 5–8 h. Respiratory displacement and both cardiac contraction and relaxation of the heart were well-resolved (Supporting Information Videos S1 and S2). The quantitative results are shown in Table 2. Acquisition times were 11 min 33 s for LIBRE, 11 min 27 s for WE, 6 min 26 s for SP, and 14 min 06 s for IFR (Table 1). They were constant and independent of respiratory patterns and heart rates. The SAR for LIBRE was 0.57 ± 0.04 W/kg, which was significantly lower than that of SP (1.56 ± 0.14 W/kg; $P < .001$),

WE (0.98 ± 0.09 W/kg; $P < .001$), and IFR (2.43 ± 0.30 W/kg, $P < .001$) (Table 2).

LIBRE provided uniform epicardial fat suppression and improved delineation of coronary arteries relative to SP and WE (Figure 7). With WE, epicardial fat suppression was less consistent (yellow arrows, Figure 7), which, coupled with poor blood signal, led to regionally impaired coronary artery delineation when compared to LIBRE (red arrows, Figure 7). SP was naturally unable to suppress fat (yellow arrows, Figure 7), which often led to an inability to delineate the coronary arteries. However, using SP, some segments of the coronary arteries were visible occasionally, which can be attributed to water–fat signal out-of-phase cancellations in voxels containing both tissues (green arrows, Figure 7).

LIBRE provided more uniform fat suppression and similar blood signal compared to FS and IFR (Figure 8). Although LIBRE blood signal is similar to that of IFR in both examples, LIBRE epicardial fat suppression is superior and more consistent (yellow arrows, Figure 8). Moreover, LIBRE reformats do not exhibit the water–fat signal out-of-phase cancellation artifacts that are characteristically seen in IFR reformats (green arrows, Figure 8), although these artifacts are also visible in the very distal part of the LM + LAD of volunteer B with LIBRE. Suppression of subcutaneous fat in

TABLE 2 Summary of in vivo results

	LIBRE	SP	WE	IFR
SAR (W/kg)	0.57 ± 0.04	1.56 ± 0.14*	0.98 ± 0.09*	2.43 ± 0.30*
Contrast ratio				
Blood–fat	3.9 ± 1.8	1.1 ± 0.5*	2.7 ± 1.3	1.2 ± 0.7*
Blood–myocardium	1.7 ± 0.5	1.5 ± 0.2	1.6 ± 0.4	1.1 ± 0.1*
RCA				
Detection rate	19/20	3/11*	10/11	6/9
Vessel length (cm)	9.7 ± 4.0		8.0 ± 4.0	9.6 ± 5.3
% VS first 4 cm	54.5 ± 10.6		46.5 ± 12.7	45.3 ± 10.1
% VS	47.1 ± 10.2		44.6 ± 13.2	40.8 ± 6.9
LM+LAD				
Detection rate	19/20	3/11	10/11	4/9
Vessel length (cm)	7.4 ± 2.8		8.1 ± 1.8	6.4 ± 1.8
% VS first 4 cm	48.6 ± 12.5		47.5 ± 10.2	39.4 ± 3.8
% VS	51.5 ± 10.2		50.7 ± 10.2	42.1 ± 6.8
LCX				
Detection rate	16/20	3/11*	8/11	1/9
Vessel length (cm)	2.8 ± 1.0		2.9 ± 1.1	3.1
% VS	42.4 ± 7.0		39.9 ± 6.0	42.1

Abbreviations: LAD, left anterior descending coronary artery; LM, left main coronary artery; LCX, left circumflex coronary artery; min, minutes; RCA, right coronary artery; SAR, specific absorption rate.

Data are presented as mean $\pm$ SD, except for the coronary artery detection rates. Asterisks (*) indicate statistically significant differences in the comparison with LIBRE data. For the vessel sharpness analysis (vessel length, % VS first 4 cm, % VS), no comparison between LIBRE and SP data was performed, as mentioned in the Methods.
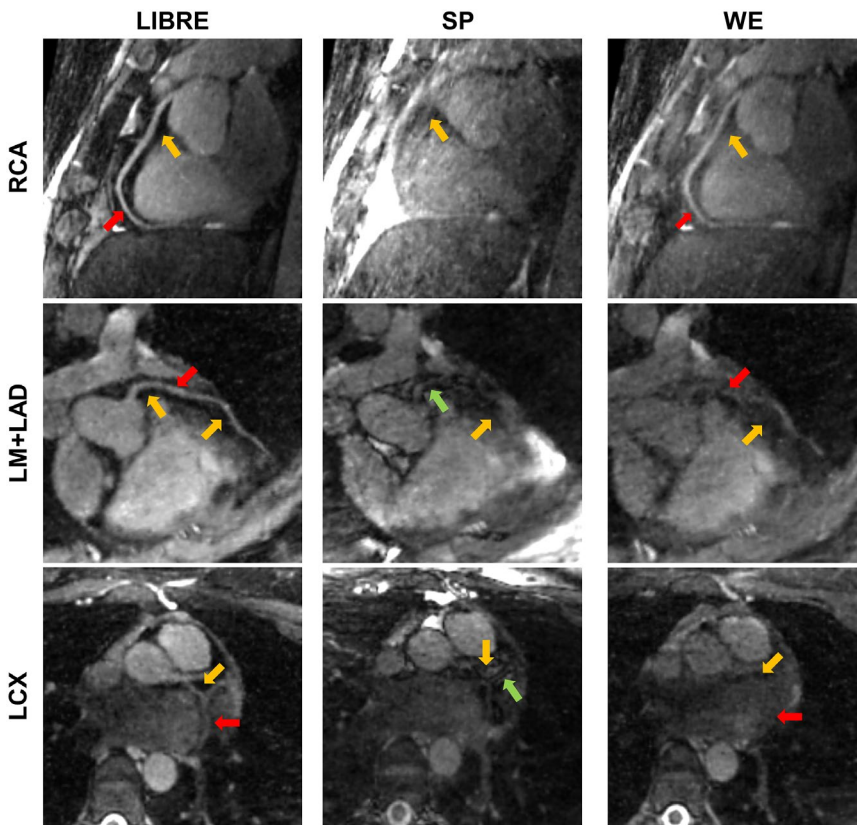
FIGURE 7 Free-running reformatted images of the right coronary artery (RCA), left main and left anterior descending artery (LM + LAD), and left circumflex artery (LCX), obtained with LIBRE, SP, and WE RF excitation pulses. Yellow arrows indicate regions of epicardial fat, red arrows indicate (expected) coronary artery edges, and green arrows show water-fat phase cancellation artifacts
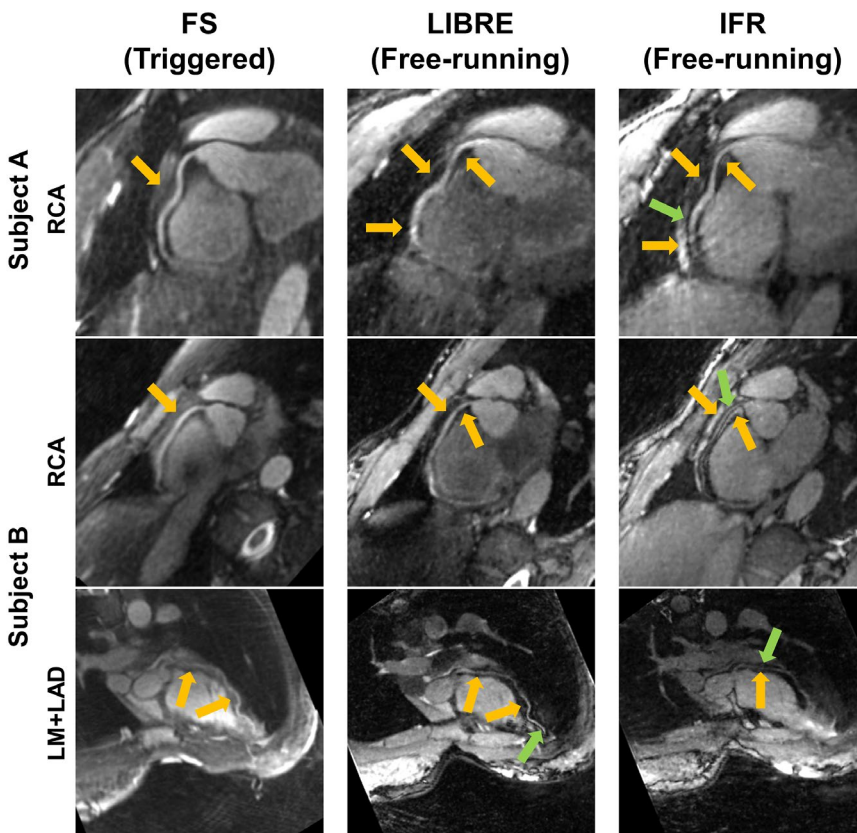
FIGURE 8 Comparison of non-interrupted free-running LIBRE images (LIBRE) with images using an ECG-triggered self-navigated fat-saturated T_2-prepared 3D radial acquisition (FS) and images using the previously published interrupted free-running acquisition (IFR) that is periodically interrupted by fat saturation and ramp-up pulses. Shown are reformatted images of the right coronary artery (RCA) and the left main and left anterior descending coronary artery (LM + LAD) acquired with the three sequences for two volunteers, A and B. Yellow arrows indicate regions of epicardial fat, and green arrows show water-fat phase cancellation artifacts

the chest wall by LIBRE also appears to be more consistent than that of IFR. Blood signal of FS appears to be slightly superior to that of LIBRE in both cases, although fat signal appears to be more consistently suppressed with LIBRE, both around the coronary arteries (yellow arrows, Figure 8), as well as in the chest wall.

The contrast ratios of the three approaches are shown in Table 2. LIBRE had the highest blood–fat and blood–myocardium CR, with statistical significance reached for the comparison of blood–fat CR with SP ($P < .001$) and IFR ($P < .001$) and for the comparison of blood–myocardium CR with IFR ($P < .001$).

Detection rates, vessel length, and vessel sharpness of the RCA, LM + LAD, and LCX are also shown in Table 2, where the results of the statistical comparisons between LIBRE and SP, WE, and IFR are also displayed. LIBRE was able to detect the RCA and LM + LAD in 19/20 volunteers and the LCX in 16/20 volunteers, which was higher than those of the other three methods, with statistical significance reached in the comparison with SP for the RCA and LCX. Vessel sharpness values measured in the first 4 cm and for the entire vessel length were highest with LIBRE for all three coronary arteries. LIBRE had the highest vessel length for the RCA, and a vessel length for the LCX that was similar to those of WE and IFR. However, the vessel length of the LM + LAD measured by LIBRE was lower than that of WE but higher than that of IFR.

4 | DISCUSSION

We successfully incorporated LIBRE RF excitation pulses into a non-interrupted bSSFP sequence to enable fat-suppressed 3D motion-resolved whole-heart coronary MRA at 1.5T using the free-running framework. Numerical optimization of the LIBRE pulse parameters was validated in vitro in phantoms, and informed the parameter ranges for subsequent in vivo scans. Compared to SP, WE, and IFR, LIBRE provided both high blood signal and suppressed fat signal. In vivo, LIBRE scan time was similar to that of WE, approximately twice as long as that of SP, and 18% shorter than that of IFR. LIBRE significantly reduced SAR values compared to SP, WE, and IFR. LIBRE had significantly greater blood–fat CR than SP and the coronary arteries were visible more often. LIBRE improved blood–fat CR and increased the vessel sharpness of all three coronary arteries relative to WE. Compared to the previously published IFR, LIBRE significantly improved blood–fat CR, had higher detection rates for all three vessels, and maintained vessel length and improved vessel sharpness for the RCA and LM + LAD.

4.1 | Water-selective RF excitation pulses in bSSFP

There have been few uses of water-selective RF excitation pulses in non-interrupted bSSFP acquisitions in the literature. Binomial WE pulses have been used in bSSFP sequences for musculoskeletal imaging at 1.5T and 3T.[26-28] Spectral–spatial

RF pulses have been used for abdominal imaging with bSSFP at 3T.[29] With regards to cardiac imaging, we were unable to find any studies involving water-selective excitation in non-interrupted bSSFP acquisitions, although Pang et al[30] used binomial 1-2-1 WE pulses in a non-interrupted gradient-recalled echo sequence for free-breathing post-contrast 4D CMRA at 3T. Therefore, to the best of our knowledge, this study demonstrates the first successful use of a WE technique in a non-interrupted bSSFP sequence for a dynamic application.

4.2 | Numerical simulations

The simulations performed in this study, and that incorporate a 6-peak fat model, provide some insights about the LIBRE pulse. The results help contextualize a previous study that used a shorter LIBRE sub-pulse duration of 0.7 ms where it was concluded that blood signal remained to be optimized.[14] In fact, increasing the sub-pulse duration reduced the off-resonant RF frequency required for effective fat suppression, which was also found in Bastiaansen et al,[11] with the benefit that on-resonant blood and myocardium signals were increased (Figure 2). This observation guided the choice of LIBRE parameters used in this study. Coincidentally, increasing the sub-pulse duration, and thus the total pulse duration, reduced SAR values at the expense of a slight increase in TR. Compared to SP, LIBRE and WE have a TR that is almost twice as long (Table 1), implying that there is a time cost for fat suppression. Naturally, the increase in TR comes at an increased risk of banding artifacts localized in the region of the heart. Furthermore, although the fat signal, and, consequently, blood–fat contrast, appears to be sensitive to variations in the RF excitation frequency (Figure 2), the practical likelihood of variations in RF frequency is low, as RF synthesizers can generally generate waveforms with the desired frequency with very high accuracy.

The in vitro and in vivo findings point to the merits of numeric optimization using Bloch equation simulations and the 6-peak fat model. The Bloch equation simulations used in this study have been validated previously[14] and are able to model relevant theoretical bSSFP signal characteristics described in the literature.[10] Simulations predicted that LIBRE would have the highest blood–fat contrast, which was confirmed in vitro (Figure 6) and produced in vivo images with the highest vessel sharpness and highest blood–fat contrast ratio (Table 2). There were cases where the simulations did not perfectly match the in vitro or in vivo behavior. The in vitro fat signal of SP was higher than theoretically predicted (Figure 6), and there were slight discrepancies between simulated LIBRE signal behavior and that in vitro (Figure 5). In both cases, the fact that each tissue was modelled with only a single T_1 and T_2, and a limited number of off-resonance values (reflecting B_0 inhomogeneities), could have contributed

to such minor differences. With regards to the high in vitro SP fat signal, it is possible that higher proton density in the fat compartment of the phantom could have caused such high signal, which the simulations, assuming constant proton densities, would not have been able to predict without further information. Furthermore, the lower FSBW of LIBRE compared to WE did not appear to be reflected in the vessel sharpness values, but might explain the lower vessel lengths of the LM + LAD and LCX in LIBRE images compared to WE images. Numerical simulations suggested that LIBRE had higher blood–fat contrast, which may explain the higher vessel sharpness values, but it had a lower FSBW than WE, meaning that fat suppression would have been less consistent in areas further away from the isocenter and the heart, where vessel diameter gradually decreases due to branching and B_0 inhomogeneities become more severe, potentially affecting the discernible vessel length. Nevertheless, numerical simulations with even simple models, such as those used here, can guide in vivo parameter settings by predicting optimal pulse parameters and characterizing signal.

One potential drawback of the present numerical simulations is that the relaxation times were those of the phantom, rather than in vivo values. Retrospectively, we performed numerical simulations using the same six-peak fat model as before but with relaxation times for blood,[31] fat,[32] and myocardium[33,34] that were measured in vivo. The results for the numerical optimization of LIBRE are presented in Supporting Information Figure S1, and the results of the numerical optimization of SP and WE are presented in Supporting Information Figure S2. The optimal parameters for SP and WE (Supporting Information Figure S2) did not change compared to the current simulations (Figure 3), although, for $\tau = 1.3$ ms, the optimal LIBRE parameters were $\alpha = 140°$ and $f_{RF} = 540$ Hz (Supporting Information Figure S1), which represents a 20° change for α. These results indicate that the behavior of these three pulses is relatively insensitive to the choice of relaxation times, and that the present simulations were sufficiently accurate for modelling pulse behavior in vitro and in vivo.

Finally, the fat model used here provides insights into pulse optimization for CMRA. The three main peaks of the present fat model, at −166 Hz, −217 Hz, and −243 Hz (Table 1), all fall within the region of tissue frequencies suppressed by LIBRE and WE (Figure 4). Furthermore, an in vivo myocardial triglyceride spectroscopy study noted that epicardial lipids exhibited a peak at −3.1 ppm that was not detected in myocardial lipids,[35] which would correspond to −198 Hz at 1.5T. The fact that both LIBRE and WE suppressed signal at all four of these resonant frequencies (Figure 4) could explain why they were generally able to suppress epicardial fat in vivo for CMRA, and provides guidance for future studies as to the range of fat frequencies that need to be suppressed for successful CMRA. Furthermore, to account for in vivo variation in lipid composition, future studies should ensure

that a range of fat frequencies, centered around −3.1 ppm and −3.4 ppm, are suppressed.

4.3 | 3D whole-heart CMRA approaches

This study included a comparison with a previously reported free-running bSSFP sequence that is periodically interrupted for fat suppression.[6] LIBRE scan time was reduced by 18% when compared to IFR (Table 1). While LIBRE affords the advantage of removing the fat saturation and ramp-up prepulses, the TR is inherently increased, and therefore the gain in scanning time is modest. However, SAR was reduced by 77% relative to IFR (Table 2). LIBRE provides more consistent fat signal suppression both around the RCA and LM + LAD as well as in the anterior chest when compared to IFR (Figure 8). Moreover, LIBRE provides vessel delineation through blood–fat contrast alone, whereas vessel delineation in IFR images appears to have been largely due to and artificially overemphasized by the presence of water-fat phase cancellation artifacts, as the mean blood–fat CR of 1.2 indicated little difference between blood and epicardial fat signal in IFR images. These artifacts, which were frequently seen in the present IFR images (full data not shown) and also retrospectively in images in Coppo et al,[6] and Feng et al,[7] generate sharp vessel edges that artificially increase vessel sharpness values, and likely account for the similarity in vessel sharpness values between LIBRE and IFR data despite the qualitatively superior fat suppression observed in the LIBRE images.

With regard to the comparison with the ECG-triggered self-navigated FS method, the free-running LIBRE approach has several advantages. Preliminary examination in two volunteers suggests that LIBRE provides more consistent fat suppression, whereas FS provides slightly higher blood signal. The higher blood signal may be due to the ECG triggering, as the trigger delay would allow for magnetization recovery. A more comprehensive quantitative study would be necessary for concrete conclusions. On a more general level, the LIBRE approach uses all readouts, thereby increasing sampling efficiency, and providing motion-resolved 5D images rather than respiratory-motion-corrected 3D images. The free-running LIBRE approach also greatly reduces operator-dependence relative to FS, because the need for the ECG set-up is eliminated.

Finally, although we did not compare our non-interrupted free-running LIBRE approach with conventional ECG-triggered,[36] navigator-gated,[37,38] fat-saturated, T_2-prepared[19,39] 3D Cartesian CMRA, we will proceed with a brief discussion of the two approaches. The conventional approach provides motion-corrected images through the use of ECG triggering in mid-diastole for cardiac motion compensation and the use of respiratory navigators for respiratory motion correction, with T_2-preparation used to improve blood–myocardium contrast and fat saturation to improve blood–fat contrast.

Conversely, our free-running non-interrupted LIBRE bSSFP approach provides cardiac- and respiratory-motion-resolved images without the need for ECG or navigators, with blood–myocardium contrast intrinsically provided by bSSFP[2] and fat signal attenuation through LIBRE. The benefit of our approach is that it provides isotropic motion-resolved 3D images with a simplified workflow—eliminating the need to apply the ECG and position the navigator—while scanning time is constant and independent of heart rate or respiratory patterns. The sampling efficiency is high at around 30%, as all the data, whose acquisition accounts for ~30% of the scan duration, are used to reconstruct the 5D images. Conversely, the conventional ECG-triggered and navigator-gated approach suffers from a significantly reduced sampling efficiency of 2% only, because data used for image reconstruction are only collected when both favorable cardiac and respiratory phases coincide. In addition, the acquisition time of the conventional approach can be unpredictable and vary because of many factors, including the low acceptance rate of the respiratory gating,[15] positioning of the navigator,[40] and changes in the respiratory[41] or cardiac cycle[6] during the scan. However, like FS, the conventional approach potentially benefits from higher SNR as the ECG trigger delay allows for magnetization recovery. Furthermore, the use of T_2-preparation provides increased blood–myocardium contrast, but this increase may be offset to a certain degree by the intrinsic blood–myocardium contrast of bSSFP.[2]

4.4 | Study limitations

The study methodology contained some shortcomings. The LIBRE pulse was compared to a 1-2-1 WE pulse that was available on the scanner, and, apart from an RF excitation angle optimization, no further optimization of this pulse was performed. Recent work has demonstrated that fast interrupted steady-state (FISS)[42] can be exploited for fat-saturated 5D free-running cardiac imaging,[43,44] and a comparison with the present approach would be very instructive. The reconstruction pipeline, including regularization weights, was identical for LIBRE, SP, WE, and IFR, although optimal regularization weights are expected to vary as each acquisition will have slightly different noise levels and residual aliasing. The identification of the mid-diastolic phase was done visually and separately for each data set, without consideration of coronary artery vessel length or sharpness. Therefore, coronary artery visualization for these data could potentially be further improved through the use of pulse-specific regularization weights and a more quantitative approach for extracting the mid-diastolic resting phase.

Furthermore, this study did not measure cardiac function. However, LIBRE acquisitions can potentially provide cardiac functional information, as previous studies involving free-breathing 3D radial bSSFP or gradient-recalled echo acquisitions, with[7] and without[6,30] compressed sensing reconstructions, showed good agreement with 2D cine acquisitions in terms of left ventricular end-systolic volumes, end-diastolic volumes, and ejection fraction.

5 | CONCLUSIONS

The LIBRE pulse was numerically optimized and successfully used for fat-suppressed fully self-gated non-interrupted free-running 5D bSSFP cardiac MRI at 1.5T. In vivo, LIBRE improved blood–fat contrast and vessel sharpness and maintained vessel length relative to non-interrupted free-running WE and the previously published IFR, while reducing scan time and SAR relative to IFR. LIBRE could potentially offer motion-resolved coronary MRA and functional imaging of the heart at high spatial resolution, with a simplified workflow compared to more conventional cardiac MRI protocols.

ORCID

Nemanja Masala https://orcid.org/0000-0003-1193-4557
Jessica A. M. Bastiaansen https://orcid.org/0000-0002-5485-1308
Lorenzo Di Sopra https://orcid.org/0000-0003-3426-9457
Christopher W. Roy https://orcid.org/0000-0002-3111-8840
Davide Piccini https://orcid.org/0000-0003-4663-3244
Jérôme Yerly https://orcid.org/0000-0003-4347-8613
Matthias Stuber https://orcid.org/0000-0001-9843-2028

TWITTER

Matthias Stuber @CVMR_Lausanne

REFERENCES

1. Benjamin EJ, Muntner P, Alonso A, et al. Heart disease and stroke statistics—2019 update: A report from the American heart association. *Circulation*. 2019;135:e146–e603.
2. Stuber M, Weiss RG. Coronary magnetic resonance angiography. *J Magn Reson Imaging*. 2007;26:219–234.
3. Dweck MR, Puntmann VO, Vesey AT, Fayad ZA, Nagel E. MR imaging of coronary arteries and plaques. *JACC Cardiovasc Imaging*. 2016;9:306–316.
4. Sakuma H, Ichikawa Y, Chino S, Hirano T, Makino K, Takeda K. Detection of coronary artery stenosis with whole-heart coronary magnetic resonance angiography. *J Am Coll Cardiol*. 2006;48:1946–1950.
5. Piccini D, Monney P, Sierro C, et al. Respiratory self-navigated postcontrast whole-heart coronary MR angiography: Initial experience in patients. *Radiology*. 2014;270:378–386.
6. Coppo S, Piccini D, Bonanno G, et al. Free-running 4D whole-heart self-navigated golden angle MRI: Initial results. *Magn Reson Med*. 2015;74:1306–1316.
7. Feng LI, Coppo S, Piccini D, et al. 5D whole-heart sparse MRI. *Magn Reson Med*. 2018;79:826–838.

8. Di Sopra L, Piccini D, Coppo S, Stuber M, Yerly J. An automated approach to fully self-gated free-running cardiac and respiratory motion-resolved 5D whole-heart MRI. *Magn Reson Med*. 2019;82:2118–2132.

9. Haase A, Frahm J, Hanicke W, Matthaei D. 1H NMR chemical shift selective (CHESS) imaging. *Phys Med Biol*. 1985;30:341–344.

10. Bieri O, Scheffler K. Fundamentals of balanced steady state free precession MRI. *J Magn Reson Imaging*. 2013;38:2–11.

11. Bastiaansen JAM, Stuber M. Flexible water excitation for fat-free MRI at 3T using lipid insensitive binomial off-resonant RF excitation (LIBRE) pulses. *Magn Reson Med*. 2018;79:3007–3017.

12. Colotti R, Omoumi P, van Heeswijk RB, Bastiaansen JAM. Simultaneous fat-free isotropic 3D anatomical imaging and T2mapping of knee cartilage with lipid-insensitive binomial off-resonant RF excitation (LIBRE) pulses. *J Magn Reson Imaging*. 2018;1–10.

13. Bastiaansen JAM, van Heeswijk RB, Stuber M, Piccini D. Noncontrast free-breathing respiratory self-navigated coronary artery cardiovascular magnetic resonance angiography at 3 T using lipid insensitive binomial off-resonant excitation (LIBRE). *J Cardiovasc Magn Reson*. 2019;21:38.

14. Masala N, Bastiaansen JAM, Piccini D, Stuber M. Fat suppression in 3D bSSFP coronary MRA using lipid-insensitive binomial off-resonant RF excitation (LIBRE) pulses. In Proceedings of the Society for Cardiovascular Magnetic Resonance 22nd Annual Scientific Sessions, Bellevue, USA, 2019. Abstract 550699.

15. Piccini D, Littmann A, Nielles-Vallespin S, Zenge MO. Respiratory self-navigation for whole-heart bright-blood coronary MRI: Methods for robust isolation and automatic segmentation of the blood pool. *Magn Reson Med*. 2012;68:571–579.

16. Hamilton G, Yokoo T, Bydder M, et al. In vivo characterization of the liver fat 1H MR spectrum. *NMR Biomed*. 2011;24:784–790.

17. Wang X, Hernando D, Reeder SB. Sensitivity of chemical shift-encoded fat quantification to calibration of fat MR spectrum. *Magn Reson Med*. 2016;75:845–851.

18. Piccini D, Littmann A, Nielles-Vallespin S, Zenge MO. Spiral phyllotaxis: The natural way to construct a 3D radial trajectory in MRI. *Magn Reson Med*. 2011;66:1049–1056.

19. Brittain JH, Hu BS, Wright GA, Meyer CH, Macovski A, Nishimura DG. Coronary angiography with magnetization-prepared T2 contrast. *Magn Reson Med*. 1995;33:689–696.

20. Stehning C, Börnert P, Nehrke K, Eggers H, Stuber M. Free-breathing whole-heart coronary MRA with 3D radial SSFP and self-navigated image reconstruction. *Magn Reson Med*. 2005;54:476–480.

21. Donoho DL. Compressed sensing. *IEEE Trans Inf Theory*. 2006;52:1289–1306.

22. Feng L, Axel L, Chandarana H, Block KT, Sodickson DK, Otazo R. XD-GRASP: Golden-angle radial MRI with reconstruction of extra motion-state dimensions using compressed sensing. *Magn Reson Med*. 2016;75:775–788.

23. Lustig M, Donoho D, Pauly JM. Sparse MRI: The application of compressed sensing for rapid MR imaging. *Magn Reson Med*. 2007;58:1182–1195.

24. Fedorov A, Beichel R, Kalpathy-Cramer J, et al. 3D Slicer as an image computing platform for the quantitative imaging network. *Magn Reson Imaging*. 2012;30:1323–1341.

25. Etienne A, Botnar RM, Van Muiswinkel AMC, Boesiger P, Manning WJ, Stuber M. "Soap-Bubble" visualization and quantitative analysis of 3D coronary magnetic resonance angiograms. *Magn Reson Med*. 2002;48:658–666.

26. Kornaat PR, Doornbos J, van der Molen AJ, et al. Magnetic resonance imaging of knee cartilage using a water selective balanced steady-state free precession sequence. *J Magn Reson Imaging*. 2004;20:850–856.

27. Duc SR, Koch P, Schmid MR, Horger W, Hodler J, Pfirrmann CWA. Diagnosis of articular cartilage abnormalities of the knee: Prospective clinical evaluation of a 3D water-excitation true FISP sequence. *Radiology*. 2007;243:475–482.

28. Ribot EJ, Wecker D, Trotier AJ, et al. Selective imaging and bSSFP banding artifact correction in humans and small animals at 3T and 7T, respectively. Zhang H, ed. *PLoS ONE*. 2015;10:e0139249.

29. Yuan J, Madore B, Panych LP. Fat–water selective excitation in balanced steady-state free precession using short spatial–spectral RF pulses. *J Magn Reson*. 2011;208:219–224.

30. Pang J, Sharif B, Fan Z, et al. ECG and navigator-free four-dimensional whole-heart coronary MRA for simultaneous visualization of cardiac anatomy and function. *Magn Reson Med*. 2014;72:1208–1217.

31. Stanisz GJ, Odrobina EE, Pun J, et al. T1, T2 relaxation and magnetization transfer in tissue at 3T. *Magn Reson Med*. 2005;54:507–512.

32. de Bazelaire CMJ, Duhamel GD, Rofsky NM, Alsop DCMR. Imaging relaxation times of abdominal and pelvic tissues measured in vivo at 3.0 T: Preliminary results. *Radiology*. 2004;230:652–659.

33. Chow K, Flewitt JA, Green JD, Pagano JJ, Friedrich MG, Thompson RB. Saturation recovery single-shot acquisition (SASHA) for myocardial T 1 mapping. *Magn Reson Med*. 2014;71:2082–2095.

34. Sprinkart AM, Luetkens JA, Träber F, et al. Gradient spin echo (GraSE) imaging for fast myocardial T2 mapping. *J Cardiovasc Magn Reson*. 2015;17:12.

35. Szczepaniak LS, Dobbins RL, Metzger GJ, et al. Myocardial triglycerides and systolic function in humans: In vivo evaluation by localized proton spectroscopy and cardiac imaging. *Magn Reson Med*. 2003;49:417–423.

36. Edelman RR, Manning WJ, Burstein D, Paulin S. Coronary arteries: Breath-hold MR angiography. *Radiology*. 1991;181:641–643.

37. Ehman RL, Felmlee JP. Adaptive technique for high-definition MR imaging of moving structures. *Radiology*. 1989;173:255–263.

38. Li D, Kaushikkar S, Haacke EM, et al. Coronary arteries: Three-dimensional MR Imaging with retrospective respiratory gating. *Radiology*. 1996;201:857–863.

39. Botnar RM, Stuber M, Danias PG, Kissinger KV, Manning WJ. Improved coronary artery definition with T2-weighted, free-breathing, three-dimensional coronary MRA. *Circulation*. 1999;99:3139–3148.

40. Stuber M, Botnar RM, Danias PG, Kissinger KV, Manning WJ. Submillimeter three-dimensional coronary MR angiography with real-time navigator correction: Comparison of navigator locations. *Radiology*. 1999;212:579–587.

41. Taylor AM, Jhooti P, Firmin DN, Pennell DJ. Automated monitoring of diaphragm end-expiratory position for real-time navigator echo MR coronary angiography. *J Magn Reson Imaging*. 1999;9:395–401.

42. Koktzoglou I, Edelman RR. Radial fast interrupted steady-state (FISS) magnetic resonance imaging. *Magn Reson Med*. 2018;79:2077–2086.

43. Küstner T, Bustin A, Jaubert O, Neji R, Prieto C, Botnar R. 3D Cartesian fast interrupted steady-state (FISS) imaging. *Magn Reson Med*. 2019;82:1617–1630.

44. Bastiaansen JAM, Piccini D, Di Sopra L, et al. Natively fat-suppressed 5D whole-heart MRI with a radial free-running fast-interrupted steady-state (FISS) sequence at 1.5T and 3T. *Magn Reson Med*. 2020;83:45–55.

SUPPORTING INFORMATION

Additional Supporting Information may be found online in the Supporting Information section.

FIGURE S1 Theoretical LIBRE signal behavior modelled using relaxation times measured in vivo. Transverse steady-state magnetization (M_{ss}), as a function of RF excitation angle and frequency (relative to the Larmor frequency) for different sub-pulse durations (τ) of the LIBRE pulse, for blood, fat (6-peak model), myocardium, blood–fat contrast, and blood–myocardium contrast

FIGURE S2 Theoretical LIBRE ($\tau = 1.3$ ms, $f_{RF} = 540$ Hz), SP, and WE signal behavior modelled using relaxation times measured in vivo. Transverse steady-state magnetization (M_{ss}) as a function of RF excitation angle for (A) blood, (B) fat (6-peak model), (C) myocardium, (D) blood–fat contrast, and (E) blood–myocardium contrast

VIDEO S1 Animation derived from one free-running LIBRE data set showing respiratory motion at mid-diastole for one 3.5-mm-thick slice in transverse, coronal, and sagittal orientations. Epicardial fat was consistently suppressed, which allowed visualization of the coronary arteries, even though fat was not necessarily homogeneously suppressed throughout the FOV

VIDEO S2 Animation derived from one free-running LIBRE data set showing cardiac motion at end-expiration for one 3.5-mm-thick slice in transverse, coronal, and sagittal orientations. Epicardial fat was consistently suppressed, which allowed visualization of the coronary arteries, even though fat was not necessarily homogeneously suppressed throughout the FOV
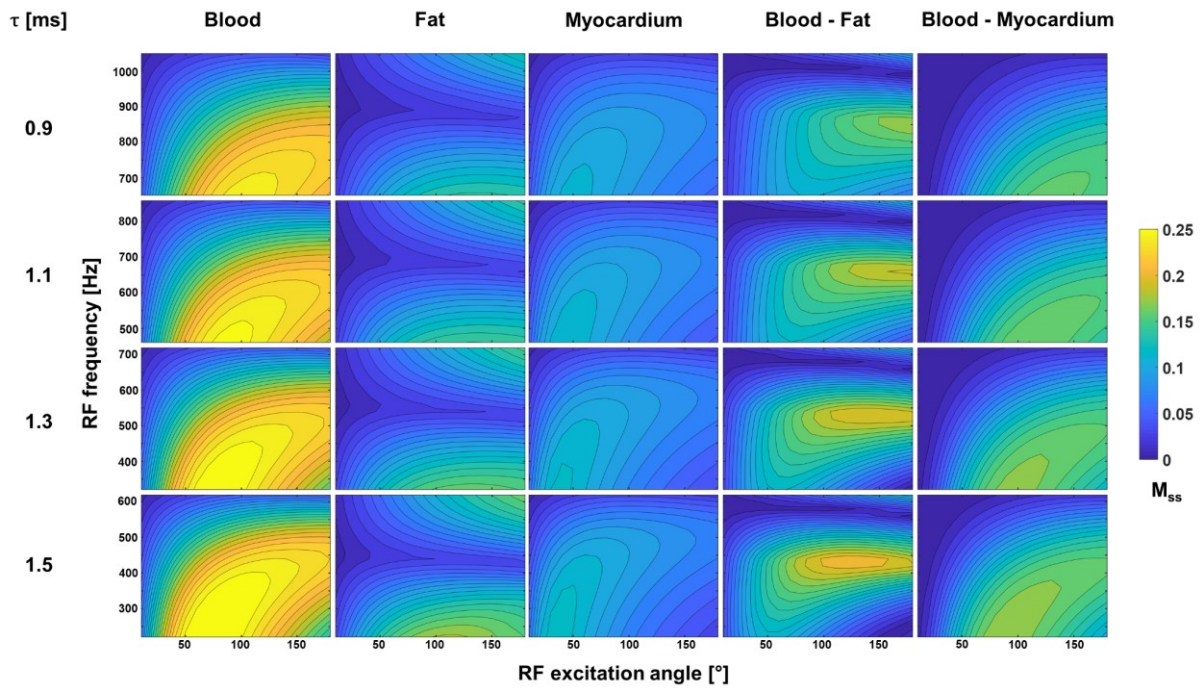
Supporting Information Figure S1: Theoretical LIBRE signal behavior modelled using relaxation times measured in vivo. Transverse steady-state magnetization (M_{ss}), as a function of RF excitation angle and frequency (relative to the Larmor frequency) for different sub-pulse durations (τ) of the LIBRE pulse, for blood, fat (6-peak model), myocardium, blood-fat contrast, and blood-myocardium contrast.

Supporting Information Figure S2: Theoretical LIBRE ($\tau = 1.3$ ms, $f_{RF} = 540$ Hz), SP, and WE signal behaviour modelled using relaxation times measured in vivo. Transverse steady-state magnetization (M_{ss}) as a function of RF excitation angle for A) blood, B) fat (6-peak model), C) myocardium, D) blood-fat contrast, and E) blood-myocardium contrast.

2.4 Free-running bSSFP coronary MRA with LIBRE pulses and fast(er) fNAV reconstruction

The study in Section 2.3 achieved fully self-gated uninterrupted free-running 5D coronary MRA by integrating LIBRE pulses into a bSSFP sequence. The free-running LIBRE approach reduced scan time and SAR compared to the interrupted acquisition, and maintained image quality and vessel conspicuity relative to the interrupted IFR and uninterrupted WE free-running acquisitions. However, the reconstruction time of the XD-GRASP technique for these datasets was between 5 and 8 hours, which would have been prohibitively long for allowing prompt assessment by clinicians during patient scans. Recent work in the lab had led to the development of an autofocusing approach (121) called focused navigation (fNAV) (122,123) that estimated non-rigid respiratory motion from the SI projection of the 3D radial phyllotaxis trajectory (48). In ECG-triggered 3D radial coronary MRA (37) of volunteers and patients, fNAV reconstruction significantly improved vessel sharpness compared to reconstructions using rigid motion correction or XD-GRASP. This advanced the notion that fNAV could be successfully used for 3D coronary MRA of the free-running 5D LIBRE acquisitions while reducing the reconstruction time, as fNAV does not require compressed sensing and instead iteratively minimizes a metric of image quality. A colleague, Giulia Rossi, was responsible for translating fNAV to 5D acquisitions by implementing an additional correction for cardiac motion. fNAV was first used for non-rigid intra-bin correction of respiratory motion of the undersampled 5D dataset, and then five cardiac phases manually selected from the resulting 4D dataset were co-registered, generating a 3D motion-corrected image for each 5D dataset. The conference abstract, which was accepted to the Virtual Scientific Sessions 2021 of the Society for Cardiovascular Magnetic Resonance (SCMR), is presented below.

2.4.1 Personal contribution

I was the second author of this study. I provided the raw data, the computed motion signals, and the XD-GRASP reconstructions to the first author, Giulia Rossi.

2.4.2 Peer-reviewed conference abstract

A copy of the abstract is reproduced here with permission from the SCMR.

Focused navigation for free-running respiratory and cardiac motion-corrected 3D whole-heart coronary MRA.

Giulia MC Rossi[1], Nemanja Masala[1], Jessica AM Bastiaansen[1], Aurelien Bustin[1,3], John Heerfordt[1,4], Davide Piccini[1,4], Matthias Stuber[1,2], Christopher W Roy[1]

[1]Department of Radiology, Lausanne University Hospital (CHUV) and University of Lausanne (UNIL), Switzerland [2]Center for Biomedical Imaging (CIBM), Lausanne, Switzerland [3]LIRYC (Electrophysiology and Heart Modeling Institute), Bordeaux, France. [4]Advanced Clinical Imaging Technology (ACIT), Siemens Healthcare AG, Lausanne, Switzerland

Background

Coronary Magnetic Resonance Angiography (CMRA) requires robust compensation of both respiratory and cardiac motion. Recently, an auto-focusing technique (fNAV) **[1]** was proposed for intra-acquisition non-rigid correction of respiratory motion in 3D radial ECG-triggered CMRA acquisitions. In this work, we present a novel method for CMRA that integrates fNAV with an uninterrupted bSSFP acquisition using LIBRE water excitation pulses **[2-4]** as part of the free-running framework **[5-6]**. We test the hypothesis that, a) by using fNAV to correct for respiratory motion and b) image registration to correct for residual cardiac motion, we can obtain high-quality images of coronary arteries without the need for compressed sensing (CS). We quantitatively compare our approach to the previously established cardiac-and-respiratory-resolved 5D imaging in vivo.

Methods

CMRA data were acquired in 9 healthy volunteers (age: 23-34 y; 5 male) on a 1.5T MAGNETOM Sola (Siemens Healthcare, Erlangen, Germany) with a previously described prototype free-running acquisition (**Fig.1A**) **[4]**. For each volunteer, we reconstructed 5D images as previously reported **[4-6],** extracted quiescent 3D images (**Fig.1B**), and compared those to fNAV reconstructions (**Fig.1C**). For both methods, reconstruction times were recorded. Curved reformats of the right coronary artery (RCA) were obtained from the resulting 3D images and visually compared. Quantitative comparison of image quality was performed via evaluation of RCA percentage vessel sharpness (%VS) and visible length using Soap-Bubble **[7]** and by blood-to-myocardium contrast ratio (CR) measurements using 3DSlicer **[8]**. Statistical significance was evaluated using paired t-tests.

Results

Overall, fNAV images were visually comparable to 5D images (**Fig.2**), with reconstruction times of 32-52 minutes and 5-8 hours **[4]**, respectively. Reformats of the RCA were also similar; however, the fNAV approach provided improved visual vessel conspicuity at specific locations (**Fig.3**). Quantitative comparisons (**Table1**) confirmed preserved CR and comparable visible RCA length, and no statistically significant difference in %VS.

Discussion and Conclusion

By combining fNAV and image registration, fully motion-corrected CMRA images can be obtained from free-running acquisitions without the need for CS, leading to similar image quality in significantly shorter reconstruction times. In patient populations where un-resolved intra-bin motion may be further amplified and degrade image quality of cardiac-and-respiratory-resolved 5D imaging, our approach may be particularly beneficial, but this remains to be studied. Sources of improvement can be sought in the optimization of quiescent cardiac data selection and subsequent image registration. If sufficient SNR gain could be achieved whilst preserving %VS, the increased amount of signal could be traded for higher resolution or abbreviated scan times, potentially improving the current diagnostic ability of 3D radial CMRA in the assessment of coronary artery disease.

References

[1] Roy, C. W., Heerfordt J., Piccini, D., Schwitter, J., & Stuber, M. Motion Compensated Coronary MRA using Focused Navigation (fNAV). *Proc. Intl. Soc. Mag. Reson. Med*. 28 1321 (2020).

[2] Bastiaansen, J. A., & Stuber, M. (2018). Flexible water excitation for fat-free MRI at 3T using lipid insensitive binomial off-resonant RF excitation (LIBRE) pulses. *Magnetic resonance in medicine*, *79*(6), 3007-3017.

[3] Bastiaansen, J. A., van Heeswijk, R. B., Stuber, M., & Piccini, D. (2019). Noncontrast free-breathing respiratory self-navigated coronary artery cardiovascular magnetic resonance angiography at 3 T using lipid insensitive binomial off-resonant excitation (LIBRE). *Journal of Cardiovascular Magnetic Resonance*, *21*(1), 38.

[4] Masala, N., Bastiaansen, J. A., Di Sopra, L., Roy, C. W., Piccini, D., Yerly, J., ... & Stuber, M. (2020). Free-running 5D coronary MR angiography at 1.5 T using LIBRE water excitation pulses. *Magnetic resonance in medicine*, *84*(3), 1470-1485.

[5] Di Sopra, L., Piccini, D., Coppo, S., Stuber, M., & Yerly, J. (2019). An automated approach to fully self-gated free-running cardiac and respiratory motion-resolved 5D whole-heart MRI. *Magnetic resonance in medicine*, 82(6), 2118-2132.

[6] Feng, L. I., Coppo, S., Piccini, D., Yerly, J., Lim, R. P., Masci, P. G., ... & Otazo, R. (2018). 5D whole-heart sparse MRI. *Magnetic resonance in medicine*, *79*(2), 826-838.

[7] Etienne, A., Botnar, R. M., Van Muiswinkel, A. M., Boesiger, P., Manning, W. J., & Stuber, M. (2002). "Soap-Bubble" visualization and quantitative analysis of 3D coronary magnetic resonance angiograms. *Magnetic Resonance in Medicine: An Official Journal of the International Society for Magnetic Resonance in Medicine*, *48*(4), 658-666.

[8] Fedorov, A., Beichel, R., Kalpathy-Cramer, J., Finet, J., Fillion-Robin, J. C., Pujol, S., ... & Buatti, J. (2012). 3D Slicer as an image computing platform for the Quantitative Imaging Network. *Magnetic resonance imaging*, 30(9), 1323-1341.
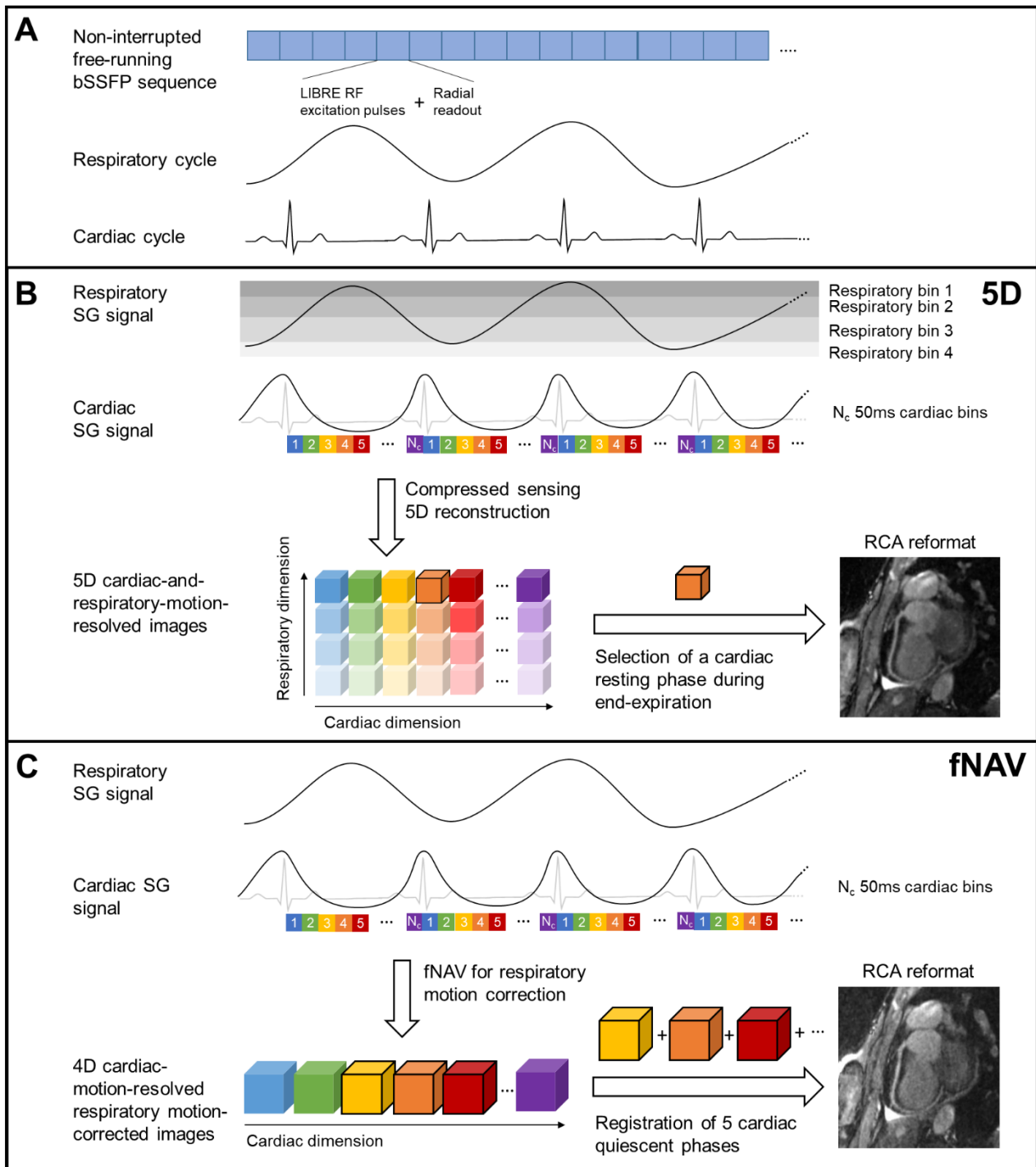
Figure 1. Overview of the methods. **A**: Schematic of the prototype free-running acquisition comprising lipid-insensitive binomial off-resonant RF excitation (LIBRE) pulses for water-excitation**.** **B**: Schematic of the reconstruction pipeline for 5D image reconstruction. Self-gating (SG) signals extracted from the data are used to bin the data into four respiratory bins and a variable number (N_c) of 50 ms cardiac bins (N_c was in the range 16-21 for the 9 subjects). Cardiac-and-respiratory-motion-resolved 5D images are reconstructed with CS and a final 3D image representing a cardiac resting phase during end-expiration is manually selected for curved reformatting of the right coronary artery (RCA) **C**: Schematic of the reconstruction pipeline for the proposed fNAV-based reconstruction. fNAV

is used for intra-acquisition non-rigid correction of respiratory motion for each cardiac phase creating cardiac-motion-resolved 4D respiratory motion-corrected images. Image registration of five manually chosen cardiac phases is then performed using NiftyReg, and results in a 3D image used for curved reformatting of the RCA. The number of cardiac phases to register was empirically fixed to five based on a trade-off between SNR and sharpness.
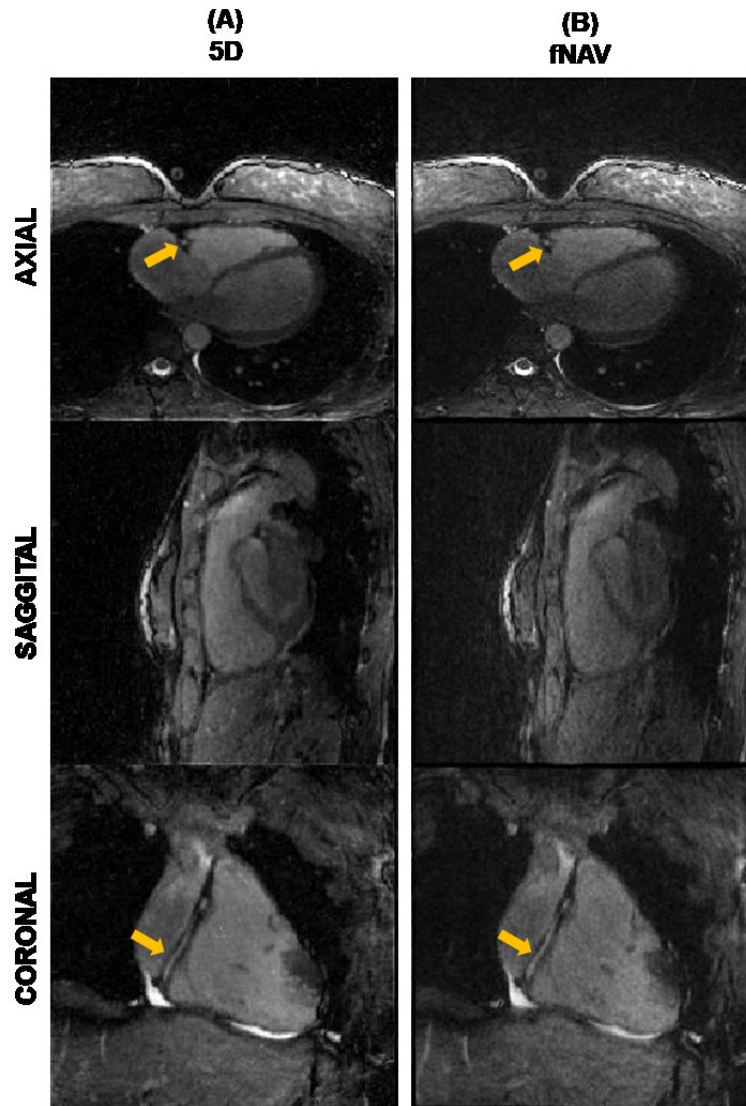
Figure 2. Qualitative comparison between 5D and fNAV-based reconstruction. Representative images in axial, sagittal, and coronal orientations are shown for a mid-diastolic end-expiration phase in the reference 5D reconstruction **(A)** and for the proposed fNAV reconstruction **(B)**. Yellow arrows indicate locations where a portion of the right coronary artery is visible.
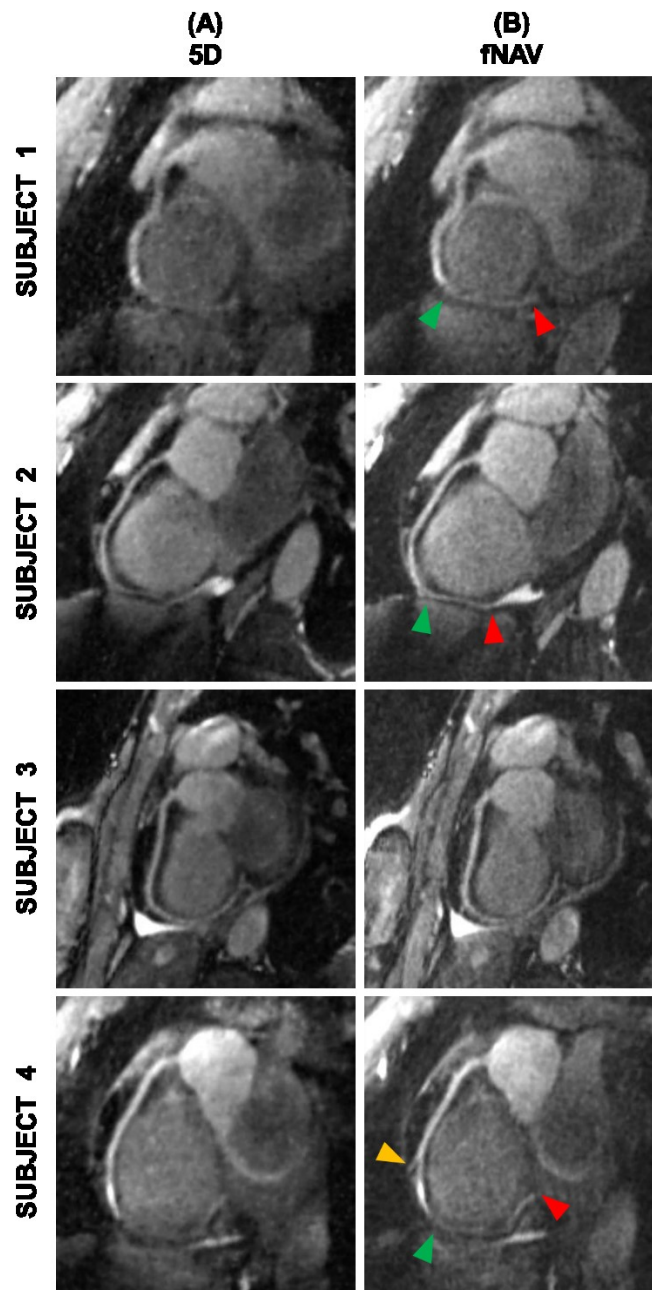
Figure 3. Reformatted images of the right coronary artery (RCA). Reformatted images of the RCA obtained with Soap-Bubble are shown for four representative volunteers for the reference 5D reconstruction **(A)** and for the proposed fNAV-based reconstruction **(B)**. Arrows indicate RCA branches (yellow) or segments (green: beginning of the segment, red: end of the segment) for which the fNAV-based reconstruction approach allowed for improved detail visibility.

	5D	fNAV
CR blood-myocardium	1.36 ± 0.16	1.35 ± 0.21
RCA detection rate	8/9	8/9
RCA Vessel length (cm)	8.47 ± 2.95	8.34 ± 3.09
RCA %VS (first 4 cm)	42.5 ± 8.1	40.4 ± 9.8
RCA %VS (full length)	39.4 ± 7.3	37.8 ± 7.5

Table 1. Quantitative comparison between 5D and fNAV-based reconstructions. Abbreviations: CR, contrast ratio; RCA, right coronary artery; VS, vessel sharpness. Data are presented as mean ± SD, except for detection rates. RCA was considered detected if >2cm were visible. None of the differences were found to be statistically significant at a 0.05 significance level (paired t-test). p-values were 0.88, 0.88, 0.20 and 0.08 for CR blood-myocardium, RCA vessel length, RCA %VS (4 cm) and RCA %VS (full length), respectively.

2.5 Discussion

LIBRE pulses were successfully optimized and used for coronary MRA at 1.5T in an uninterrupted bSSFP sequence (Section 2.3), without the need for contrast agent injection, ECG set-up, or respiratory belts. LIBRE reduced SAR and improved blood-fat contrast in vivo compared to all other examined sequences, and compared to the previously-published interrupted free-running (IFR) approach (40), it reduced scan time by 18%. The free-running LIBRE approach maintained image quality and vessel conspicuity compared to the free-running IFR and WE approaches. In addition to the discussion in the article, the blood-myocardium contrast of the uninterrupted bSSFP sequences was higher than that of IFR, indicating that the inherent blood-myocardium contrast of bSSFP was compromised by interrupting the steady-state. This was also the first time that an uninterrupted 3D bSSFP sequence had been used in cardiac MRI or in any other dynamic application. Finally, the use of fNAV reconstruction (Section 2.4) reduced the reconstruction time by eight-fold while maintaining image quality.

A further extension would involve the extraction of functional information from the LIBRE free-running approach. Reference ejection fraction cine scans were acquired during the original study and it would be informative to see whether ejection fraction calculated from the 5D images matches the reference values. Moreover, an intermediate step of the fNAV reconstruction for 5D data involves the generation of a 4D cardiac-resolved dataset, which could be used for the calculation of ejection fraction, offering the potential for combined anatomical and functional imaging with the simplified workflow of the free-running framework and the reduced reconstruction time of fNAV. However, we currently lack the computational tools to automatize ejection fraction calculation in 5D datasets, and, more generally, to efficiently take advantage of the large amount of data contained in multidimensional datasets. The current challenge with calculating ejection fraction from 5D data is that both the reformatting of the images to the correct orientation and the segmentation of the left ventricle are largely manual steps. A current industrial collaboration has as one of its aims to improve the ease of analyzing 5D images.

Some of the shortcomings of the free-running LIBRE approach will be discussed in this paragraph. In this study, the LIBRE pulse was numerically optimized for blood-fat contrast, although the final choice of parameters was somewhat arbitrary because it was largely based on attempting to reach similar blood signal as a 1-180°-1 binomial pulse, which may have been a suboptimal criterion. For example, it remains to be seen

whether a slight decrease of the subpulse duration would be able to maintain vessel conspicuity while reducing scan time and TR, including the risk of banding artefacts. In addition, while the B_0 and B_1 sensitivity of the LIBRE pulse were examined with these simulations, they were not verified quantitatively in vitro. It would be interesting to see whether the in vitro signal measured as a function of B_0 inhomogeneities from a B_0 map or as a function of B_1 inhomogeneities from a B_1 map matches the predictions of the simulations. As an example, the frequency response of the LIBRE pulse was asymmetric, so a B_0 map would be able to reveal the effect of this asymmetry on in vitro or vivo signal and whether it needs to be mitigated. Finally, the algorithm for the selection of parameters could be optimized. A single-peak fat model was initially used (Figure 16), consisting of the dominant peak in the six-peak model, and it was during the review process that the simulations were re-done with the six-peak model that went into the article. The optimal parameters using the six-peak model did not change, aside from the optimal RF angle increasing from 120° to 130°. However, as mentioned in the Discussion in the article, the fat suppression band of LIBRE encompassed four likely dominant peaks of epicardial fat, which may explain why it still successfully suppressed fat in vivo. We were unable to find studies that discussed the variability of the locations or amplitudes of each of the peaks in the spectral domain nor was the multi-peak nature of fat often considered in the literature, aside from notably the IDEAL technique (99), yet such information could be used to replace the peaks in the simulations with distributions and potentially yield a parameter set that provides more robust in vivo blood signal and suppressed fat signal. Knowing the distribution of fat peaks among a healthy or patient population could provide a probability of how often those parameters would yield effective fat suppression in vivo. In vivo B_0 distributions for the heart could also be included in such a model. The numerically-optimized parameters for the study were validated in vitro, and then the RF frequency was further optimized in vivo in three volunteers, as the blood-fat contrast was more susceptible to variations in RF frequency. Interestingly, however, the optimal RF frequency in vitro was higher than that from the simulations, which was higher than the in vivo optimal value, indicating that care should be taken in choosing the data on which to base the pulse parameter optimization. It remains to be seen whether theoretical multi-peak models like those discussed above can entirely replace the need for an in vivo calibration.

The determination of the motion signals could also be improved. Although the default self-gating algorithm determined the three principal components with the highest powers in the respective spectral frequency bands and then selected the one with the lowest index, the cardiac principal component with the "best" cardiac signal was often

the one with the highest spectral power in that band, rather than the one with the lowest index. Moreover, the temporal frequency spectrum of the SI projections acquired with the LIBRE pulse tended to have very strong trajectory-dependant peaks that were not completely removed by the trajectory-dependant frequency component filtering (54). Motion signals producing clear motion-resolved images could always be successfully extracted from LIBRE datasets, although it remains to be seen whether the impact of these trajectory components can be reduced. The use of a non-trajectory-based motion signal, such as the Pilot-Tone (124), may represent one potential avenue. In addition, referring to the comment in the Discussion of the article about a quantitative way of determining the quiescent cardiac phase, current work in the lab is attempting to do that in combination with the fNAV technique.

Coronary MRA with the free-running LIBRE approach has the potential for clinical applications, although some issues need to be addressed. The optimal parameters from this study need to be validated in a larger group of volunteers, or else re-determined from more accurate simulations. While the use of an fNAV reconstruction greatly reduced reconstruction time, a shorter reconstruction time would better permit the clinicians to assess the images at the scanner. Parallelization of the fNAV reconstruction might be one means. Deep learning approaches for cardiac MR image reconstruction might be another means. Five-second reconstruction times were achieved for 4D undersampled Cartesian acquisitions with a 15-subject training set (125), indicating that the 20 LIBRE datasets acquired here might serve as an adequate training set. Yet another such approach could be SIMBA (126). The trajectory peaks in LIBRE datasets (and bSSFP datasets in general) hindered the application of SIMBA to these data, meaning that another means of extracting the motion signals might enable the use of SIMBA for LIBRE.

There are potential alternatives for free-running coronary MRA. Such alternatives must be amenable to a free-running acquisition, namely avoiding the use of external devices, and permit the extraction of cardiac and respiratory motion signals. As noted in the article in Section 2.3, it would be interesting to compare free-running LIBRE and free-running FISS as they have both been recently used for free-running 5D coronary MRA. Current work in the lab aims to use asymmetric echoes to reduce the TR constraints and enable more robust high-resolution imaging with radial FISS; changing TR with the present free-running LIBRE approach would only affect the likelihood of banding artefacts and may thus serve as a potential means of reducing scan time. Moving on, the water excitation techniques have the benefit of being readily implementable in the

free-running framework. LIBRE should be compared with the BORR pulse in a free-running radial bSSFP acquisition, as they are the two off-resonant excitation techniques of which we are aware. Although only an RF-phase-modulated 1-2-1 water excitation pulse was examined in this study, it would be very informative to examine free-running imaging with other water excitation pulses, especially as they can be used for both non-selective and slab-selective imaging. Slab-selective excitation would have the benefit or reducing signal from bright sources outside the FOV and thus reducing streaking artefacts in radial imaging. Furthermore, the spectrally-selective wideband bSSFP approach (92) highlighted the possibility of modifying the interpulse spacing, which suggests that other parameters of these conventional binomial pulses can be modified to improve on-resonant signal of the 1-2-1 pulse to that of normal bSSFP. In general, it might be informative to define an optimization problem involving a general class of (off-resonant) binomial excitation pulses, to see if other promising pulses can be found; a possible approach could use particle swarm optimization (127) as was done in (128). Second, although inversion-based fat suppression techniques can theoretically be applied for free-running Cartesian imaging, the need to image around the TI might impose impractical restrictions on the trajectory and result in scan inefficiency. A possible alternative may be combined T_1 mapping and synthetic fat suppression using an inversion-based 3D radial free-running sequence for T_1 mapping (129), where it was shown that the T_1-weighting could be incorporated as an extra dimension in the free-running framework, although it remains to be seen whether spatial resolution can be increased for high-resolution coronary imaging. Third, with regards to the sequence-based techniques, FS-TIDE (91) does not appear to be adaptable to 3D trajectories, and the required short TR and reduced SNR of the periodic RF angle technique (89) may be prohibitive for high-resolution imaging. It remains to be seen whether the opening and closing ramped flip angles of the S5FP approach (76) may generate artefacts in either the motion extraction step or the reconstructed images. The two dual-acquisition bSSFP techniques (86,88) may be worth investigating, although some sort of acceleration along the phase cycle dimension should be added to mitigate the increase in scan time. The use of steady-state bSSFP sequences makes the techniques possible with both radial and Cartesian imaging, and also the steady-state nature may facilitate extracting motion signals. Fourth, multi-echo Dixon fat-water separation techniques hold promise for B_0- and B_1-insensitive fat suppression, and current work in the lab is exploring this avenue. The feasibility of motion extraction from the imaging data, due to the use of different TEs, remains to be investigated, although non-trajectory-based motion signals may alleviate this concern. TRs with bSSFP-based Dixon techniques have been below 6 ms (99,130), which should reduce the risk of banding artefacts, but a combined Dixon and

banding reduction technique (102) may also be useful for free-running imaging. The other bSSFP-based water-fat separation techniques could also be used, as the sequence could be readily adapted. The phase-sensitive technique (104) should be easily translatable and should be less sensitive to partial volume effects at the higher resolutions necessary for coronary MRA, although it remains to be seen whether the TR-dependance would make it B_0-sensitive in the inhomogeneous volumes experienced in cardiac MRI. Finally, the repeated sampling of the k-space centre by rosette trajectories fulfills the self-gating criterion for free-running imaging, although the SNR reduction may be prohibitive. In summary, the binomial water excitation, bSSFP-based, and Dixon-based techniques hold the most promise for alternative free-running imaging approaches.

To add to the previous paragraph, it should be pointed out that some techniques might be more amenable to low-field free-running bSSFP imaging and others to high-field free-running imaging. While higher field strengths benefit from higher SNR, lower field strengths benefit from lower cost, lower SAR, improved main field homogeneity, and improved safety for patients with implants (131). At higher field strengths, the water excitation techniques would all have shorter RF pulse durations and therefore TR due to the increased separation between fat and water in the tissue-frequency domain, reducing scan time. However, the increased B_0 and B_1 inhomogeneities would need to be mitigated; a GRE acquisition with contrast agent would be one avenue with regards to B_0 inhomogeneities. On the other hand, the improved field imhomogeneity lends bSSFP sequences readily to low-field applications, where the use of bSSFP together with the other advantages of low-field systems may help to offset the SNR reduction (131). The simultaneous banding reduction and fat suppression technique with phase-cycled bSSFP (86) would be able to use a more flexible TR of 6.6 ms with little risk of banding artefacts (see Figure 5 in (131)), providing for reduced-banding high-resolution imaging. Other bSSFP techniques like fluctuating equilibrium MRI (106) and two-phase linear combination (107) would also be able to take advantage of such a longer TR. The Dixon bSSFP techniques might also benefit from the improved B_0 homogeneity at low field, as it would reduce restrictions on TR and hence TE. The increase in scan time due to TR would need to be considered, although Simonetti et al. have argued that acceleration with CS methods would have an even more beneficial effect on image quality at low-field than at high-field (131). Applying the free-running LIBRE approach at low field would necessitate increasing pulse duration to account for the reduced water-fat separation in the tissue frequency domain, assuming the other two parameters remain constant, yet the inherent benefits of low-field imaging would provide two avenues of

optimization. The improved B_0 homogeneities would permit increasing TR, accommodating increases in pulse duration and consequent reductions in RF frequency with the effect of increasing blood signal, and consequently reducing receiver bandwidth for increased SNR. On the other hand, the reduced SAR would permit a higher excitation angle, reducing pulse duration (and compensating for the inherently longer pulse durations), TR, and consequently, acquisition time.

As a final addition to the discussion about alternative free-running approaches, a free-running study using a spiral-based Cartesian trajectory (132) was performed by a colleague, Christopher Roy (133). The original study found that image quality relative to 5D radial imaging was somewhat degraded by artefacts, partly from uncompensated intra-bin motion. Although LIBRE and BORR are not adaptable to a slab-selective Cartesian approach, the binomial water excitation and bSSFP-based approaches hold promise for Cartesian free-running imaging, in combination with a technique like fNAV for accounting for intra-bin respiratory motion.

This work offers the potential to open up the field of cardiac MRI by simplifying the complicated workflow and required specialist knowledge. This combination of the free-running framework and LIBRE water excitation shifts the burden from the acquisition side to the reconstruction side. The self-gating feature of the free-running framework reduces the amount of active participation by both technicians and patients, removing the need for the set-up of the ECG and other external devices and removing the need for breath-holds, among other things. The generation of blood-fat contrast through the water excitation properties of the LIBRE pulse and that of blood-myocardium contrast inherently by the use of an uninterrupted bSSFP sequence obviated the need for the administration of gadolinium-based contrast agent, which can sometimes pose health risks (17). Moreover, the computational burden of the XD-GRASP reconstruction was itself greatly reduced through the use of fNAV reconstruction, and can perhaps be further reduced through the use of deep-learning-based reconstruction. In addition, bSSFP sequences have been widely used for both cardiac imaging and other applications for about the past twenty years, which should facilitate both the availability on different scanners, particularly low-field scanners, and clinical acceptance of uninterrupted free-running bSSFP approaches. From the technical side, this study also showed that a simple, conventional sequence like bSSFP could be successfully used for 3D cardiac MRI, potentially encouraging new research. The use of the LIBRE free-running approach therefore has the potential to improve adoption of cardiac MRI by reducing acquisition times and sequence availability (6), in addition to the reduction in invasiveness and

operator-dependance and automatic patient-specific motion detection provided by the free-running framework.

3 FREE-RUNNING MULTIPARAMETRIC 5D MYOCARDIAL MAPPING WITH PLANET

3.1 Outline

This chapter will present work on PLANET for static and dynamic applications. Consistent with the work done in Chapter 2 where RF phase properties were exploited to generate contrast between blood and fat, PLANET exploits the phase of RF excitations to simultaneously generate T_1 and T_2 contrast, which lends itself ideally for quantitative cardiac tissue mapping on the one hand and to be integrated as part of the free-running framework on the other. Therefore, the work reported here is a logical extension of that in the previous chapter. In this chapter, a literature overview of previous techniques for multiparametric T_1 and T_2 mapping will first be presented and then used to motivate the choice of PLANET in detail. This will be followed by a description of the PLANET algorithm. The subsequent two sections will focus on technical work: accomplishing PLANET with an accelerated 3D Cartesian acquisition, and preliminary work involving PLANET for the myocardium and with radial acquisitions. The chapter will conclude with a discussion and future directions.

3.2 Multiparametric mapping approaches

This section will provide a literature overview of methods providing T_1 and/or T_2 maps. Although there are other quantitative MR imaging techniques, this focus was chosen to be consistent with the clinical significance provided in Section 1.2 and for brevity.

3.2.1 Brief overview of conventional T_1 and T_2 mapping techniques

For static tissues, the standard techniques are inversion recovery spin echo (IR-SE) for T_1 mapping and multi-echo spin echo (ME-SE) for T_2 mapping (134). IR-SE T_1 mapping acquires images of the sample at different TIs, generating a voxel-wise sampling of the longitudinal magnetization recovery curve from which a non-linear fitting technique

can be used to recover the T_1 value. IR-SE requires a long TR, recommend to be four times the longest T_1 relaxation time in the sample, leading to long acquisition times even for 2D acquisitions (134). T_2 mapping using ME-SE involves using a spin echo train to acquire several images of the sample, from which a voxel-wise fit can be used to recover T_2. Imperfections in the refocusing pulses lead to stimulated echoes that can result in an overestimation of T_2 values (135). Both these techniques are model-based and require long acquisition times (134).

For cardiac applications, the standard T_1 technique is modified Look-Locker inversion recovery (MOLLI) (10,24) and the standard T_2 technique is T_2-prepared bSSFP (10,25). The Look-Locker technique (136,137) attempts to reduce the long acquisition time of IR-SE by acquiring images with repeated low-excitation-angle pulses following each inversion pulse, which results in a perturbation of the normal recovery curve and needs a non-linear fit to recover the true T_1. MOLLI uses a 2D ECG-triggered breath-held acquisition in mid-diastole where three Look-Locker experiments are performed in succession using bSSFP readouts. Each Look-Locker experiment has a different TI that offsets the sampling of the recovery curve and ensures there are sufficient sampling points on the recovery curve when the three sets of images are combined. Nonlinear voxel-wise fitting is then used to recover the true T_1. Acquisition times in the original study ranged from 15 to 18 s (24). MOLLI measurements have high precision and reproducibility, but a low accuracy due to biases that can result from heart-rate dependance and T_2 dependance (138). T_2-prepared bSSFP uses a breath-held acquisition with T_2-preparation modules followed by dummy pulses and bSSFP partial Fourier readouts. There are two different T_2-preparation modules, to facilitate respectively a short TE of 2.59 ms and a long one of 55 ms, that are alternated during the acquisition. Fitting is performed voxel-wise. The original study used a 25 s acquisition (25). T_2-prepared bSSFP requires a delay of some heartbeats to allow for magnetization recovery (19), further increasing breath-hold and acquisition time. Moreover, a slight dependancy of the measured T_2 value on the slice orientation was also observed (139). Both these techniques are single-slice techniques that might be prone to slice misalignment in the multi-slice case (140) and are unable to provide complete information on the spatial variation of disease (10) due to limited spatial coverage (namely, 2D) or partial volume effects. Both methods also use long breath-holds that would be difficult for patients to consistently manage, as pulmonary-compromised patients can only hold their breath for 9.2 s on average (31).

In addition to the clinical advantages discussed in Section 1.2, multiparametric cardiac mapping would avoid the need to register maps acquired from different acquisitions. 3D free-breathing multiparametric techniques would also avoid the problems of slice misalignment orientation dependence, and the need for breath-holds. As well, accurate multiparametric mapping allows the retrospective generation of images with synthetic MR contrast, and such a generation of clinically-useful synthetic images may aid in improving clinical acceptance of multiparametric mapping and in increasing the amount of information available to the clinician from one scan (141).

3.2.2 Multiparametric mapping techniques for static applications

Multiparametric mapping for static applications can be categorized into a few general classes of acquisitions, including magnetization-prepared techniques, transient-state techniques, phase-cycled bSSFP-based techniques, unbalanced steady-state techniques, and stimulated-echo techniques. While most methods first reconstruct images before generating maps, one of the transient-state techniques, MR-STAT, directly reconstructs parameter maps without first reconstructing MR images (142).

3.2.2.1 Magnetization-prepared techniques

This class uses acquisitions with magnetization preparation pre-pulses, such as inversion pulses or T_2-preparation modules, to generate a specific series of contrasts and extract parameters from fitting a model to the obtained images.

IR-TrueFISP (143), which was the earliest reported multiparametric mapping technique, used an acquisition consisting of repeating sequences of an inversion pulse and bSSFP readouts, with five seconds of T_1 recovery prior to the next inversion, to acquire 38 2D images along the recovery curve. T_1, T_2, and proton density were recovered for each voxel by fitting the data to an analytical model using a least-squares fit. Maps of a single slice were acquired with near-1-mm in-plane resolution at the expense of a long acquisition time of 2:08 minutes, and the method was sensitive to B_0 inhomogeneities, which were not included in the model but were minimal in the original study of the brain (143). The authors also noted a sensitivity to imperfect slice profile effects (143). A further development incorporated a golden-angle radial trajectory with view sharing to reduce the acquisition time to 6 s per slice (144). This development also added corrections for magnetization transfer and slice profile effects that increased the scan time up to 28 s per slice.

Another technique, QRAPMASTER (141), acquired T_1, T_2, B_1, and proton density maps using a spin-echo sequence where the repeating unit had a saturation pulse followed by a multi-echo spin echo train. The saturation pulse and spin echo RF pulses acted on different slices, allowing each slice to experience different delay times that enabled the calculation of the T_1 relaxation time, while the multi-echo spin echo train allowed the calculation of T_2 (141). Parameters were recovered voxel-wise by fitting the measured signal to a theoretical model and included a correction for imperfect slice profiles. Accurate and 3D maps of the brain with voxel sizes of 0.8 x 0.8 x 5 mm were acquired in 5:14 minutes with SENSE acceleration (141). The authors did note a sensitivity to partial volume effects at interfaces of white matter and cerebrospinal fluid (141), and it was unclear whether the slice profile correction and B_1 estimate prevented the T_2 over-estimation that could occur with ME-SE.

3.2.2.2 Transient-state techniques

This class utilizes acquisitions with irregular variations in acquisition parameters, and then recovers parameter maps using an appropriate reconstruction technique.

MR fingerprinting (145) used a pseudorandomized acquisition to generate unique signal evolutions over time, or "fingerprints," for each parameter combination, and then recovered parameters via voxel-wise matching of the acquired time courses to a "dictionary" of predicted signal time courses. The original study (145) varied RF excitation angle and TR pseudo-randomly while using a 2D variable-density spiral trajectory, and matched acquired time courses to simulated time courses after magnitude normalization by finding the simulated time course that maximized the dot product (a proxy for linear correlation). The dictionary generation time for 563 784 entries was 399 s. MR fingerprinting was found to produce accurate motion-insensitive 2D maps of T_1, T_2, M0, and off-resonance with an accelerated 12.3 s acquisition and dictionary matching time of 3 minutes (145). The original study used a voxel size of 2.3 x 2.3 x 5 mm, which could be reduced at the expense of acquisition time (146). Furthermore, the requirement for spatially- and temporally-incoherent artefacts meant that, in addition to pseudorandom excitation patterns, fingerprinting was limited to spiral and radial trajectories (142,145). There have been many studies extending the capabilities or addressing the limitations of MR fingerprinting. Some examples include: accelerating map generation by about 70 times using fast group matching (147), adding B_1 estimation (148), extending to simultaneous multi-slice and 3D acquisitions (148,149), and further accelerating the acquisition down to 2.6 s using a reconstruction technique

with spatial wavelet and locally low-rank regularization (146). It should also be mentioned that the original MR fingerprinting study appeared to have ignited interest in developing multiparametric mapping techniques.

A second technique, MR-STAT (142), solved the MR-physics-based nonlinear inversion problem of the temporally- and spatial-varying MRI signal, yielding the parameters directly from k-space data without first reconstructing intensity-based images like the other multiparametric mapping techniques discussed in this thesis. MR-STAT treated the problem of generating MR parameter maps as a system identification problem (150). The avoidance of the initial Fourier decoding step of conventional MRI reconstruction had the benefit of enabling transient-state acquisitions, like MR fingerprinting (142). Unlike MR fingerprinting, however, MR-STAT did not restrict the choice of RF excitation or trajectory, being applicable to any trajectory, and did not require a pre-computed dictionary (142). MR-STAT could also provide an estimate of the precision of the parameters. A 1.8 x 1.8 x 3 mm^2 image was acquired in 7.8 s and generation of T_1, T_2, proton density, off-resonance, and B_1+ maps took 12 minutes with parallelization (142). MR-STAT had similar accuracy as reference techniques and similar map quality as MR fingerprinting, although the generation of high-resolution maps (1-mm isotropic resolution) required approximately five hours of computation (151). The computation of 3D maps would, therefore, be prohibitively long.

A third study aimed to drastically reduce map reconstruction time by using artificial neural networks for parameter estimation in combination with k-space view sharing, generating 3D T_1, T_2, and proton density maps with high accuracy in less than seven minutes (152). The networks were trained on simulated data with added noise, indicating that prior in vitro or in vivo data was not required, although the authors reported that the network had to be trained separately for each proposed acquisition (152). It was also unclear how long the training phase took.

3.2.2.3 Phase-cycled bSSFP-based techniques

These techniques all utilize multiple bSSFP acquisitions with the RF phase increment per acquisition increasing linearly from 0° to 360° (or equivalently from -180° to 180°), yet they are distinguished in the way that they extract parameter maps.

The earliest technique, motion-insensitive rapid configuration relaxometry (MIRACLE) (153), extended TESS (154) to bSSFP by using an iterative approach based on

configuration theory to estimate T_1 and T_2 relaxation times. It was able to acquire $1\times1\times2mm^3$ maps of the brain in 5min30 with 12 phase cycles (153). The maps were accurate and T_2 was B_1-insensitive, although the authors reported T_1 underestimation in the brain that was likely due to frequency profile asymmetries, as the model used failed to account for the multiple-component nature of the tissue (153). MIRACLE was also sensitive to B_0 inhomogeneities for low numbers of phase cycles (155). TrueCISS (156) used a dictionary-matching approach to estimate bSSFP parameters (M0, f0, T_2/T_1) voxel-wise from an undersampled acquisition, after a compressed sensing reconstruction that exploited spatial sparsity and sparsity of the bSSFP profile in the Fourier domain of the phase-cycle dimension. Using 16 phase cycles with 8x undersampling, they acquired data with 1×1 mm^2 resolution in 10min15s (156). The maps were B_1-insensitive, and they noted that the accuracy of the coil sensitivity estimation affected the maps (156). PLANET (64) exploited the elliptical signal model of phase-cycled bSSFP (157) to recover T_1, T_2, M0 and f0 maps by fitting an ellipse to the data in each voxel using a non-iterative least-squares method (158) and estimating parameters analytically from the model. The ellipse-fitting technique constrained PLANET to require at least 6 phase cycled acquisitions (64). PLANET could acquire accurate 3D maps using 10 phase cycles with $1.5\times1.5\times4$ mm^3 resolution in 6min04 (64). Similar to MIRACLE, T_2 estimates were B_1-insensitive, although an underestimation of T_1 and T_2 due to bSSFP profile asymmetries (64) was reported. Further work provided a simple algorithm for B_0 drift correction with two additional off-resonance maps (159). The most recent approach trained an artificial neural network with phase-cycled images (1.3 mm isotropic resolution) as input and reference T_1, T_2, B_0, and B_1+ maps as outputs, thereby enabling the voxel-wise generation of these maps (155) from a phase-cycled acquisition. The network was trained voxel-wise using approximately 439 000 bSSFP profiles from a training set of three subjects, and then tested on another three subjects (155). The generated maps were accurate and robust to acceleration using parallel imaging and reducing the number of phase cycles, bringing the viable total acquisition time down to 3min24s (155). Furthermore, the maps were unaffected by bSSFP profile asymmetries, unlike the previous model-based techniques. However, the technique had a certain amount of inflexibility as the network had to be retrained for different bSSFP sequence parameters or different reference protocols, and the generalizability of the technique was unclear as only healthy subjects were included (155).

3.2.2.4 Unbalanced steady-state techniques

This class of techniques involves steady-state sequences with unbalanced gradient waveforms, with (150) or without RF spoiling (154,160,161).

Leroi et al. (150) adapted quantitative imaging using configuration states (QuICS) (162) to obtain proton density, B_1, T_1, and T_2 maps at ultra-high field strength (7T). The sequence used 11 GRE acquisitions with varying RF spoiling increments and RF excitation angles (150); the acquisition pattern was optimized using the Cramer-Rao lower bound (CRLB). A 3D Cartesian trajectory with 1 x 1 x 3 mm^3 voxel size and parallel imaging was used, leading to a total acquisition time of 16min36s (150). 3D maps were generated with voxel-wise nonlinear least-squares fitting to an analytical model. This technique had similar accuracy and precision as the reference methods they used, although the T_1 relaxation time was over-estimated (150).

The other three techniques were essentially unbalanced multi-echo SSFP sequences. Double-echo steady-state (DESS) sequences have been used for 3D T_1, T_2, and proton density mapping (160,163), and additionally for diffusion coefficient mapping (160). Both studies optimized their sequence parameters using the CRLB, leading to acquisition times of 35 minutes for 1-mm-isotropic resolution (160) and 15 minutes for 1.4-mm-isotropic resolution (163), which did not include an extra 2-4 minutes for B_1 map acquisition for correction (160,163). Voxel-wise least-squares fitting was used for both cases, although Stöcker et al. (163) also used a pre-computed signal database to reduce computation times. The two studies reported high accuracy and precision, except at higher T_2 values, that were unaffected by off-resonance, at the cost of a sensitivity to B_1 inhomogeneities and an underestimation of T_2 in brain tissues due to the lack of a two-component model (160,163). Triple-echo steady-state (TESS) sequences have been used for T_1 and T_2 mapping (154) in the knee, using iterative voxel-wise fitting informed by configuration theory. 3D maps were acquired with 0.6 x 0.6 x 3 mm^3 resolution in 4min24s (154). TESS enabled accurate, B_0-insensitive, and B_1-insensitive T_2 estimation, although T_1 estimation was affected by B_1 inhomogeneities (154). As well, seven averages were required, indicating that TESS suffers from low SNR. The multipathway multi-echo (MPME) technique extended TESS to multiple echoes (161) to analytically generate T_1, T_2, T_2^*, B_1+, B_0, and proton density maps with 1.2 x 1 x 1.2 mm^3 resolution in under 14 minutes. The main drawback of MPME was reduced precision due to uncontrolled noise amplification in the map generation pipeline (161), although the authors noted that it was amenable to regularized or deep-learning reconstructions

to alleviate this problem. All these unbalanced techniques were sensitive to uncorrected motion (154,160,161,163).

3.2.2.5 Stimulated-echo-based mapping

Stimulated-echo-based mapping (STEM) used a stimulated-echo diffusion-weighted sequence, varying mixing time, TE, and b-values to generate four images from which T_1, T_2, proton density, and the apparent diffusion coefficient were calculated voxel-wise by nonlinear least-squares fitting (164). STEM provided accurate maps of the brain in 13min20s that were insensitive to B_1-inhomogeneities and amenable to a six-fold acceleration in a restrospective study, although at the cost of B_0-sensitivity and an inability to model multi-component tissues with the current model (164). Moreover, that study used a resolution of 2.2 x 2.2 x 5 mm^3 and a TR of 4 s, respectively indicating a potential low SNR and poor applicability to the imaging-based motion extraction of the free-running framework.

3.2.3 Multiparametric mapping techniques for cardiac applications

3.2.3.1 Magnetization-preparation-based techniques

As before, this class uses acquisitions with specific magnetization preparation pre-pulses, such as inversion pulses or T_2-preparation modules, to generate a specific series of contrasts and extract parameters from fitting a model to the obtained images.

The following techniques used interleaved inversion and T_2prep pulses. The first simultaneous T_1 and T_2 myocardial mapping study was that by Blume et al. (165), which used an ECG-triggered navigator-gated 2D sequence where R-R intervals could contain either an inversion pulse or T_2prep module followed by a bSSFP readout or else no excitation (rest heartbeat). T_1-weighting was accomplished through the use of different TIs and T_2-weighting through the use of different TEs for the T_2prep module, with the relaxation times being calculated from a voxel-wise fit of the respective data. The acquisition time was approximately three minutes with a resolution of 1.3 x 1.3 x 8 mm^3 (165). The acquired values matched those of conventional reference techniques, although the technique could not quantify long T_1 values, as the TI was constrained by the R-R interval (165). There was a potential for inter-dependance of the T_1 and T_2 estimates and a slight heart rate dependance (165). Further work by Shao et al. (166) incorporated a golden-angle radial breath-held acquisition with GRE readouts and compressed sensing reconstruction to reduce the acquisition duration to 11 heartbeats and remove the heart rate dependence, and then reduced the map generation time to

under one second using deep learning (167). Another technique, 3D-QuAntification using an interleaved Look-Locker Acquisition Sequence with T_2 preparation pulse (3D-QALAS) (168), used an ECG-triggered breath-held 3D GRE sequence with SENSE acceleration (45) and voxel-wise least-squares fitting. Maps were acquired with 2 x 2 x 12 mm^3 in 15 heartbeats, and were shown to match reference techniques with an insensitivity to heart rate variations and B_1 inhomogeneities (168). A recent study by Qi et al. (169) combined a GRE readout, cardiac ECG-gating, respiratory self-navigation, low-rank patch-based reconstruction (170), and dictionary matching for 3D free-running T_1 and T_2 mapping and cine imaging. Acquisitions took 11.2 minutes with an isotropic spatial resolution of 2 mm, resulting in maps with similar accuracy but improved precision compared to reference techniques and no effect of heart rate (169).

Cardiac balanced-SSFP inversion recovery with interleaved sampling acquisition (CABIRIA) (171) translated the previously-discussed IR-TrueFISP (143) technique to cardiac imaging at 3T, using only an inversion pulse to generate contrast. 2D ECG-triggered breath-held maps were acquired in 8 heartbeats with 1.7 x 1.7 x 8 mm^3 resolution (171). CABIRIA generated maps with similar accuracy and precision as reference values and incorporated slice profile correction, although the authors indicated that artefacts could arise from B_0 inhomogeneities or through-plane motion (171).

A final subcategory uses acquisitions incorporating saturation pulses for T_1-weighting and T2prep modules for T_2-weighting. Akcakaya et al. (172) used a 2D ECG-triggered breath-held bSSFP acquisition to acquire maps in 13 heartbeats with a voxel size of 2 x 2 x 8 mm^3. Saturation time and TE of the T2prep module were varied among the heartbeats, and maps were generated via voxel-wise least-squares fitting. This technique provided similar accuracy as reference techniques, albeit with a reduced precision for T_2, and was insensitive to heart rate (172). Guo et al. (173) used a 3D ECG-triggered navigator-gated GRE acquisition with a scheme of interleaved pulses and rest heartbeats and map generation using voxel-wise model-based fitting. Maps were acquired in approximately eight minutes with a resolution of 1.5 x 1.5 x 16 mm^3 (173). The maps were accurate, although the T_1 values had a slight dependance on heart rate (173).

3D-QALAS was applied in 23 patients, demonstrating similar values as reference techniques and with high precision, although maps could not be acquired in one patient (174).

Therefore, the techniques in this category generate myocardial maps with relatively low spatial resolution, usually with large slice thicknesses of 8 mm and in-plane resolution of 2 x 2 mm^2, indicating either a need to improve SNR or else, given that most studies were breath-held, reduce acquisition time. Cardiac motion was compensated for using ECG triggering, and respiratory motion was compensated for using breath-holds, with only two of the studies using free-breathing techniques. Most of the studies had 2D acquisitions. Sensitivity to heart rate and inter-dependance of the T_1 and T_2 estimates were two concerns that methods in this class often sought to address.

3.2.3.2 Cardiac MR fingerprinting

This recent class of techniques adapts MR fingerprinting (145) to cardiac MRI.

The first such study was performed by Hamilton et al. (175), who used a 2D ECG-triggered breath-held GRE acquisition, which incorporated inversion and T2prep pulses, at 3T together with an iterative approach for reconstruction and map generation that incorporated the ECG signal to account for heart rate variation. Data were acquired in 16 heartbeats with an acquisition window of approximately 240 ms and 1.6 x 1.6 x 8 mm^3 voxel size, and maps were generated in approximately 8 minutes (175). The authors reported high T_1 value accuracy and a small bias of -2.6 ms in T_2, and an insensitivity to B_1+ inhomogeneities (175). However, they noted that the acquisition might be impractical for patients with high heart rates or who cannot hold their breath for the required time, but noted that it could be reduced at the cost of a longer reconstruction time (175). In a larger population of healthy volunteers, cardiac MR fingerprinting was noted to have better map quality and similar repeatability but lower precision compared to MOLLI and T_2-prepared bSSFP (176). This single-slice version was further developed into three-slice coverage with the same acquisition time, using a low-rank reconstruction with spatial wavelet regularization to maintain precision despite the acceleration (177). However, the authors noted that the relaxation times did not match those of reference techniques, and map generation took almost one hour (177). The single-slice version was also extended to a 2D free-running cardiac-motion-resolved bSSFP sequence that could additionally generate cine images using ECG gating (178,179). One version used a variable-density spiral trajectory with a 10.9-s breath-hold and 1.6 x 1.6 x 8 mm^3 resolution, and registered all cardiac phases together prior to map generation (178), while another used a tiny golden-angle radial trajectory with a 29.4-s breath-hold and 2 x 2 x 10 mm^3 resolution (179); both used a form of low-rank reconstruction. Interestingly, the 29.4-s technique was the only one of the techniques

in this paragraph to not add T_2prep modules with varying TEs as a way of further distinguishing between time courses (179). Both studies reported significant differences in T_2 values compared to reference techniques (178,179), which both studies suggested was partly due to uncompensated in-plane and through-plane motion, whereas only the 10.9-s study reported significant differences in T_1 values (178). The precision of the free-running technique appeared similar to the reference methods, although neither study specifically commented on this aspect. Both studies also had long reconstruction times of six (178) and three hours (179), respectively. Finally, Cruz et al. (180) successfully performed 3D cardiac MR fingerprinting using a variable-density stack-of-spirals trajectory, GRE readouts, ECG triggering, respiratory correction with an autofocus algorithm (121) using the signal from a respiratory bellows, and low-rank reconstruction combined with HD-PROST denoising (170). Data were acquired in approximately seven minutes with 2 x 2 x 8 mm^3 resolution, and dictionary generation and map reconstruction took ten hours (180). While precision was similar to reference techniques, mean relaxation times had biases compared to reference methods, similar to the other MR fingerprinting techniques in this paragraph (180).

A sub-category combines cardiac MR fingerprinting with water-fat separation techniques. The first such study was by Jaubert et al. (181), who incorporated a three-echo GRE readout and golden-angle radial trajectory into 2D ECG-triggered breath-held cardiac MR fingerprinting. HD-PROST (170) was used to reconstruct images, from which water and fat images and a B_0 map were generated using multi-echo Dixon techniques, and then maps were extracted for both water and fat using dictionary matching. Data were acquired in 15 s with a voxel size of 2 x 2 x 8 mm^3, and reconstruction and map generation took approximately three hours (181). The water T_1 and T_2 maps had biases compared to reference techniques, although spatial variability was similar (181). This was extended to 3D ECG-triggered respiratory-corrected cardiac MR fingerprinting using a dual-echo GRE readout, variable-density 3D Cartesian trajectory, and image-based navigators (66). Data were acquired in approximately nine minutes with 2-mm isotropic resolution. T_2 values matched those of T_2-prepared bSSFP, although T_1 values were higher than with MOLLI, and precision was lower (66). A separate 2D ECG-triggered breath-held study used rosette trajectories instead for water-fat separation (see Section 2.2.2.5) , generating water and fat maps, and a B_0 map, with 1.6 x 1.6 x 8 mm^3 voxel size and an acquisition time of 15 heartbeats (117). Relaxation times had biases relative to reference techniques (117), similar to the other cardiac MR fingerprinting studies.

The single-slice water-fat MR fingerprinting technique by Jaubert et al. (181) was applied in 19 patients in a separate study (182), which showed it had better image quality and similar precision but biases compared to reference mapping techniques.

In general, while these cardiac MR fingerprinting approaches can provide a large amount of data and are amenable to water-fat separation, fat quantification having potential use for monitoring the progression of CAD (183), it can be seen that extending their capabilities to free-running or 3D coverage results in a dramatic increase in reconstruction time of up to ten hours. The temporal incoherence of the trajectories also necessitates the use of external devices for respiratory and cardiac motion tracking, which in the case of the ECG signal would require setting-up and be subject to errors leading to missed triggers. The studies noted disagreements with reference techniques, although, for example, this was sometimes due to the known underestimation of T_1 values by MOLLI (138). Several other explanations were offered for these biases, including uncompensated motion and MR-physics-based sources, although it remains to be seen to what extent suitable corrections can be incorporated while reducing reconstruction time. Large slice thicknesses of 8 mm were generally used, which was justified as mitigating the effects of through-plane motion (178–180), and in-plane resolutions ranged from 1.5 to 2 mm isotropic. Given that the original MR fingerprinting technique used similar in-plane resolution to reduce scan time and the fact that the cardiac versions were often breath-held, such a low resolution was likely necessary to reduce acquisition times.

3.2.3.3 Cardiac MR multitasking

Cardiac MR multitasking is a recent technique that modeled the dynamic dimensions of the acquired data as a low-rank tensor, including both motion and contrast, and exploits correlations along all dynamic dimensions to reconstruct multidimensional images from under-sampled data (184). Multitasking was applied in a proof-of-concept study for cardiac-and-respiratory-motion-resolved 2D T_1 and T_2 myocardial mapping (184), using hybrid pulses capable of generating both T_1 and T_2 weighting and deriving physiological motion signals from a golden-angle radial trajectory. Data were acquired in both healthy subjects and patients in 88 s with 1.7 x 1.7 x 8 mm^3 resolution, and reconstruction took approximately 71 minutes per dataset (184). The relaxation times had biases relative to reference methods, although the authors noted that the values were within the range of reported values and that such deviations had been previously reported, and similar precision (184). While multitasking has been extended to 3D brain

(185) and 2D motion-resolved myocardial T_1 mapping (186), no extension to 3D myocardial T_1 and T_2 mapping has been reported.

3.3 Motivation

The current cardiac multiparametric approaches suffer from 1) low spatial resolution, as they generally use large voxel sizes of approximately 1.5 to 2-mm in-plane and 8-mm slice thickness, often with 2) low spatial coverage coverage and 3) often without cardiac-and-respiratory motion resolution. All the techniques with the exception of multi-tasking 4) used the ECG for cardiac motion tracking, and 5) breath-holding was often used for respiratory motion compensation. The magnetization preparation-based techniques appeared to suffer from 6) confounding effects, such as heart rate and inter-dependance of T_1 and T_2 values. Cardiac MR fingerprinting can offer a vast amount of information, although motion-tracking requires 7) external devices that might themselves require set-up and its extension to more than two spatial dimensions comes at a 8) large increase in reconstruction time. Cardiac multitasking is a promising technique that can resolve different types of dynamic information about the heart, although 9) its applicability to 3D techniques remains to be investigated as 2D maps already required more than an hour to reconstruct. Therefore, because of reasons 2, 4 and 5 above, the current published cardiac multiparametric approaches do not appear to be compatible with free-running imaging, which would offer improvements in the amount of information available and ease-of-use.

Concerning the feasibility of applying static multiparametric approaches to the free-running framework, the RF-pulse-based and transient-state categories would be subject to similar considerations as those for cardiac RF-pulse-based and fingerprinting (reasons 1 to 7 above). The unbalanced steady-state techniques can provide many different tissue parameters, but their sensitivity to intra-bin motion hinders their amenability to physiological motion resolution (reason 3). The stimulated-echo technique has the advantages of mapping many parameters and being B_1-insensitive, although it has lower spatial resolution, due to reduced signal, compared to the other techniques.

The phase-cycled techniques use uninterrupted bSSFP sequences, which can be used with 3D acquisitions and, as was shown in Chapter 2, are readily amenable to the free-running framework, avoiding problems 2, 3, 4, 5, 7, and 9. The techniques themselves

also do not suffer from problem 6. However, there is an inherent increase in scan time due to the need for multiple acquisitions.

In light of these considerations, it was hypothesized that phase-cycled uninterrupted bSSFP acquisitions and PLANET could be applied to the free-running framework for uninterrupted free-running 5D T_1 and T_2 myocardial mapping. PLANET was chosen as it could account for off-resonance, which can be considerable in cardiac applications, while estimating T_1 and T_2 relaxation times with higher resolution than the other mentioned techniques (reason 1). In fact, this was the inspiration I had after reading the original PLANET paper (64) around the spring of 2018 and having seen from my own work in the free-running LIBRE project and other work in the lab (187) that uninterrupted bSSFP acquisitions could be readily used for free-running imaging. To counter the inherent increase in scan time, acceleration of the acquisition would be required. The use of regularization in the free-running LIBRE study and the use of Fourier-transform regularization along the phase cycle dimension in the MIRACLE study (153), indicated that the long acquisition time of a phase-cycled 3D, or 5D, acquisition could be further accelerated.

3.4   Personal contribution

I reached out to Yulia Shcherbakova and received PLANET code from her, and went through the derivation for the PLANET algorithm to ensure I understood the algorithm and the code I had received. I built on the numerical simulation code from Chapter 2 by ensuring that RF phase cycling was correctly implemented and performed simulations. I performed acquisitions, reconstructions, and analyses, although I note in the text where others contributed either ideas or code. Specifically, I implemented phase cycling in pulse sequence code from Davide Piccini in IDEA (Siemens Healthcare, Erlangen, Germany) and ported it to new scanner baseline versions when necessary. Dr. van Heeswijk was at the scanner with me for the acquisitions of the data shown in Sections 3.6 and 3.7 and otherwise provided help and guidance. I modified the 5D radial reconstruction code of Jérôme Yerly to accept undersampled 4D arrays of Cartesian data, both for his version using conjugate gradient descent and the later one using the alternating direction method of multipliers (ADMM) (188). I also implemented relevant code for examining and analysing the PLANET maps. The tissue masks (Section 3.6.2.6) were kindly provided by Eleonora Fornari.

3.5 Description of PLANET algorithm

This section will describe the main steps of the PLANET algorithm, along with some details of the mathematical derivations that were not discussed in the published articles. The main steps of the algorithm are those described in the first PLANET article (64). The algorithm is very quick, taking approximately 3×10^{-4} s per voxel including the off-resonance calculation.

The correction for B_0 drift described in (159), the third PLANET article, is applied as a correction to the phase-cycled images and voxel-wise RF phase increments prior to Step 1.

3.5.1 Steady-state signal model

When the complex signal immediately after RF excitation from a (stationary) voxel due to varying RF phase increments is plotted in the complex plane, the points form an ellipse (157) centred on the real axis (see Figure 5A), described by Equation (1):

$$I = M \frac{1 - a\, e^{i\theta}}{1 - b\cos\theta} \tag{1}$$

$$M = \frac{M_0(1 - E_1)\sin\alpha}{1 - E_1\cos\alpha - E_2^2(E_1 - \cos\alpha)} \tag{2}$$

$$a = E_2 \tag{3}$$

$$b = \frac{E_2(1 - E_1)(1 + \cos\alpha)}{1 - E_1\cos\alpha - E_2^2(E_1 - \cos\alpha)} \tag{4}$$

$$E_1 = e^{-\frac{TR}{T_1}} \tag{5}$$

$$E_2 = e^{-\frac{TR}{T_2}} \tag{6}$$

$$\theta = \theta_0 - \Delta\theta_{RF} \tag{7}$$

$$\theta_0 = 2\pi(\delta_{CS} + \Delta f_0)TR \tag{8}$$

where I is the complex signal, M_0 is the thermal equilibrium magnetization, α is the RF excitation angle (rad), δ_{CS} is the chemical shift (Hz) with respect to the Larmor frequency, Δf_0 is the off-resonance due to B_0 inhomogeneities (Hz) with respect to the Larmor frequency, and $\Delta\theta_{RF}$ is the RF phase increment (rad).
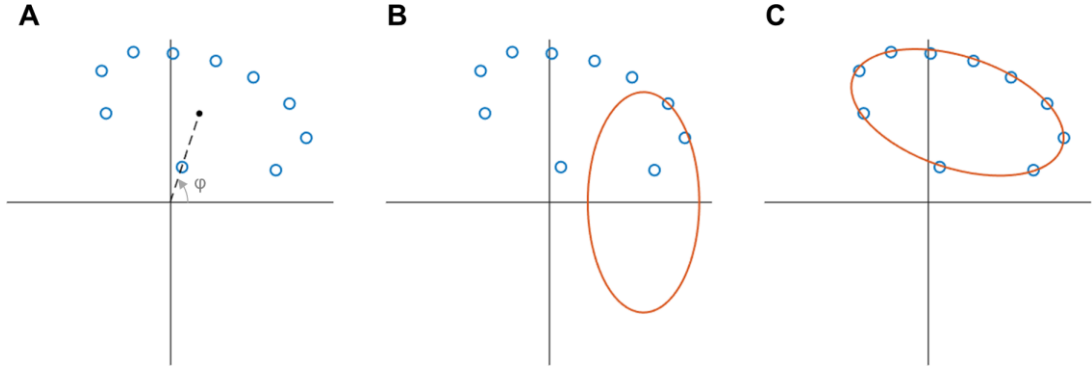
Figure 5. Graphical schematic of PLANET algorithm. A) The ellipse is fitted to the data points (step 1) in the complex plane, and the angle of rotation, φ, is estimated from its coefficients (step 2). M_{eff}, T_1, and T_2 are then estimated (step 3), and the ellipse (in red) in its canonical vertical form can then be drawn (B), which corresponds to the signal immediately after RF excitation. After Δf_0 is estimated (step 4), the fitted ellipse at time TE correctly matches the acquired data (C). Here the data points were generated with numerical simulations and with added Gaussian noise; practically, the data points would correspond to the phase-cycled bSSFP signal of a single voxel in stationary tissue.

The signal at time TE, accounting for rigid rotation about the origin due to off-resonance, is

$$I = M_{eff} \frac{1 - a\,e^{i\theta}}{1 - b\cos\theta} e^{i\varphi} \tag{9}$$

$$M_{eff} = KMe^{-\frac{TE}{T_2}} \tag{10}$$

$$\varphi = 2\pi(\delta_{CS} + \Delta f_0)TE + \varphi_{RF} + \varphi_{eddy} + \varphi_{drift} \tag{11}$$

where M_{eff} is the effective magnetization, K is the magnitude of the combined receive field (also referred to as coil sensitivities in this thesis), φ_{RF} is the RF phase offset or transceiver phase, φ_{eddy} refers to phase error due to eddy currents, and φ_{drift} is the phase error due to B_0 drift (whose correction is described in (159). The effect of φ is a rigid rotation of the ellipse counterclockwise about the origin, which can also be shown using rotation matrices.

3.5.2   Step 1: ellipse fitting

The first step involves fitting an ellipse to the data points, whose general equation is described below (Eq. (12)). This was done using a non-iterative least-squares technique based on a simple eigen decomposition that guarantees that the retrieved conic is elliptical (158,189), and it is the algorithm used in this thesis. The use of a singular value

decomposition also ensures the algorithm will not return an error. The fact that Equation (12) has six coefficients is the reason why PLANET requires at least six RF phase increments:

$$C_1 x^2 + C_2 xy + C_3 y^2 + C_4 x + C_5 y + C_6 = 0 \tag{12}$$

One alternative ellipse fitting algorithm is a constrained approach that requires only four points (190).

3.5.3 Step 2: rotation of ellipse back to real axis

In this step, the ellipse is rotated back to the real axis, undoing the effect of φ. This is done by calculating φ and the coefficients of the rotated ellipse (the one rotated back to the x-axis).

The conic equation for an ellipse centred at the origin is:

$$\frac{x^2}{A^2} + \frac{y^2}{B^2} - 1 = 0 \tag{13}$$

Translating this ellipse to (x_c, y_c) and then rotating it counterclockwise by φ, where the rotation matrix, R_φ, is

$$R_\varphi = \begin{bmatrix} \cos\varphi & -\sin\varphi \\ \sin\varphi & \cos\varphi \end{bmatrix}, \tag{14}$$

we get:

$$\left(\frac{\cos^2\varphi}{A^2} + \frac{\sin^2\varphi}{B^2}\right)x^2 + \left(\frac{\sin 2\varphi}{A^2} - \frac{\sin 2\varphi}{B^2}\right)xy + \left(\frac{\sin^2\varphi}{A^2} + \frac{\cos^2\varphi}{B^2}\right)y^2$$
$$+ \left(\frac{-2x_c \cos\varphi}{A^2} + \frac{2y_c \sin\varphi}{B^2}\right)x \tag{15}$$
$$+ \left(\frac{-2x_c \sin\varphi}{A^2} - \frac{2y_c \cos\varphi}{B^2}\right)y + \left(\frac{x_c^2}{A^2} + \frac{y_c^2}{B^2} - 1\right) = 0$$

Equating like terms in Equations (12) and (15) and manipulating the terms, we find that

$$\varphi = \frac{1}{2}\tan^{-1}\frac{C_2}{C_1 - C_3} \tag{16}$$

where C_1, C_2, and C_3 are the coefficients of the unrotated ellipse.

It can then be shown, using R_φ and Equation (12), that the coefficients of the rotated ellipse can be related to the unrotated ellipse as follows:

$$C_1' = C_1 \cos^2 \varphi + \tfrac{1}{2}C_2 \sin 2\varphi + C_3 \sin^2 \varphi \qquad (17)$$

$$C_2' = (C_3 - C_1) \sin 2\varphi + C_2 \cos 2\varphi, \qquad (18)$$

$$C_3' = C_1 \sin^2 \varphi - \tfrac{1}{2}C_2 \sin 2\varphi + C_3 \cos^2 \varphi \qquad (19)$$

$$C_4' = C_4 \cos \varphi + C_5 \sin \varphi \qquad (20)$$

$$C_5' = -C_4 \sin \varphi + C_5 \cos \varphi \qquad (21)$$

$$C_6' = C_6 \qquad (22)$$

Comparing the rotated coefficients in Equations (17) to (22) to like terms in (15) with φ set to zero, we can calculate the geometric parameters of the rotated ellipse. At this point, φ is unwrapped from its range of $(-\tfrac{\pi}{4}, \tfrac{\pi}{4})$, due to the $\tan^{-1}()$ function, to $(-\pi, \pi)$ by examining its geometric parameters to ensure it is vertical and centred on the x-axis, per Equation (1); the rotated coefficients and geometric parameters are re-calculated if necessary.

As an aside, although the ellipse for the signal from a single-component tissue after RF excitation will lie on the real axis, it was tentatively shown that y_c, the residual vertical displacement of the rotated ellipse, may be correlated to the fraction of multiple-component tissues such as fat (191). Therefore, it can be used a measure of the "validity" of the PLANET estimates that assume single-component tissue.

3.5.4   Step 3: calculation of M_{eff}, T_1, and T_2

Using the geometric parameters, M_{eff}, a, and b in Equation (1) can be determined using the following formulas in the Appendix of (64):

$$b = \begin{cases} \dfrac{-x_c A + \sqrt{(x_c A)^2 - (x_c^2 + B^2)(A^2 - B^2)}}{(x_c^2 + B^2)}, & \alpha > \cos^{-1}\left(e^{\frac{-TR}{T_1}}\right) \\[3mm] \dfrac{x_c A + \sqrt{(x_c A)^2 - (x_c^2 + B^2)(A^2 - B^2)}}{(x_c^2 + B^2)}, & \alpha < \cos^{-1}\left(e^{\frac{-TR}{T_1}}\right) \end{cases} \qquad (23)$$

$$a = \frac{B}{x_c \sqrt{1 - b^2} + bB} \qquad (24)$$

The RF excitation angles that are practically used will fall under the case $\alpha > \cos^{-1}\left(e^{\frac{-TR}{T_1}}\right)$, as accuracy and precision would otherwise be low at normal TR values (see, for example, Figure 2 in (192)).

M_{eff}, T_1, and T_2 can be determined using:

$$M_{eff} = \frac{x_c(1 - b^2)}{1 - ab} \tag{25}$$

$$T_1 = \frac{-TR}{\ln \dfrac{a(1 + \cos\alpha - ab\cos\alpha) - b}{a(1 + \cos\alpha - ab) - b\cos\alpha}} \tag{26}$$

$$T_2 = -\frac{TR}{\ln a} \tag{27}$$

3.5.5   Step 4: calculation of off-resonance

The off-resonance, Δf_0, is calculated after the main three steps per the procedure in (64), although it requires only φ from Section 3.5.3. A by-product of this step is the RF phase offset, φ_{RF}, which can be used for in vivo conductivity mapping (193).

The fact that the off-resonance calculation is independant of the other three parameters estimated by PLANET means that it can be substituted with another algorithm, such as the one in (194).

3.6   Accelerated 3D Cartesian PLANET for static applications

3.6.1   Purpose

The purpose of this section was to show that the PLANET acquisition for static tissue could be accelerated while maintaining accuracy and precision. Such a study could also inform considerations for the acquisition or reconstruction of the heavily-undersampled 5D motion-resolved maps of the myocardium.

3.6.2   Methods

3.6.2.1 Undersampled 3D spiral Cartesian trajectory

The 3D Cartesian trajectory used here (132,195) has a spiral phyllotaxis pattern (Figure 6). The profiles in the phase-encoding plane fall on Cartesian positions following a spiral

pattern, with successive spirals, referred to as shots, being rotated by the golden angle ($\pi(3 - \sqrt{5})$ rad ≈ 137.5°). The number of profiles in each spiral is referred to as the number of segments. Such a sampling pattern ensures the incoherently-distributed spatial artefacts necessary for compressed sensing reconstructions. Furthermore, the trajectory also maximizes the fully-sampled area around the centre of k-space by randomly moving a profile to a nearby empty position in its 8-neighbourhood when possible; this property is useful for the calculation of coil sensitivity maps (195).
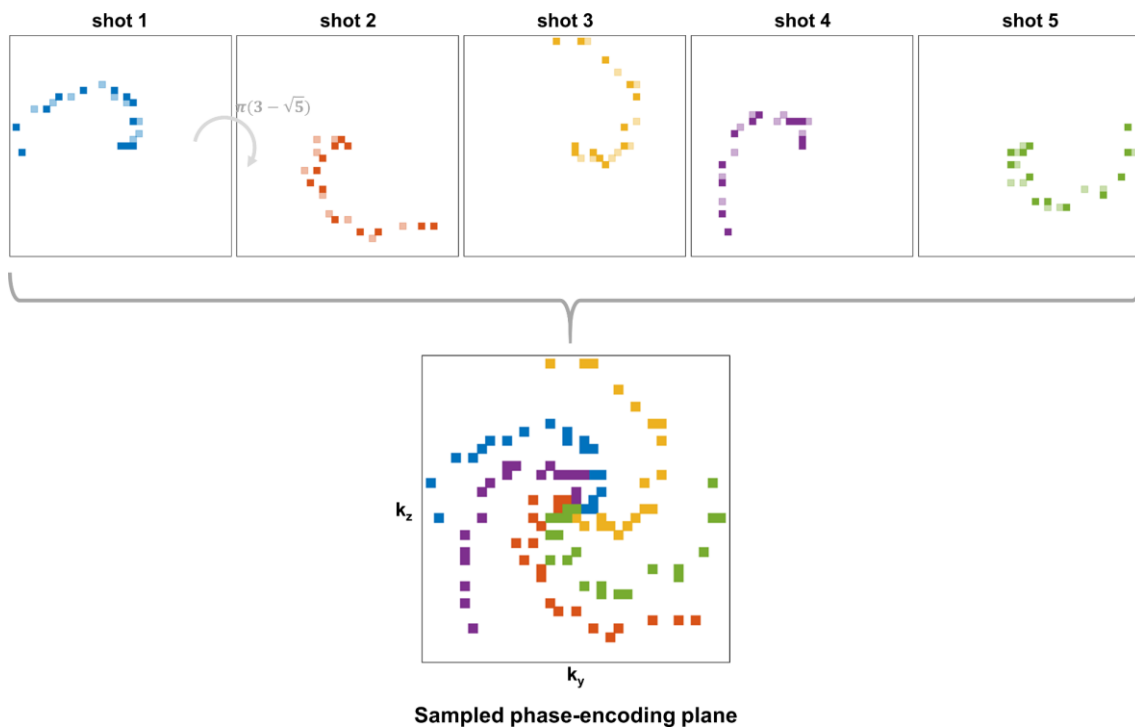
Figure 6. Sample spiral Cartesian trajectory in phase-encoding plane. Each spiral is populated first starting from the centre of k-space and going out (darker squares), then coming back towards the centre of k-space (lighter squares). Subsequent spirals (different colours) are formed by rotation by the golden angle.

This trajectory was already available in the lab, and its parameters were optimized for undersampling while maintaining a fully-sampled 24 × 24 central k-space region for adequate coil sensitivity estimation. Variable parameters included the variable density correction, spiral curvature, number of shots, and number of segments. Trajectory simulations showed that it was not possible to consistently generate a fully-sampled 24 × 24 central region with acceleration factors higher than 2, and therefore an acceleration factor of 2 was used in this study. As well, with high numbers of shots, k-space positions are inevitably redundantly sampled, meaning that the undersampling factor will be higher than the acceleration factor. For this study, a trajectory with an acceleration

factor of 2 and undersampling factor of 2.7 was generated with the following parameters: variable density correction = 0.7; spiral curvature factor = 16; 470 shots; 22 segments. A separate mask was generated for each phase cycle, with the first shot of each successive phase cycle being offset by the golden angle from the last shot of the previous phase cycle in order to generate incoherent undersampling artefacts in the phase cycle dimension.

3.6.2.2 Compressed sensing reconstruction framework

The reconstruction framework used here was an adapted version of the 5D radial reconstruction framework of Jérôme Yerly (54), of which an earlier version was used for the reconstructions in Chapter 2, modified to reconstruct Cartesian images. The framework accepts an array containing the raw data from all the phase cycles, and outputs zero-filled and CS-denoised 4D images. Fully-sampled images in the context of this chapter refers to the zero-filled images reconstructed from fully-sampled data. The 4D complex raw data (x, y, z, coil) from different phase cycles were combined into a single 5D complex array (x, y, z, phase cycle, coil). The coil sensitivities were estimated from the 24 × 24 central k-space region of the first ($\Delta\theta_{RF} = -180°$) volume using the adaptive reconstruction technique (196). The CS denoising was performed using ADMM (188) and can flexibly accommodate different regularization schemes. The reconstructions were performed in MATLAB R2018b (The MathWorks, Natick, MA, USA).

3.6.2.3 Retrospectively-undersampled reconstruction of phantom acquisition

Fully-sampled 3D Cartesian k-space data of a vial phantom with relaxation times resembling those of brain tissue were acquired at 3T (MAGNETOM Prisma, Siemens Healthcare, Erlangen, Germany) with a 64-channel head coil and retrospectively undersampled in the k_x-k_y plane by applying the mask of a 3D spiral Cartesian trajectory (see Section 3.6.2.1). The vial phantom was placed in a container filled with gadolinium-doped water. The Cartesian mask was applied to the k_x-k_y plane, as the resolution in the k_y-k_z plane was not isotropic, and as such undersampling would mimic the orientation of a 5D acquisition, namely having the fully-sampled central readout oriented in the SI direction. Relevant acquisition parameters for the fully-sampled dataset were similar to the published PLANET protocol (64) and were as follows: TE/TR = 4.98/9.96 ms; FOV = 220 x 220 x 100 mm³; matrix size = 144 x 144 x 40 including 25% slice oversampling; voxel size = 1.5 x 1.5 x 2.5 mm³; RF excitation angle = 30°; receiver bandwidth = 131 Hz/pixel; 144 dummy excitations; N = 10 RF phase-cycling schemes

starting from -180° in increments of 36°; total acquisition time = 9min40s; lowest gradient slew rate setting. An ME-SE acquisition for reference T_2 maps was also run with the following parameters: TR = 5000.0 ms; 32 TEs from 10 to 320 ms in increments of 10 ms; FOV = 250 x 250 x 8 mm^3; voxel size = 1.0 x 1.0 x 8.0 mm^3.

We examined the effect of three different regularization schemes on the accuracy and precision of the PLANET maps generated from the undersampled reconstructions. We investigated spatial wavelet regularization and Fourier transform regularization applied along the phase cycle dimension (FT-PC), both without and with spatial total variation (TVs) regularization. The examined array of regularization weights was [0, 0.001, 0.005, 0.01] for both wavelet and FT-PC regularization and [0, 0.001] for TVs. The range of weights for TVs was based on preliminary experiments that showed that higher weights led to over-smoothing of the PLANET maps and introduced spurious spatial variations that were not present in the fully-sampled maps. The use of FT-PC was inspired by its use for the trueCISS technique (156), where it was noted that the complex signal of phase-cycled bSSFP is sparse in the Fourier domain of the phase-cycle dimension (197) and, therefore, such a regularization can be thought of as a physics-inspired one for phase-cycled bSSFP datasets. In addition, we also examined if there was a synergistic effect of the regularization schemes by running a reconstruction with both FT-PC and wavelet regularization using the weights that yielded the highest qualitative map quality.

3.6.2.4 Retrospectively-undersampled reconstruction of human brain acquisition

We examined the effect of undersampling on an in vivo acquisition of a human brain at 3T (MAGNETOM Vida, Siemens Healthcare, Erlangen, Germany) with a with a 64-channel head coil using the same trajectory as above and the regularization weights that yielded optimal qualitative image quality in vitro. Relevant acquisition parameters for the fully-sampled dataset were similar to the published PLANET protocol (145) and differed from those in Section 3.6.2.3 in the case of FOV (220 x 220 x 160 mm^3) and voxel size (1.5 x 1.5 x 4 mm^3).

3.6.2.5 Image pre-processing and PLANET map generation

PLANET was implemented in MATLAB 2019b (The MathWorks, Natick, MA, USA) and run as described in Section 3.5. A mask was input to avoid running PLANET on voxels whose mean magnitude in the phase-cycle dimension was less than 3% of the maximum mean magnitude in the phase-cycle dimension; such a mask was included in the code

from Yulia Shcherbakova and it was empirically found that it excluded background (air or irrelevant) voxels from the PLANET algorithm.

For the fully-sampled phantom images, preprocessing prior to running the PLANET algorithm included an unringing algorithm that removes Gibbs ringing artefacts in Cartesian images through local subvoxel shifts to minimize oscillations (198), as this was used in the published PLANET algorithm. It was indeed also observed that excluding this step resulted in clear Gibbs ringing artefacts in the PLANET maps. This preprocessing step was not used for the undersampled data to avoid confounding its effect with that of TVs regularization.

For the brain data, the unringing algorithm was run only on the fully-sampled data for the same reason as above. Rigid co-registration of the individual phase-cycled volumes to the first phase-cycled volume was applied to both the sets of images, after the unringing algorithm in the case of the fully-sampled data.

3.6.2.6 Data analysis

For the in vitro phantom images, the accuracy and precision of T_2 maps of the undersampled reconstructions was compared to that of the fully-sampled non-denoised reconstruction. Accuracy was assessed as the correlation of mean values of the vials in the PLANET maps to reference ME-SE maps. Precision was evaluated as the coefficient of variation of the respective vials, which is equal to the standard deviation of the data in an ROI drawn in each vial divided by its mean. Only PLANET T_2 data were assessed as no B_1 maps were acquired for correction of PLANET T_1 values.

For the in vivo brain images, an ROI analysis of white and grey matter was performed. White matter (WM), grey matter (GM), and cerebrospinal fluid were segmented using the unified segmentation approach (199) on the M_{eff} maps, and voxels were classified according to the tissue with the highest probability. ROIs were drawn in the same five central slices in the GM and WM masks, ensuring that they were distributed spatially in each slice to reduce the impact of spatially-dependant biases; this was considered the most blinded approach in light of the fact that no independant anatomical scans were acquired. Outliers in each ROI were defined as voxels where the T_1 value was more than three standard deviations away from the mean and were excluded from the subsequent analysis. The mean and standard deviation over all ROIs were calculated for both tissues for T_1 and T_2 for both fully-sampled (FS) and undersampled CS reconstructions. The

statistical significance of differences in relaxation times between FS and CS reconstructions was assessed using a two-sample unpaired t-test with a significance level of 0.05, and the Bonferroni correction for multiple comparisons was applied.

All analyses were performed in MATLAB R2019b (The MathWorks, Natick, MA, USA).

3.6.3   Results

3.6.3.1 PLANET T_2 maps of retrospectively-undersampled reconstructions of in vitro phantom

Figure 7 below shows the PLANET maps obtained from the fully-sampled 3D Cartesian acquisition. Furthermore, co-registration was included as a pre-processing step in the received PLANET code; while it is not warranted for stationary phantom data, it did have a slight smoothing effect on the maps (see the reduction in the "ripples" in some vials in Figure 7B compared to Figure 7A).
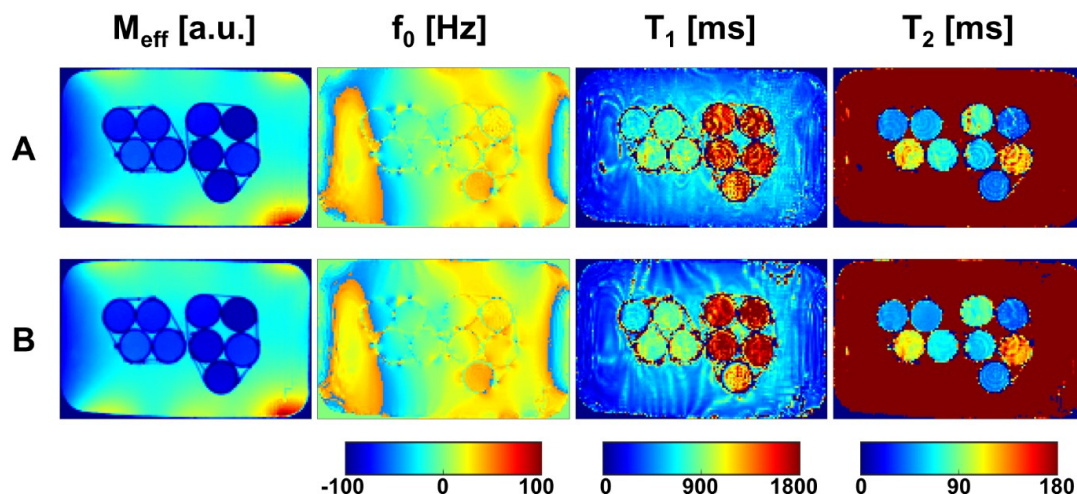
Figure 7. PLANET maps of effective magnitude M_{eff}, off-resonance Δf_0, T_1, and T_2, generated from A) non-co-registered and B) co-registered phase-cycled volumes. The acquisition was done at 3T (Prisma, Siemens Healthcare, Erlangen, Germany) with slab-selective excitation, a 3D Cartesian trajectory with linear phase encoding, and lowest slew-rate gradients.

TVs regularization improved map homogeneity, accuracy, and precision, while the effect of FT-PC regularization was evident only in combination with TVs regularization (Figure 8). Qualitatively, referring to Figure 8A, it can be seen that a lack of TVs regularization generated severe artefacts in the T_2 maps (top row) that degraded map quality, while adding TVs with a regularization weight of 0.001 removed these artefacts

and noticeably improved map homogeneity (bottom row). TVs regularization also removed the ripples seen in the fully-sampled map. The qualitative effect of FT-PC regularization appeared to be insignificant apart from a slight reduction of T_2 values for regularization weights higher than 0.001 (bottom row, Figure 8A). The (TVs = 0, FT-PC = 0) image is not actually the zero-filled image but can be considered as a type of SENSE reconstruction with Tikhonov regularization. Quantitatively, the use of TVs regularization improved the correlation of PLANET and ME-SE values to that of the fully-sampled case (Figure 8B), and greatly improved the precision of the T_2 values, in some cases exceeding that of the fully-sampled maps (Figure 8C). FT-PC regularization had an inconsistent effect on accuracy without TVs regularization, but appeared to decrease accuracy in combination with TVs (Figure 8B): specifically, the slope of the (0.001, 0) line matched that of the fully-sampled case and increasing the FT-PC weight decreased the slope of this line, reflecting its effect of decreasing T_2 values mentioned previously. FT-PC appeared to have an inconsistent and negligible effect on precision (Figure 8C), as the CoV was improved to the general precision of the fully-sampled case only with the use of TVs. The optimal FT-PC regularization weight from this experiment was chosen as 0.001 due to its slight improvement of map homogeneity without compromising accuracy, while TVs regularization with a weight of 0.001 was clearly necessary due to its improvement of accuracy and precision.

Figure 8. PLANET T_2 maps, accuracy, and precision of FT-PC and TVs regularized images compared to fully-sampled images. A) Maps for the fully-sampled and undersampled images with all combinations of regularization weights. B) Correlation of PLANET mean values with those of ME-SE reference technique. C) Coefficient of variation (CoV) in percent of PLANET maps. FS denotes the fully-sampled data, and the numbers in the legend in B and C indicate the FT-PC regularization weight. Note that the CoV values of the undersampled maps in C) were higher than 25% for TVs = 0.

Wavelet regularization improved map homogeneity, accuracy, and precision, although to a lesser extent that TVs regularization alone or in combination with it (Figure 9). Wavelet regularization qualitatively removed the artefacts seen in the (0, 0) image and improved map homogeneity in a weight-dependant manner (Figure 9A), although a

slight distortion at the edges of the top-right vial appeared to become more pronounced with greater weights. The addition of TVs further improved map homogeneity for all wavelet regularization weights. Wavelet regularization had a noticeable effect on accuracy, as the best-fit lines of correlation corresponding to non-zero weights approached that of the fully-sampled case (Figure 9B), although this effect appeared to be negligible when combined with TVs regularization. Wavelet regularization improved precision compared to the case with no wavelet and TVs regularization (Figure 9C), although the improvement was not as great as with TVs = 0.001 alone. The effect of the wavelet weight in combination with TVs = 0.001 appeared to be negligible (Figure 9C). In combination with TVs = 0.001, the optimal wavelet weight here was chosen as 0.001, as a compromise between map homogeneity and the distortions at the edges of the vials.
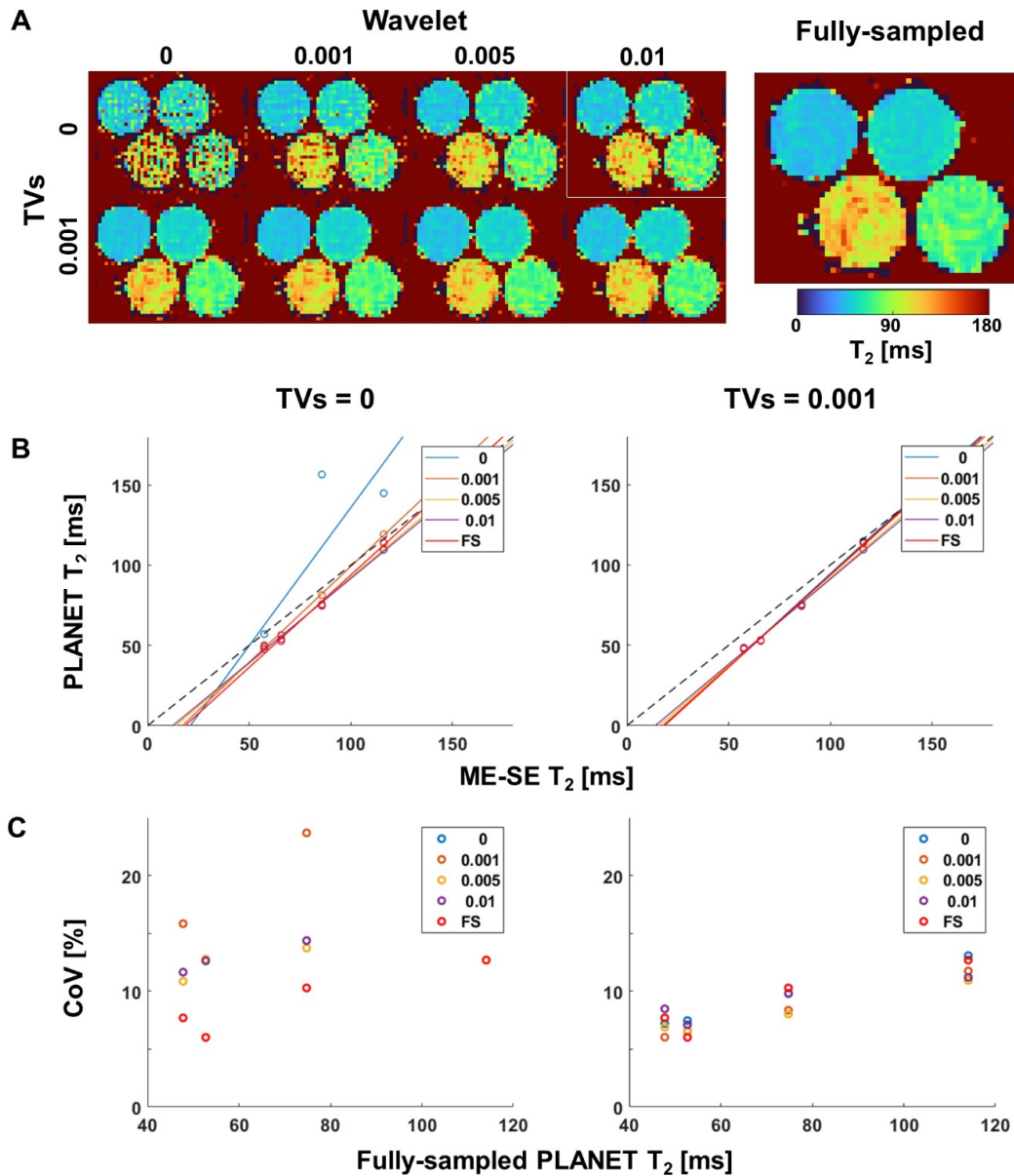
Figure 9. PLANET T$_2$ maps, accuracy, and precision of wavelet and TVs regularized images compared to fully-sampled images. A) Maps for the fully-sampled and undersampled images with all combinations of regularization weights. B) Correlation of PLANET mean values with those of ME-SE reference technique. B) Coefficient of variation (CoV) in percent of PLANET maps. FS denotes the fully-sampled data, and the numbers in the legend in B and C indicate the wavelet regularization weight.

The combination of (FT-PC = 0.001, wavelet = 0.001) regularization together with TVs regularization for the retrospectively-undersampled reconstruction successfully matched the map quality and accuracy and exceeded the precision of the fully-sampled reconstruction (Figure 10). These reconstructions also all used TVs = 0.001, as justified by the previous results. Qualitatively, the combination of FT-PC and wavelet

regularization appeared to yield a slight improvement in map homogeneity compared to using either type alone (Figure 10A). The qualitative map quality and homogeneity of the (0.001, 0.001) case were similar to the fully-sampled map, which itself had the ripple-like artefacts mentioned previously. The accuracy appeared relatively unchanged and similar to that of the fully-sampled case (Figure 10B). The combination of FT-PC and wavelet had a best-fit line with the lowest slope and sightly lower than that of (0, 0.001), similar to the previously-observed decrease of T_2 values by FT-PC regularization. While the use of either FT-PC or wavelet regularization alone inconsistently affected precision, their combination generated the highest precision (lowest CoV) among the undersampled reconstructions and even surpassed that of the fully-sampled maps (Figure 10C).
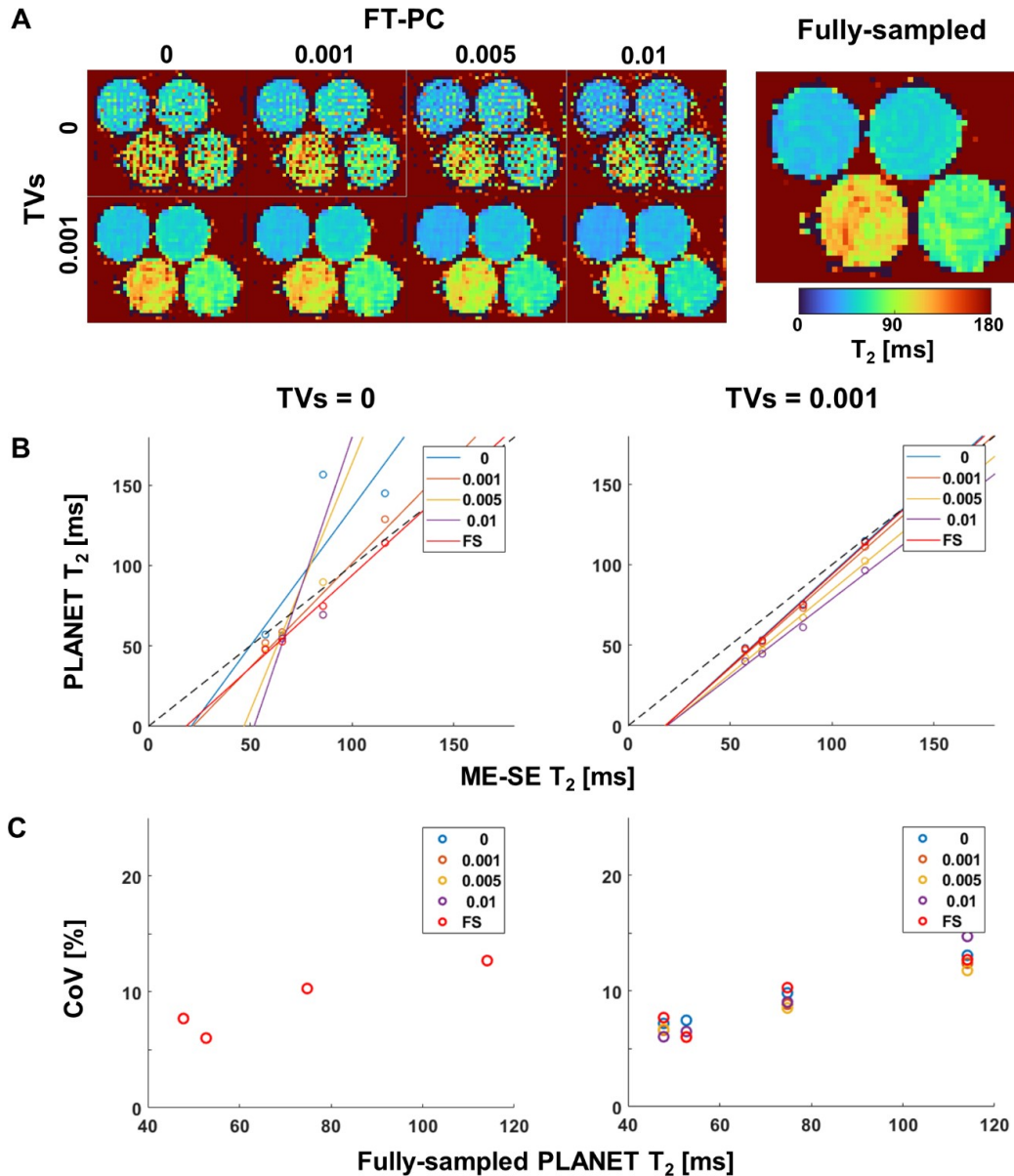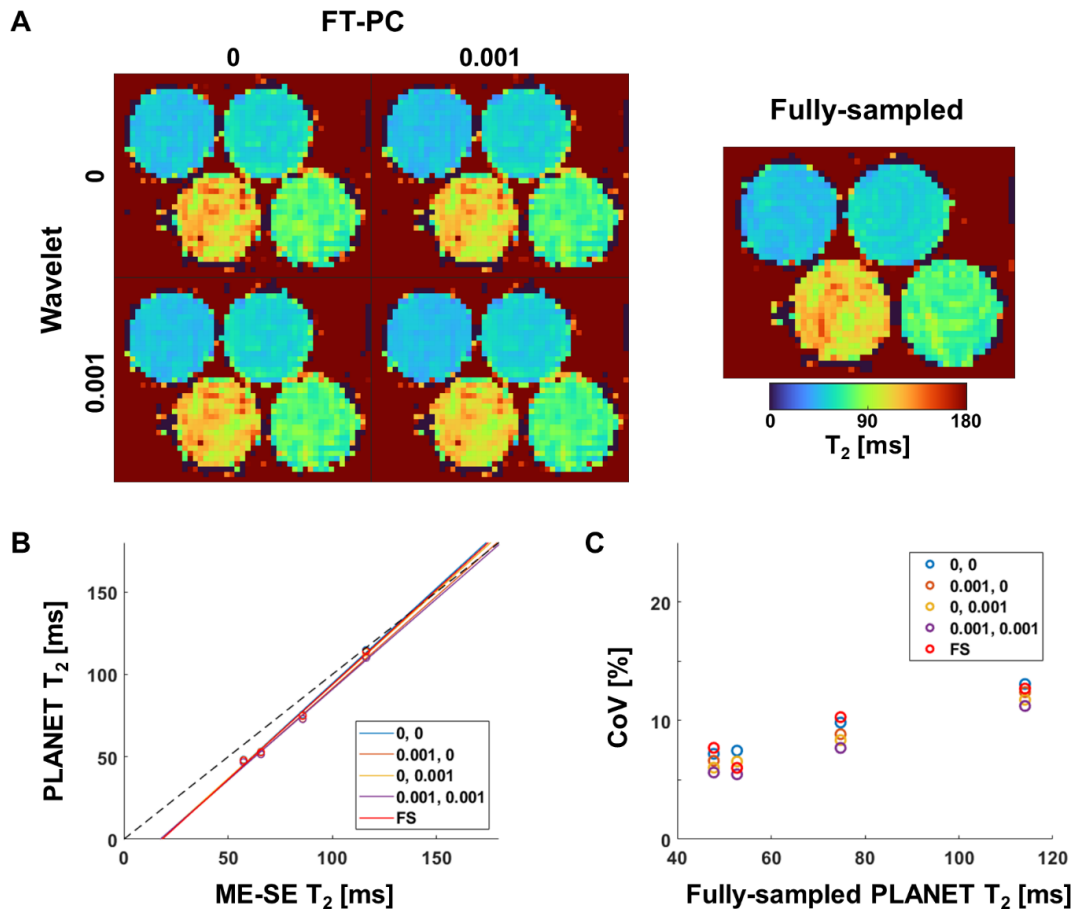
Figure 10. PLANET T_2 maps, accuracy, and precision of FT-PC, wavelet, and TVs regularized images compared to fully-sampled images. A) Maps for the fully-sampled and undersampled images with TVs and combinations of FT-PC and wavelet regularization. B) Correlation of PLANET mean values with those of ME-SE reference technique. B) Coefficient of variation (CoV) in percent of PLANET maps. FS denotes the fully-sampled data, and the numbers in the legend in B and C indicate the pair (FT-PC weight, wavelet weight).

A subset of the magnitude and phase images reconstructed with TVs = 0.001, FT-PC = 0.001, and wavelet = 0.001 regularization are shown in Figure 11. The banding artefacts visible in the magnitude images correspond to the sudden phase jumps. (yellow arrows, Figure 11) It was noted that the qualitative homogeneity of the T_1 and T_2 maps was related to the homogeneity of the phase images, which clearly depended on the regularization scheme, whereas the magnitude images were more robust and uncorrelated with the homogeneity of the T_1 and T_2 maps.
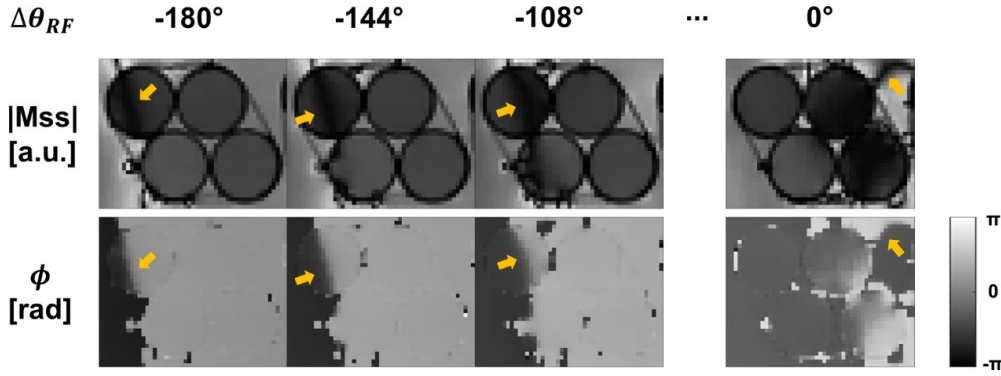
Figure 11. Magnitude, $|M_{ss}|$, and phase, ϕ, images from the retrospectively-undersampled reconstruction with TVs = 0.001, FT-PC = 0.001, and wavelet = 0.001 regularization. The images are shown for a subset of the phase cycles, $\Delta\theta_{RF}$. Yellow arrows indicate banding artefacts.

3.6.3.2 *PLANET T_1 and T_2 maps of retrospectively-undersampled in vivo brain acquisition*

PLANET T_1 and T_2 maps generated from a retrospectively-undersampled reconstruction (CS), using 0.001 for all three aforementioned types of regularization, of an in vivo brain acquisition matched the qualitative map homogeneity and mean values of the fully-sampled acquisition (Figure 12, Table 1). Qualitatively, the maps appeared similar between fully-sampled and CS reconstructions. However, certain horizontal and vertical artefacts in white matter posterior to the ventricles could be seen in the CS maps that did not resemble the spatial variation seen in the corresponding regions of the fully-sampled maps. The results of the corresponding ROI analyses for white and grey matter are shown in Table 1. The mean values of the retrospectively-undersampled reconstructions were similar to but slightly lower than the fully-sampled reconstruction, with a significant difference only occurring for white matter T_2. For white matter, T_1 values were 603 ± 119 ms and 601 ± 103 ms (p = 0.6) for FS and CS, respectively, and T_2 values were 54 ± 7 ms and 53 ± 7 ms, respectively (p < 0.001). For grey matter, T_1 values were 960 ± 615 ms and 944 ± 551 ms (p = 0.5) for FS and CS, respectively, and T_2 values were 75 ± 33 ms and 72 ± 24 ms, respectively (p = 0.02).
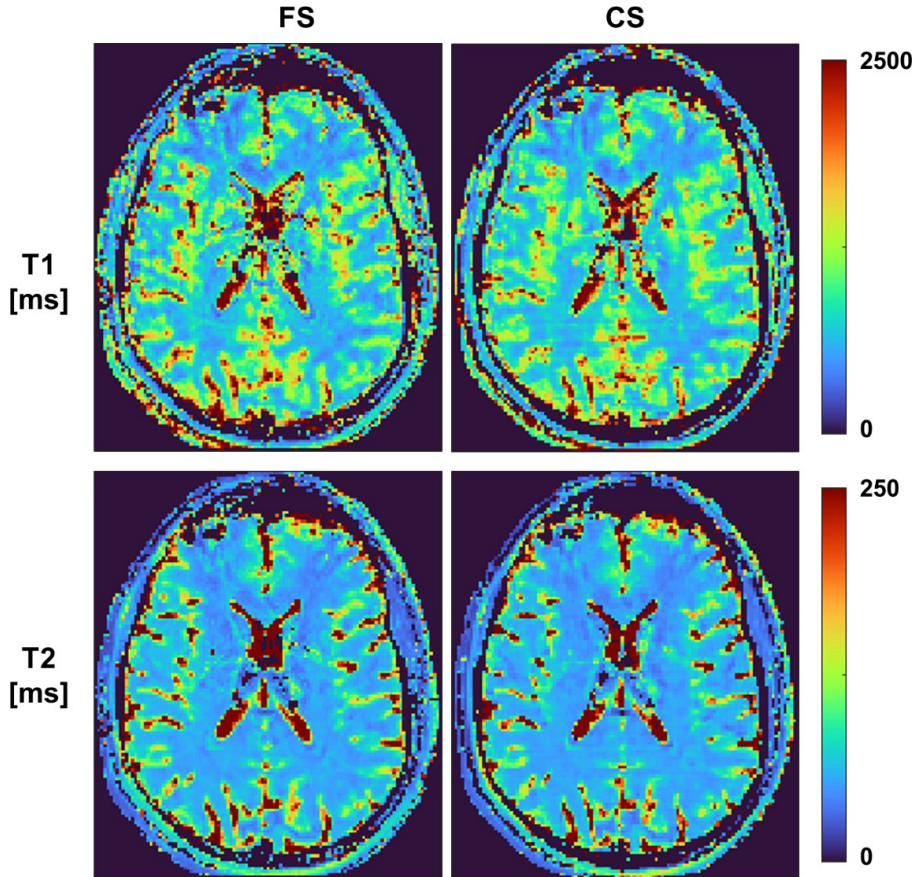
Figure 12. PLANET T_1 and T_2 maps of a human brain using fully-sampled (FS) reconstruction and retrospectively-undersampled reconstruction with TVs = 0.001, FT-PC = 0.001, and wavelet = 0.001 regularization (CS).

Table 1. In vivo relaxation times in the human brain estimated by PLANET using a fully-sampled (FS) and retrospectively-undersampled reconstruction with TVs = 0.001, FT-PC = 0.001, and wavelet = 0.001 regularization (CS). Data are presented as mean ± standard deviation.

	White matter		Grey matter	
	T_1 [ms]	T_2 [ms]	T_1 [ms]	T_2 [ms]
FS	603 ± 119	54 ± 7	960 ± 615	75 ± 33
CS	601 ± 103	53 ± 7	944 ± 551	72 ± 24

3.7 Free-running 5D PLANET for multiparametric myocardial mapping

3.7.1 Purpose

The purpose of this section was a preliminary examination of the feasibility of PLANET for free-running motion-resolved 5D myocardial T_1 and T_2 mapping, in terms of sequence parameters and in terms of the feasibility of radial imaging.

3.7.2 Methods

3.7.2.1 Numerical Monte Carlo simulations

Numerical simulations were performed to examine the optimal sequence parameters in terms of accuracy and precision for myocardial mapping with PLANET at 1.5T. Acceptable parameters were those that kept accuracy to within 5% of the true value with a maximum standard deviation of 10% about the mean. Only the T_2 relaxation time was considered, because the feasibility of cardiac free-running B_1 mapping was unclear, and 1.5T was chosen as it is currently the most common field strength for cardiac MRI. Non-noisy phase-cycled data were simulated using Equation (9), and 10 000 Monte Carlo experiments were performed in which zero-mean Gaussian noise was added separately to the real and imaginary components of the complex steady-state signal. Two sets of experiments were run with Guassian noise with standard deviations of 0.001 and 0.002, respectively, in order to assess the effect of SNR. A standard deviation of 0.001 generated phase-cycled SNR from 50 to 100, and ranged from 1% to 2.3% of the magnitudes of the geometric centres of the individual non-noisy ellipses. A standard deviation of 0.002 generated phase-cycled SNR in the range of 0 to 50, which was comparable to the SNR values calculated during the LIBRE study in Section 2.3.2. Accuracy was assessed as the difference between the mean and true T_2 values normalized by the true T_2 value, as was done in (192). Precision was assessed as the coefficient of variation, being the standard deviation of the T_2 values divided by the mean value, as was done in (192). SNR for these phase-cycled data were calculated as in (64,200), namely as the average magnitude of the bSSFP signal among the phase cycles (magnitude of the geometric ellipse centre) divided by the standard deviation of noise. Simulated sequence parameters were: RF excitation angle from 4° to 60° in increments of 4°; TR from 2 to 10 ms; number of RF phase increments, N, was 6, 8, and 10; M0 = 1; T_1 = 960 ms; T_2 = 50 ms; Δf_0 = 0 Hz; φ_{RF} = 0. Higher TR and N values were not examined due to the acquisition time of a 5D radial acquisition with 2-mm isotropic voxel size, 2055 shots, 22 segments, TR = 10 ms, and N = 10, already being 75 minutes. The simulations were performed in MATLAB 2019b (The MathWorks, Natick, MA, USA).

3.7.2.2 3D Cartesian and 3D radial acquisitions of phantom

PLANET map homogeneity between 3D Cartesian and 3D radial acquisitions was compared. 3D k-space data of a vial phantom were acquired at 1.5T (MAGNETOM Sola, Siemens Healthcare, Erlangen, Germany) with a 64-channel head coil. The vial phantom was the same as in Section 3.6.2.3 and was placed in a container filled with gadolinium-doped water. One acquisition involved a fully-sampled 3D slab-selective Cartesian

acquisition with linear phase encoding, for which relevant acquisition parameters were: TE/TR = 5.00/9.99 ms; FOV = 220 x 220 x 150 mm^3; matrix size = 144 x 144 x 60 with 25% slice oversampling; voxel size = 1.5 x 1.5 x 2.5; RF excitation angle = 30°; 144 dummy excitations; N = 10 RF phase-cycling schemes starting from -180° in increments of 36°; lowest gradient slew rate setting. A second acquisition used the 3D radial spiral phyllotaxis trajectory (48) with slab-selective excitation: TE/TR = 4.95/9.93 ms; FOV = 220 x 220 x 220 mm^3; matrix size = 112 isotropic; voxel size = 2.0 mm^3 isotropic; RF excitation angle = 30°; 112 dummy excitations; N = 10 RF phase-cycling schemes starting from -180° in increments of 36°; lowest gradient slew rate setting. The voxel size used for the radial acquisition was that anticipated to be used in vivo in the heart and was also chosen to offset the inherent SNR decrease with radial acquisitions compared to Cartesian acquisitions.

3.7.2.3 Image reconstruction

The reconstruction pipeline for the 3D Cartesian images followed that of Section 3.6.2.2. The 3D radial reconstructions used a modified version of Jérôme Yerly's 5D radial version with the relevant parameters appropriately set to reconstruct a static image. The trajectory delay correction algorithm from the original 5D reconstruction (54) was not used, as preliminary investigations showed it degraded map quality. The radial streaking reduction procedure, based on that in (201), was also not used.

3.7.2.4 Image pre-processing and PLANET map generation

PLANET was run for both acquisitions as described in Section 3.5. The mask described in Section 3.6.2.5 was also used here. The unringing algorithm (182) was run prior to PLANET only for the Cartesian images, as it is not applicable to non-Cartesian data.

3.7.3 Results

3.7.3.1 Numerical Monte Carlo simulations

The results of the Monte Carlo simulations of PLANET T_2 performance on myocardial tissue are shown in Figure 13 for added Gaussian noise with an SD of 0.001, and in Figure 14 for Gaussian noise with an SD of 0.002. SNR ranged from approximately 50 to 100 for added noise with an SD of 0.001 (Figure 13C) and from 0 to 50 for added noise with an SD of 0.002 (Figure 14C), and was primarily affected by the RF excitation angle. Referring to Figure 13A and Figure 14A, the accuracy of T_2 estimation depended on the TR, RF excitation angle, and the number of phase cycles. There was a broad range of

parameters that kept the relative accuracy below 5%; for example, for a noise SD of 0.001 (Figure 13A), this region included RF excitation angles from 6° to 40°, TRs from 5 to 10 ms, and N from 6 to 10. This region of robust RF excitation angles and TRs expanded with higher N, which also improved accuracy in general, but contracted with lower SNR (comparing Figure 13A and Figure 14A). The regions on the left-hand side of the plots where the absolute value of the accuracy was greater than 5% corresponded to areas where the RF excitation angle was equal to the Ernst angle and the ellipse devolved into a line, as described in (64). The precision of the T_2 estimate showed a similar variation with the three sequence parameters and SNR as the accuracy (Figure 13B and Figure 14B). Taking the example of an RF excitation angle of 20°, TR of 8 ms, and N of 8, we see that T_2 accuracy and precision were 0.2% and 3.3%, respectively, for a noise SD of 0.001 (Figure 13A,B), and they decreased to 0.8% and 6.9%, respectively, for a noise SD of 0.002 (Figure 14A,B). However, TR ccould be brought as low as 5 ms with an RF excitation angle of 12° and 10 RF phase increments.
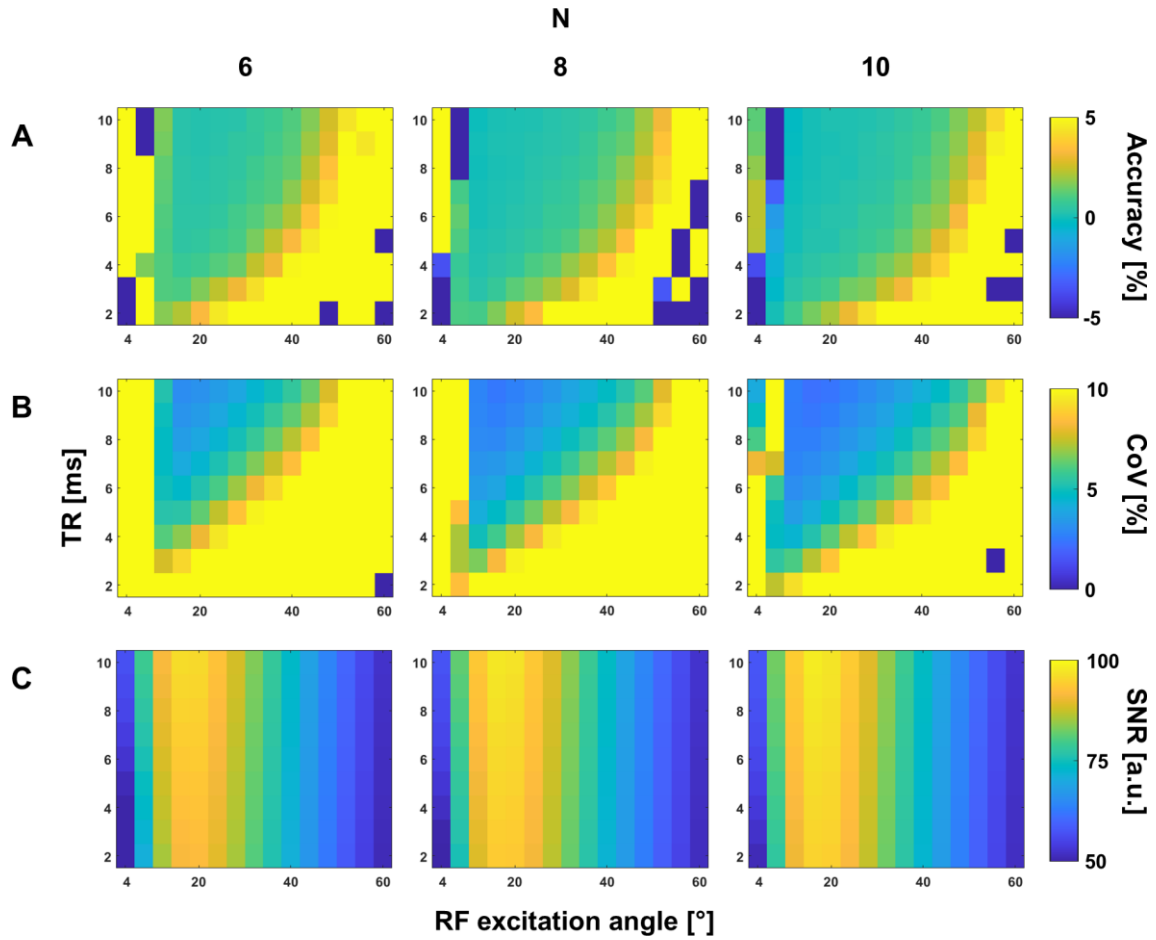
Figure 13. Results of Monte Carlo simulations of PLANET T_2 performance in human myocardium at 1.5T, with added Gaussian noise with standard deviation of 0.001. Shown are A) relative accuracy (%), B) coefficient of variation (%) as a proxy of precision, and C) SNR as functions of the number of phase cycles (N, columns), TR (vertical axis), and RF excitation angle (horizontal axis).
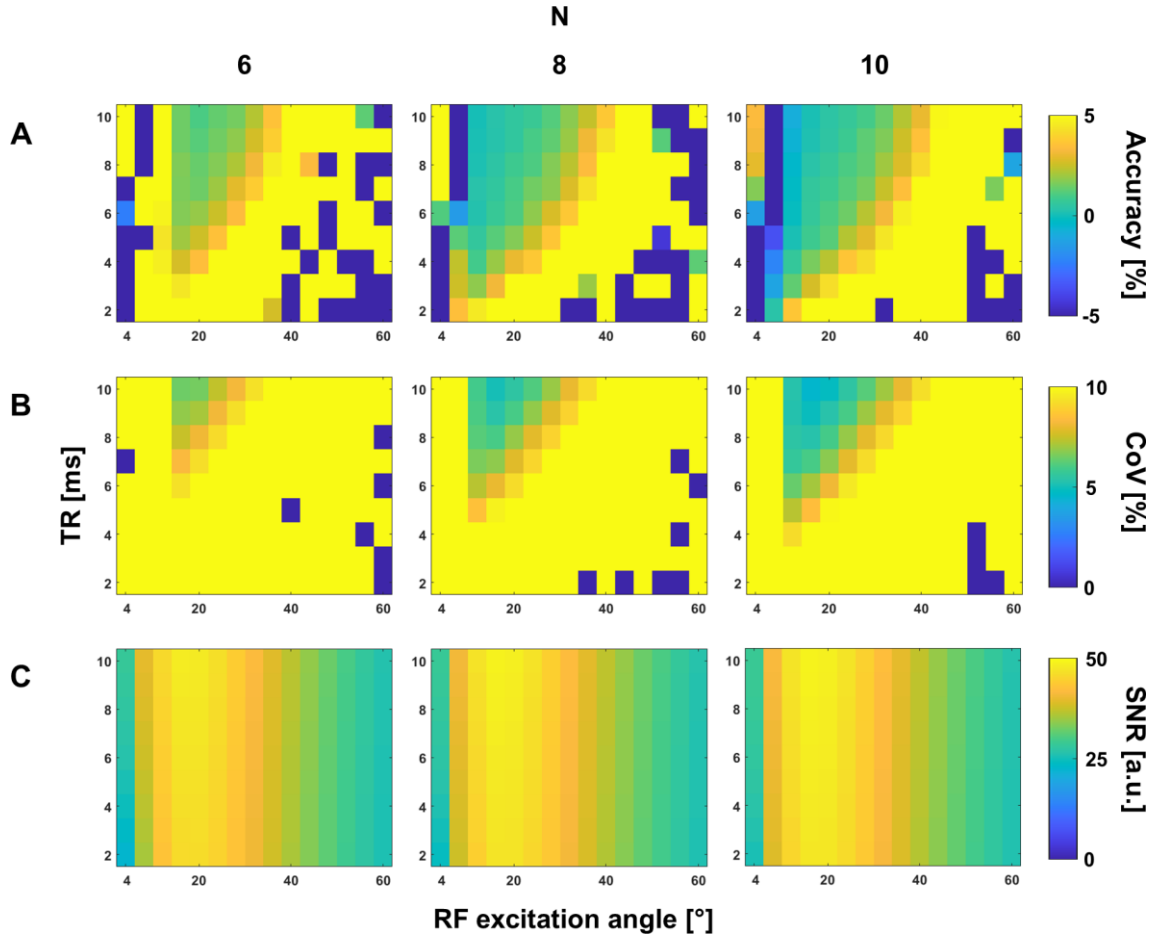
Figure 14. Results of Monte Carlo simulations of PLANET T_2 performance in human myocardium at 1.5T, with added Gaussian noise with standard deviation of 0.002. Shown are A) relative accuracy (%), B) coefficient of variation (%) as a proxy of precision, and C) SNR as functions of the number of phase cycles (N, columns), TR (vertical axis), and RF excitation angle (horizontal axis).

3.7.3.2 PLANET maps of in vitro Cartesian and radial acquisitions

The map homogeneity and numerical values of radial PLANET acquisitions did not closely match those of Cartesian acquisitions of a phantom (Figure 15). The map homogeneity of these 3D Cartesian maps acquired at 1.5T (Figure 15A) appeared similar to those acquired at 3T (Figure 7). The radial maps had an overall lower homogeneity and quality (Figure 15B). The radial M_{eff} and Δf_0 maps displayed similar values as the Cartesian ones, although concentric rings could be seen in the radial M_{eff} maps. The radial T_1 maps did not have matching values as the Cartesian maps and did not appear to correctly map T_1, as five of the nine vials had similar T_1 values as the interior of the phantom and the other four were largely masked out. Regarding the radial T_2 maps, the four vials on the left appeared to have differences in T_2 that somewhat reflected those seen in the Cartesian map, although there also appeared to be spurious variations of T_2

that were not seen in the Cartesian map; the other five vials had either spurious variations not seen in the Cartesian maps or else were masked out. The magnitude and phase maps of the Cartesian and radial phase-cycled images were qualitatively similar, and the phase maps both showed similar RF-phase-increment-dependant variations of the banding artefacts (data not shown).
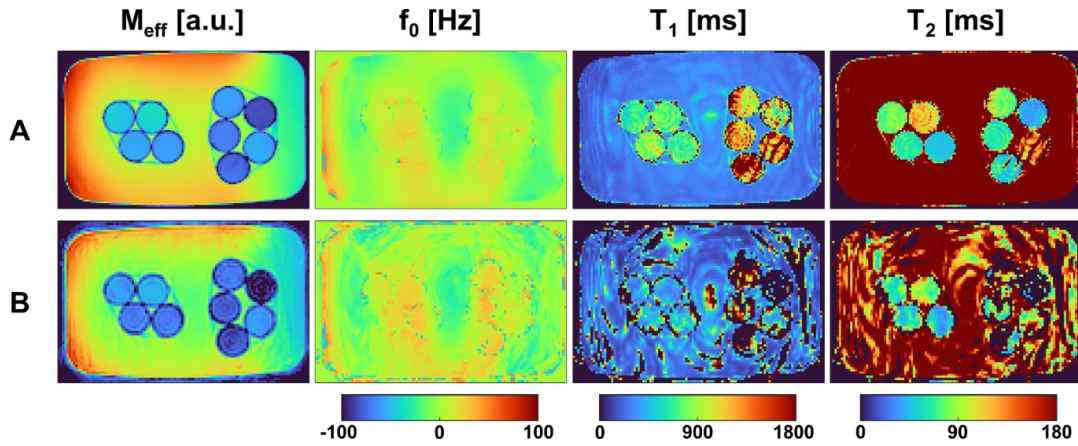
Figure 15. PLANET maps acquired in vitro in a phantom at 1.5T using A) a 3D Cartesian trajectory with linear phase encoding and B) 3D radial phyllotaxis trajectory.

3.8   Discussion

3.8.1   Summary of results

PLANET T_1 and T_2 maps homogeneity, accuracy, and precision were successfully maintained despite a two-fold acceleration with a retrospective reconstruction of a 3D Cartesian phantom acquisition (Figure 10). The specific regularization parameters used were 0.001 each for spatial TV regularization (TVs), Fourier transform regularization along the phase cycle dimension (FT-PC), and spatial wavelet regularization. It was found that the qualitative and quantitative performance of PLANET depended on the regularization scheme: TVs regularization had a clear effect on homogeneity, accuracy, and precision (Figure 8 and Figure 9), while wavelet regularization had a less pronounced effect on these three features (Figure 9) and FT-PC appeared to have a negligible effect (Figure 8). The homogeneity of the PLANET T_1 and T_2 maps was related to the homogeneity of the individual phase images (Figure 11). In a two-times accelerated retrospectively-undersampled reconstruction of an in vivo brain acquisition, map homogeneity and mean values and standard deviation were similar to the fully-sampled reconstruction (Figure 12 and Table 1).

Preliminarily, it was also shown that PLANET could theoretically estimate T_2 accuracy to within 5% and precision to within 10% over a broad range of parameters, confirming the feasibility of myocardial mapping with PLANET (Figure 14). In fact, TR can be brought as low as 5 ms without exceeding these limits on performance, which would equate to a total 5D scan time of 38 minutes with a spatial resolution of 2-mm isotropic, 10 RF phase increments, 22 segments, 2055 shots, and no acceleration along the phase cycle dimension. However, preliminary in vitro results with PLANET applied to a 3D radial phyllotaxis acquisition showed inaccurate T_1 and T_2 values and poor map homogeneity (Figure 15).

3.8.2 Discussion of results

3.8.2.1 Static in vitro and in vivo acquisitions

An initial investigation of regularization schemes was performed in this study. It was found that TVs regularization appeared to have the greatest effect on PLANET T_2 accuracy and precision, whereas FT-PC was found to have a minor effect. This finding is somewhat surprising considering that FT-PC exploits the properties of the phase-cycled signal unlike TVs, although FT-PC only operates on the data for a single voxel. As was shown briefly in this study, the effect of FT-PC may only be evident in combination with TVs or another type of regularization that denoises the data by ensuring voxel-to-voxel consistency, which warrants further investigation. Instead of ensuring spatial consistency, as TVs does, it may be possible to devise a regularization scheme that ensures consistency between neighbouring ellipses. A technique such as ReCat (202), which uses a tensor kernel to estimate missing k-space samples by exploiting redundancies across both coil and phase-cycle dimensions, may enable higher acceleration factors and can perhaps be integrated into HD-PROST (170) for a denoised phase-cycled bSSFP reconstruction. In any case, a more thorough sweep of regularization weights or an approach inspired by sparsity adaptive composite recovery (203) may provide more optimal regularization weights. Finally, it should be mentioned that it was found, without thorough investigation, that there was a limit to how much a denoising scheme could improve the accuracy of PLANET, and that acquisitions would still need to use appropriate sequence parameters to achieve the desired PLANET performance.

Throughout this study, there was the underlying question of what constituted acceptable fully-sampled PLANET maps. Referring to Figure Figure 7, neither set of maps was as homogeneous as the in vitro maps in the first PLANET paper (64), raising

the question of what the effect of scanner vendor and hardware – influencing aspects such as B_1 inhomogeneities and coil sensitivity estimation – is on map quality. Moreover, co-registration improved PLANET map homogeneity (Figure 7B), even though co-registration would not be warranted for the case of an inanimate sample that undergoes no inter-scan movement. Both co-registration and FT-PC regularization with a weight of 0.01 can generate a correlation (with ME-SE) best-fit line with a slope of approximately 1 (full data not shown). The implication of this is that the overestimation of T_2 values by ME-SE is approximately constant, which is in fact expected, raising the question of whether such PLANET maps are in fact more accurate than the non-registered ones used as the reference in Section 3.6.3.1.

There are considerations regarding the undersampling scheme and trajectory. The present reconstructions were only retrospectively-undersampled. Prospectively-undersampled acquisitions may suffer from eddy current and other effects, which would degrade the performance of PLANET compared to what was shown in this thesis, and would warrant further investigation of the optimal trajectory and reconstruction scheme. In the case of the Cartesian spiral trajectory used here, the redundant sampling of the central k-space regions would mean that, in practice, an average of these k-space samples would be taken, which may have the overall effect of increasing SNR for these central coefficients, which largely determine contrast in the image, and hence the image. It may also be possible to use the redundant positions to assess intra-acquisition rigid motion, although this would require further investigation. Furthermore, the particular undersampled trajectory used here had a fully-sampled 24 × 24 central region for coil sensitivity estimation, which was difficult to achieve for acceleration factors above two considering the random nature of the trajectory. The significance of the coil sensitivity is that preliminary work suggested that suboptimal estimates generated artefacts in the phase images and reduced the precision and homogeneity of the T_1 and T_2 maps. An initial fully-sampled low-resolution reference scan (204) can alternatively be used to provide the required data, which would take under 10 s in this case and would be offset by the 4min50s reduction offered by the scan acceleration. Alternatively, the coil sensitivities can be estimated with an additional low-resolution scan using the body coil, which is the subject of current work in the lab. Either approach would alleviate restrictions on the acceleration factor for this trajectory and open up the use of other trajectories. As a side note, it was found that PLANET can be effectively run on single-coil images and, although the resulting maps were not as homogeneous as the maps from the coil-combined images (data not shown), it raises the possibility of using the output M_{eff} for coil sensitivity estimation in a first iteration.

A previous study exploring banding artefact reduction was able to achieve acceleration factors up to four with acceptable image quality (205), compared to two in the present study. The higher achievable acceleration factor may be explained by the fact that they ensured the central 10% region of k-space was fully-sampled and independently sampled the periphery, whereas we modified the parameters of a published trajectory to natively obtain such a region but were in turn constrained by the acceleration factor. Additionally, their banding artefact reduction used the magnitude images, whereas we have found that the PLANET T_1 and T_2 estimates depend rather on the phase images, which were also more sensitive to the regularization scheme than the magnitude images. They found that employing different sampling patterns per phase-cycled acquisition and using variable-density trajectories improved the final mage quality, which we had used in our study.

The PLANET technique itself can be further modified. The published PLANET technique used linear series of RF phase increments, but the merit of non-linear increments remains to be explored. For example, the Cramer-Rao lower bound (206) may inform about more optimal phase-cycling schemes. As was mentioned previously in Section 3.5, sections of the algorithm can be changed. A constrained ellipse fitting approach reduced the number of required acquisitions for PLANET to four while maintaining map quality and accuracy (190), and therefore holds promise for reducing the PLANET acquisition time. It should be noted that the simulations in this study or in (192), which use no less than six acquisitions, were based on the current direct ellipse-fitting approach (158,189) and do not apply to this alternative technique. The off-resonance estimation can be substituted with the Fourier-transform-based approach in (194), which was shown to have a higher precision, although the improvement in computational time remains to be elucidated. It also appeared that PLANET T_2 accuracy and precision had a nonlinear relationship with SNR (Section 3.7.3.1), which is a topic that has not been examined in detail to date in the literature and warrants exploration. On a separate note, should it be found that higher numbers of phase cycles are optimal for PLANET, the use of MIRACLE for estimating T_1 and T_2 relaxation times might be merited, as its sensitivity to off-resonance would then be mitigated (see Section 3.2.2.3).

Finally, the retrospectively-undersampled brain reconstructions will be discussed. While the fully-sampled and undersampled mean values were similar (Table 1), the undersampled T_1 and T_2 values were slightly lower, which was likely a consequence of the already-noted reduction of T_2 values due to FT-PC regularization (Figure 12). A previous PLANET study at 3T consisting of five volunteers found white matter T_1 and

T_2 of 664 ± 58 ms and 52 ± 5 ms, respectively, and 1096 ± 91 ms and 65 ± 10 ms for grey matter (192). We obtained lower T_1 values by approximately 10% and similar T_2 values, albeit with larger standard deviations; the underestimation of T_1 can be accounted for by the lack of a B_1 correction (64). PLANET underestimates relaxation times in the brain compared to conventional methods (192), which has been explained as being due to asymmetries in the bSSFP profile caused by multi-component tissues (64,153,207). Co-registration was performed on the phase-cycled images prior to running PLANET but was not incorporated into the reconstruction, which may have limited the validity of FT-PC regularization in case inter-acquisition movement was significant.

3.8.2.2 Dynamic free-running cardiac acquisitions

Numerical Monte Carlo simulations showed that myocardial mapping at 1.5T with PLANET was theoretically possible with feasible sequence parameters, and TR could be reduced by tuning the RF excitation angle and number of RF phase increments. Together with the finding that the acquisition can be accelerated two-fold, with perhaps higher accelerations possible with more robust coil sensitivity estimation methods, this suggested that the low-resolution 5D phase-cycled scan time could be accelerated from the 38 minute scan time mentioned above to possibly under 20 minutes. The previous discussions about regularization schemes, coil sensitivity estimation, and improving the PLANET algorithm also apply for this case.

However, PLANET T_1 and T_2 estimates from a 3D radial acquisition showed poor accuracy and homogeneity compared to a 3D Cartesian acquisition. Considering the effect of SNR on accuracy and precision documented in this thesis and in published work (192), it may be that the inherently lower SNR of radial acquisitions is the cause of such maps, and it remains to be seen to what extent regularization in a CS reconstruction can improve the radial maps. Severe eddy current effects may also be responsible, which may necessitate modifications to the radial trajectory, such as pairing of readouts (208). Gradient delays leading to trajectory imperfections may be another cause, although initial results using the trajectory delay correction for the 3D radial phyllotaxis trajectory presented in (54) did not improve map quality. Finally, PLANET map quality with a chest coil, which would be used for cardiac acquisitions, remains to be investigated, although a reduction in SNR is expected as the coil is larger and the imaged heart is normally farther from the coil than in the case of the brain.

Preliminary work showed that the fully self-gated motion signal extraction (54) was unaffected by phase cycling, and it was hypothesized that, as fat generally had bright signal regardless of the phase cycling scheme, the algorithm detected primarily the motion of fat. The robustness of the motion extraction and possible alternatives, such as the Pilot-Tone (124), remain to be examined.

3.8.3 Further work

Concerning PLANET with the static 3D Cartesian acquisition, it should first be clarified what constitutes acceptable fully-sampled PLANET maps. The performance of PLANET with a prospectively-sampled acquisition should be examined, and further work should explore alternative trajectories and determine the most efficient way to obtain accurate coil sensitivity estimates. B_1 maps should be acquired to enable accurate T_1 mapping with PLANET. The regularization scheme should be optimized and its effect on the performance of PLANET elucidated.

The cause of the low-quality radial PLANET maps would then need to be investigated. Coil weighting would need to be added and tested, and the angular delay correction algorithm would need to be re-optimized. The other considerations of low SNR, coil hardware, and eddy current effects should then be examined. The use of different trajectories, such as the spiral Cartesian trajectory (Section 3.6.2.1), should also be considered.

After the previous questions have been resolved and PLANET better understood, the focus of the work can shift to 5D free-running myocardial PLANET. The effect of motion on PLANET should be examined with simulations first to ensure that it is theoretically feasible, starting with simple objects undergoing 4D translation, then moving to numerical phantoms of the human heart incorporating respiratory and cardiac motion, such as the one used in the lab (123). An intermediate step could also investigate translational motion in vitro in a moving phantom, which would give an indication of feasibility and the effect of real-world confounders, such as eddy currents, during simple motion prior to application to in vivo cardiac imaging. Cardiac B_1 mapping should be investigated, including the possibility of free-running B_1 mapping or obtaining the B_1 estimate from the phase-cycled data itself. Assuming 5D PLANET works, an in vivo optimization and full study would follow.

3.8.4   Conclusions and outlook

In this preliminary retrospective study, it was shown that PLANET accuracy and precision could be maintained despite two-fold acceleration with a 3D spiral Cartesian trajectory. Myocardial mapping with PLANET was also shown to be theoretically possible with numerical simulations, although initial results with the 3D radial trajectory that had been originally used for 5D imaging did not match the quality of the Cartesian maps. Further work should focus on optimizing the regularization scheme, ensuring robust coil sensitivity estimates in prospective acquisitions, and investigating radial PLANET and the effect of motion.

While this study did not proceed to that stage, 5D free-running myocardial mapping would have the benefit of enabling mapping without the need for ECG set-up or breath-holds while avoiding the possible confounders present in some other techniques. Related to what was discussed in Section 2.5, its use of a well-known sequence, bSSFP, and its short computational time would make it readily accessible. It may even be possible to use spectrally-selective excitation or some kind of water-fat separation technique, analogously to how slab-selective excitation was used in this study, to avoid the previously-mentioned problems with estimation in voxels containing both water and fat in the heart.

In this study, PLANET maps appeared equally homogeneous on a 1.5T system and a high-performance 3T system. Translation to higher field would need to tackle the problem of higher B_1 inhomogeneities at high-field (131) for accurate T_1 mapping. PLANET at low-field would benefit from the reduced B_1 inhomogeneities, theoretically permitting more accurate T_1 mapping, and also from the reduced system heating, which would reduce the risk of B_0 drift affecting the relaxation times.

4 CONCLUSIONS AND OUTLOOK

This thesis focused on the application of steady-state techniques to free-running cardiac MRI for both anatomical and quantitative imaging. The development of the free-running framework at the start of my PhD, combining an interrupted free-running 3D radial acquisition with XD-GRASP motion-resolved reconstruction and cardiac and respiratory self-gating, critically improved the simplicity and ease-of-use of the cardiac MRI workflow. The first study focused on anatomical imaging and attempting to reduce the acquisition time of the free-running framework, showing that integration of LIBRE pulses into an uninterrupted bSSFP sequence reduced scan time and SAR while maintaining vessel conspicuity compared to the previous interrupted acquisition. Inspired by the results of this first project, the second study focused on quantitative imaging, showing that a novel multiparametric mapping technique could be accelerated in static tissue with a view to translating it to free-running 5D myocardial mapping.

In the first part (Chapter 2), the challenge was to improve upon the interrupted bSSFP acquisition of the free-running framework and mitigate its disadvantages of an interrupted steady-state, reduced duty cycle, reduced time efficiency, and increased SAR. It was hypothesized that LIBRE pulses, a novel off-resonant fat-suppressing pulse developed in our lab, would reduce scan time and SAR in an uninterrupted bSSFP acquisition relative to the interrupted acquisition. LIBRE pulses were successfully used for fully self-gated uninterrupted free-running 5D cardiac MRI. The uninterrupted free-running LIBRE approach reduced scan time and SAR compared to the interrupted acquisition, and maintained image quality and vessel conspicuity relative to the interrupted and an alternative uninterrupted acquisition. Building upon the reduction of operator-dependance and subject-specific cardiac gating of the published free-running framework, the free-running LIBRE approach further addressed the problems of cardiac sequence availability by using a conventional bSSFP sequence and of acquisition time by reducing the acquisition time of the free-running acquisition. The use of fNAV reconstruction additionally provided an avenue to address the long reconstruction time at the expense of motion resolution, reducing reconstruction time

by a factor of eight while maintaining image quality. Further work should investigate the feasibility of extracting functional information, optimizing the LIBRE parameters for robustness, new methods of obtaining or extracting motion signals, and investigating LIBRE and alternative techniques at different field strengths.

In the second part (Chapter 3), the goal was to perform free-running 5D T_1 and T_2 mapping of the myocardium. It was hypothesized that a new technique, PLANET, that uses a bSSFP acquisition was readily applicable to the free-running framework and could enable 5D myocardial mapping. After a phase of attempting to reproduce published results and understand the technique, it was shown that PLANET accuracy and precision could be maintained with two-fold acceleration in a retrospectively-undersampled reconstruction, and that myocardial PLANET mapping was theoretically feasible with reasonable sequence parameters. Further work is needed to clarify the optimal reconstruction scheme, provide robust coil sensitivity estimates, and optimize the radial trajectory for use with PLANET.

Both approaches utilized a steady-state acquisition and manipulated different properties of the steady-state signal using the RF excitation frequency. The LIBRE technique used off-resonant RF excitation, changing the frequency of B_1 in the Larmor frame, to manipulate the tissue frequency profile to suppress signal in a broad region around fat tissue frequencies and, thereby, generate blood-fat contrast for uninterrupted free-running 5D cardiac MRI. The PLANET technique required different RF phase increments, namely the incrementing of the position of the B_1 vector in the Larmor frame after each excitation, to exploit the elliptical signal model of bSSFP to estimate relaxation times for uninterrupted free-running 5D myocardial mapping. In fact, the use of an uninterrupted bSSFP acquisition also distinguished these techniques from most of the published methods in another way, namely the lack of interruption of the readout train. Both projects used numerical simulations to determine optimal sequence parameters and then independantly accelerated the acquisitions using undersampling and compressed sensing reconstructions, suggesting that steady-state techniques allow decoupling of optimal acquisition and reconstruction schemes to some extent. Because bSSFP properties can often be tuned for different purposes, it remains to be seen whether a phase-cycled bSSFP acquisition can be used both for multiparametric mapping with PLANET and for fat suppression using only the $\Delta\theta_{RF} = 0°$ and $\Delta\theta_{RF} = 180°$ acquisitions with the technique described in Quist et al. (86). Moreover, a phase-cycled technique like the one in Quist et al. (86) that is not as sensitive to imperfections in phase may be a better testbed to investigate the feasibility of phase-cycled bSSFP for

cardiac MRI. One disadvantage of steady-state techniques is the need to reach the steady-state and imaging data collected prior to that point may be subject to oscillations during the transient phase. No elaborate attempts were made in either study to reduce the severity and duration of these oscillations: the free-running LIBRE reconstruction removed the first 10 shots (220 excitations), which qualitatively appeared to be more than sufficient to account for oscillations, while the PLANET acquisitions had 100 to 150 dummy excitations, which would have been theoretically sufficient given the low off-resonance encountered with the brain coil. For the PLANET acquisitions, one possible transition scheme between acquisitions is to add dummy excitations where the RF phase increment is gradually changed, as was done in (156), reducing the required number of dummy excitations to 40 between acquisitions. Such a transition would have the benefit of turning PLANET into a single-acquisition technique and eliminating the need to account for inter-scan differences.

Both techniques address the current challenges in cardiac MRI of ease-of-use and clinical availability of sequences. Free-running bSSFP sequences are simple, having a simple theoretical background and allowing the decoupling of acquisition and reconstruction, and are readily available across MRI scanner manufacturers. Their translation to low-field systems appears feasible and perhaps even beneficial, considering that LIBRE would benefit from reduced B_0 inhomogeneities for ultimately increased TR and SNR, and PLANET would benefit from reduced B_1 inhomogeneities, for improved T_1 estimation, and reduced B_0 drift for improved accuracy overall. Low-field free-running bSSFP techniques have the potential to reduce medical costs by reducing scanner costs, removing the need for specialized sequences and MR technicians, and standardizing acquisition times for enhanced planning.

LIST OF PUBLICATIONS AND AWARDS

Peer-reviewed journal articles

Koush Y, **Masala N**, Scharnowski F, Van De Ville D. Data-driven tensor independent component analysis for model-based connectivity neurofeedback. Neuroimage. 2019;184:214-226. doi:10.1016/j.neuroimage.2018.08.067.

Masala N, Bastiaansen JAM, Di Sopra L, Roy CW, Piccini, D, Yerly, J, Colotti R, Stuber M. Free-running 5D coronary MR angiography at 1.5T using LIBRE water excitation pulses. Magn Reson Med. 2020;84(3):1470-1485. doi:10.1002/mrm.28221.

Manuscripts in preparation

Roy CW, Yerly J, Bastiaansen JAM, **Masala N**, Di Sopra L, Wetzl J, Forman C, Piccini D, Stuber M. A Comparison of Cartesian and radial trajectories for cardiac and respiratory motion-resolved 5D MRI using a free-running framework.

Peer-reviewed conference abstracts

Masala N, Bastiaansen JAM, Piccini D, Stuber M. Fat suppression in 3D bSSFP coronary MRA using lipid-insensitive binomial off-resonant RF excitation (LIBRE) pulses. In: Proceedings of the Society for Cardiovascular Magnetic Resonance 22nd Annual Scientific Sessions. Bellevue, USA; 2019:QF2-006.

Masala N, Bastiaansen JAM, Di Sopra L, Piccini D, Yerly J, Colotti R, Stuber M. Fat-free free-running coronary MRA at 1.5T using LIBRE water excitation pulses. In:

Proceedings of the ISMRM 27th Annual Meeting and Exhibition. Montréal, Canada; 2019:0459.

Heerfordt J, **Masala N**, Di Sopra L, Row CW, Milani B, Yerly J, Bastiaansen JAM, Piccini D, Stuber M. Respiratory Motion Signals Extracted from 3D Image-Based Navigation and from PCA of SI-Projections: Initial Findings in Whole-Heart Imaging using a Free-Running Framework. In: Proceedings of the ISMRM 27th Annual Meeting and Exhibition. Montréal, Canada; 2019:4474.

Roy CW, Yerly J, Bastiaansen JAM, **Masala** N, Di Sopra L, Wetzl J, Forman C, Piccini D, Stuber M. Cardiac and Respiratory Motion-Resolved 5D Imaging Using a Free-Running Framework: Comparison of Cartesian and Radial Trajectories. In: Proceedings of the ISMRM 27th Annual Meeting and Exhibition. Montréal, Canada; 2019:4751.

Rossi GMC, **Masala N**, Bastiaansen JAM, Bustin A, Heerfordt J, Piccini D, Stuber M, Roy CW. Focused navigation for free-running respiratory and cardiac motion-corrected 3D whole-heart coronary MRA. In: Proceedings of the Society for Cardiovascular Magnetic Resonance Virtual Scientific Sessions 2021. 2021.

Rossi GMC, **Masala N**, Bastiaansen JAM, Bustin A, Yerly J, Heerfordt J, Piccini D, Stuber M, Roy CW. Focused navigation (fNAV) for cardiac and respiratory motion-compensated free-running 3D whole-heart coronary MRA. In: Proceedings of the 2021 ISMRM & SMRT Annual Meeting & Exhibition. 2021:0188.

Awards

Magna Cum Laude Merit Award (top 15% of abstracts in major subject review category), awarded at the ISMRM 27th Annual Meeting and Exhibition in Montréal, Canada, for abstract 0459 above by the International Society for Magnetic Resonance in Medicine (ISMRM), 2019.

BIBLIOGRAPHY

1. Lustig M, Donoho D, Pauly JM. Sparse MRI: The application of compressed sensing for rapid MR imaging. *Magn Reson Med.* 2007;58(6):1182-1195. doi:10.1002/mrm.21391.

2. Benjamin EJ, Muntner P, Alonso A, et al. Heart Disease and Stroke Statistics—2019 Update: A Report From the American Heart Association. *Circulation.* 2019;135(10):e146-e603. doi:10.1161/CIR.0000000000000659.

3. Timmis A, Townsend N, Gale CP, et al. European society of cardiology: Cardiovascular disease statistics 2019. *Eur Heart J.* 2020;41(1):12-85. doi:10.1093/eurheartj/ehz859.

4. Stuber M, Weiss RG. Coronary magnetic resonance angiography. *J Magn Reson Imaging.* 2007;26(2):219-234. doi:10.1002/jmri.20949.

5. Dweck MR, Puntmann VO, Vesey AT, Fayad ZA, Nagel E. MR Imaging of Coronary Arteries and Plaques. *JACC Cardiovasc Imaging.* 2016;9(3):306-316. doi:10.1016/j.jcmg.2015.12.003.

6. Sakuma H. Coronary CT versus MR angiography: The role of MR angiography. *Radiology.* 2011;258(2):340-349. doi:10.1148/radiol.10100116.

7. Kim WY, Danias PG, Stuber M, et al. Coronary Magnetic Resonance Angiography for the Detection of Coronary Stenoses. *N Engl J Med.* 2001;345(26):1863-1869. doi:10.1056/NEJMoa010866.

8. Leiner T, Bogaert J, Friedrich MG, et al. *SCMR Position Paper (2020) on Clinical Indications for Cardiovascular Magnetic Resonance.* Vol 22. BioMed Central; 2020. doi:10.1186/s12968-020-00682-4.

9. Kramer CM, Barkhausen J, Flamm SD, Kim RJ, Nagel E. Standardized cardiovascular magnetic resonance (CMR) protocols 2013 update. *J Cardiovasc Magn Reson.* 2013;15(1):1-10. doi:10.1186/1532-429X-15-91.

10. Messroghli DR, Moon JC, Ferreira VM, et al. Clinical recommendations for cardiovascular magnetic resonance mapping of T1, T2, T2 and extracellular volume: A consensus statement by the Society for Cardiovascular Magnetic Resonance (SCMR) endorsed by the European Association for Cardiovascular Imagin. *J Cardiovasc Magn Reson.* 2017;19(1):1-24. doi:10.1186/s12968-017-0389-8.

11. Dall'Armellina E, Piechnik SK, Ferreira VM, et al. Cardiovascular magnetic resonance by

non contrast T1-mapping allows assessment of severity of injury in acute myocardial infarction. *J Cardiovasc Magn Reson.* 2012;14(1):1-13. doi:10.1186/1532-429X-14-15.

12. Ferreira VM, Piechnik SK, Dallarmellina E, et al. Non-contrast T1-mapping detects acute myocardial edema with high diagnostic accuracy: A comparison to T2-weighted cardiovascular magnetic resonance. *J Cardiovasc Magn Reson.* 2012;14(1):1-12. doi:10.1186/1532-429X-14-42.

13. Radunski UK, Lund GK, Stehning C, et al. CMR in patients with severe myocarditis: Diagnostic value of quantitative tissue markers including extracellular volume imaging. *JACC Cardiovasc Imaging.* 2014;7(7):667-675. doi:10.1016/j.jcmg.2014.02.005.

14. Friedrich MG, Chetrit M. The unique role of cardiovascular magnetic resonance imaging in acute myocarditis. *F1000Research.* 2018;7:1-7. doi:10.12688/f1000research.14857.1.

15. Karamitsos TD, Piechnik SK, Banypersad SM, et al. Noncontrast T1 mapping for the diagnosis of cardiac amyloidosis. *JACC Cardiovasc Imaging.* 2013;6(4):488-497. doi:10.1016/j.jcmg.2012.11.013.

16. Haaf P, Garg P, Messroghli DR, Broadbent DA, Greenwood JP, Plein S. Cardiac T1 Mapping and Extracellular Volume (ECV) in clinical practice: A comprehensive review. *J Cardiovasc Magn Reson.* 2016;18(1):1-12. doi:10.1186/s12968-016-0308-4.

17. Ramalho J, Semelka RC, Ramalho M, Nunes RH, AlObaidy M, Castillo M. Gadolinium-based contrast agent accumulation and toxicity: An update. *Am J Neuroradiol.* 2016;37(7):1192-1198. doi:10.3174/ajnr.A4615.

18. Thavendiranathan P, Walls M, Giri S, et al. Improved detection of myocardial involvement in acute inflammatory cardiomyopathies using T2 mapping. *Circ Cardiovasc Imaging.* 2012;5(1):102-110. doi:10.1161/CIRCIMAGING.111.967836.

19. Giri S, Chung Y-C, Merchant A, et al. T2 quantification for improved detection of myocardial edema. *J Cardiovasc Magn Reson.* 2009;11(1):56. doi:10.1186/1532-429X-11-56.

20. Verhaert D, Thavendiranathan P, Giri S, et al. Direct T2 quantification of myocardial edema in acute ischemic injury. *JACC Cardiovasc Imaging.* 2011;4(3):269-278. doi:10.1016/j.jcmg.2010.09.023.

21. Friedrich MG, Sechtem U, Schulz-Menger J, et al. Cardiovascular Magnetic Resonance in Myocarditis: A JACC White Paper. *J Am Coll Cardiol.* 2009;53(17):1475-1487. doi:10.1016/j.jacc.2009.02.007.

22. Cornicelli MD, Rigsby CK, Rychlik K, Pahl E, Robinson JD. Diagnostic performance of cardiovascular magnetic resonance native T1 and T2 mapping in pediatric patients with acute myocarditis. *J Cardiovasc Magn Reson.* 2019;21(1):1-9. doi:10.1186/s12968-019-0550-7.

23. Lurz P, Luecke C, Eitel I, et al. Comprehensive Cardiac Magnetic Resonance Imaging in Patients with Suspected Myocarditis the MyoRacer-Trial. *J Am Coll Cardiol.*

2016;67(15):1800-1811. doi:10.1016/j.jacc.2016.02.013.

24. Messroghli DR, Radjenovic A, Kozerke S, Higgins DM, Sivananthan MU, Ridgway JP. Modified Look-Locker inversion recovery (MOLLI) for high-resolutionT1 mapping of the heart. *Magn Reson Med.* 2004;52(1):141-146. doi:10.1002/mrm.20110.

25. Huang T-Y, Liu Y-J, Stemmer A, Poncelet BP. T2 measurement of the human myocardium using aT2-prepared transient-state trueFISP sequence. *Magn Reson Med.* 2007;57(5):960-966. doi:10.1002/mrm.21208.

26. Dabir D, Vollbrecht TM, Luetkens JA, et al. Multiparametric cardiovascular magnetic resonance imaging in acute myocarditis: A comparison of different measurement approaches. *J Cardiovasc Magn Reson.* 2019;21(1):1-11. doi:10.1186/s12968-019-0568-x.

27. Ugander M, Bagi PS, Oki AJ, et al. Myocardial edema as detected by pre-contrast T1 and T2 CMR delineates area at risk associated with acute myocardial infarction. *JACC Cardiovasc Imaging.* 2012;5(6):596-603. doi:10.1016/j.jcmg.2012.01.016.

28. Imran M, Wang L, McCrohon J, et al. Multiparametric mapping in the diagnosis and management of cardiac transplant rejection: A prospective, histologically-validated study. *J Cardiovasc Magn Reson.* 2016;18(Suppl 1):1-2. doi:10.1186/1532-429X-18-S1-O67.

29. Lauterbur PC. Image Formation by Induced Local Interactions: Examples Employing Nuclear Magnetic Resonance. *Nature.* 1973;242(5394):190-191. doi:10.1038/242190a0.

30. Edelman RR, Manning WJ, Burstein D, Paulin S. Coronary arteries: Breath-hold MR angiography. *Radiology.* 1991;181(3):641-643. doi:10.1148/radiology.181.3.1947074.

31. Marks B, Mitchell DG, Simelaro JP. Breath-holding in healthy and pulmonary-compromised populations: Effects of hyperventilation and oxygen inspiration. *J Magn Reson Imaging.* 1997;7(3):595-597. doi:10.1002/jmri.1880070323.

32. Larson AC, White RD, Laub G, McVeigh ER, Li D, Simonetti OP. Self-Gated Cardiac Cine MRI. *Magn Reson Med.* 2004;51(1):93-102. doi:10.1002/mrm.10664.

33. Ehman RL, Felmlee JP. Adaptive technique for high-definition MR imaging of moving structures. *Radiology.* 1989;173(1):255-263. doi:10.1148/radiology.173.1.2781017.

34. Wang Y, Rossman PJ, Grimm RC, Riederer SJ, Ehman RL. Navigator-echo-based real-time respiratory gating and triggering for reduction of respiration effects in three-dimensional coronary MR angiography. *Radiology.* 1996;198(1):55-60. doi:10.1148/radiology.198.1.8539406.

35. Li D, Kaushikkar S, Haacke EM, et al. Coronary Arteries: Three-dimensional MR Imaging with Retrospective Respiratory Gating. *Radiology.* 1996;201:857-863.

36. Sakuma H, Ichikawa Y, Chino S, Hirano T, Makino K, Takeda K. Detection of Coronary Artery Stenosis With Whole-Heart Coronary Magnetic Resonance Angiography. *J Am Coll Cardiol.* 2006;48(10):1946-1950. doi:10.1016/j.jacc.2006.07.055.

37. Piccini D, Littmann A, Nielles-Vallespin S, Zenge MO. Respiratory self-navigation for

whole-heart bright-blood coronary MRI: Methods for robust isolation and automatic segmentation of the blood pool. *Magn Reson Med.* 2012;68(2):571-579. doi:10.1002/mrm.23247.

38. Stuber M, Botnar RM, Danias PG, Kissinger K V., Manning WJ. Submillimeter Three-dimensional Coronary MR Angiography with Real-time Navigator Correction: Comparison of Navigator Locations. *Radiology.* 1999;212(2):579-587. doi:10.1148/radiology.212.2.r99au50579.

39. Taylor AM, Jhooti P, Firmin DN, Pennell DJ. Automated monitoring of diaphragm end-expiratory position for real-time navigator echo MR coronary angiography. *J Magn Reson Imaging.* 1999;9(3):395-401. doi:10.1002/(SICI)1522-2586(199903)9:3<395::AID-JMRI6>3.0.CO;2-Y.

40. Coppo S, Piccini D, Bonanno G, et al. Free-running 4D whole-heart self-navigated golden angle MRI: Initial results. *Magn Reson Med.* 2015;74(5):1306-1316. doi:10.1002/mrm.25523.

41. Weber OM, Martin AJ, Higgins CB. Whole-Heart Steady-State Free Precession Coronary Artery Magnetic Resonance Angiography. *Magn Reson Med.* 2003;50(6):1223-1228. doi:10.1002/mrm.10653.

42. Stuber M, Botnar RM, Danias PG, et al. Double-oblique free-breathing high resolution three-dimensional coronary magnetic resonance angiography. *J Am Coll Cardiol.* 1999;34(2):524-531. doi:10.1016/S0735-1097(99)00223-5.

43. Hardy CJ, Saranathan M, Zhu Y, Darrow RD. Coronary angiography by real-time MRI with adaptive averaging. *Magn Reson Med.* 2000;44(6):940-946. doi:10.1002/1522-2594(200012)44:6<940::AID-MRM16>3.0.CO;2-F.

44. Deshpande VS, Shea SM, Laub G, Simonetti OP, Finn JP, Li D. 3D magnetization-prepared true-FISP: A new technique for imaging coronary arteries. *Magn Reson Med.* 2001;46(3):494-502. doi:10.1002/mrm.1219.

45. Pruessmann KP, Weiger M, Scheidegger MB, Boesiger P. SENSE: Sensitivity encoding for fast MRI. *Magn Reson Med.* 1999;42(5):952-962. doi:10.1002/(sici)1522-2594(199911)42:5<952::aid-mrm16>3.3.co;2-j.

46. Kim WS, Mun CW, Kim DJ, Cho ZH. Extraction of cardiac and respiratory motion cycles by use of projection data and its applications to nmr imaging. *Magn Reson Med.* 1990;13(1):25-37. doi:10.1002/mrm.1910130105.

47. Stehning C, Börnert P, Nehrke K, Eggers H, Stuber M. Free-breathing whole-heart coronary MRA with 3D radial SSFP and self-navigated image reconstruction. *Magn Reson Med.* 2005;54(2):476-480. doi:10.1002/mrm.20557.

48. Piccini D, Littmann A, Nielles-Vallespin S, Zenge MO. Spiral phyllotaxis: The natural way to construct a 3D radial trajectory in MRI. *Magn Reson Med.* 2011;66(4):1049-1056. doi:10.1002/mrm.22898.

49. Pang J, Sharif B, Fan Z, et al. ECG and navigator-free four-dimensional whole-heart coronary MRA for simultaneous visualization of cardiac anatomy and function. *Magn Reson Med.* 2014;72(5):1208-1217. doi:10.1002/mrm.25450.

50. Feng L, Axel L, Chandarana H, Block KT, Sodickson DK, Otazo R. XD-GRASP: Golden-angle radial MRI with reconstruction of extra motion-state dimensions using compressed sensing. *Magn Reson Med.* 2016;75(2):775-788. doi:10.1002/mrm.25665.

51. Donoho DL. Compressed Sensing. *IEEE Trans Inf Theory.* 2006;52(4):1289-1306. doi:10.1109/TIT.2006.871582.

52. Piccini D, Feng L, Bonanno G, et al. Four-dimensional respiratory motion-resolved whole heart coronary MR angiography. *Magn Reson Med.* 2017;77(4):1473-1484. doi:10.1002/mrm.26221.

53. Feng L, Coppo S, Piccini D, et al. 5D whole-heart sparse MRI. *Magn Reson Med.* 2018;79(2):826-838. doi:10.1002/mrm.26745.

54. Di Sopra L, Piccini D, Coppo S, Stuber M, Yerly J. An automated approach to fully self-gated free-running cardiac and respiratory motion-resolved 5D whole-heart MRI. *Magn Reson Med.* 2019;82(6):2118-2132. doi:10.1002/mrm.27898.

55. Haase A, Frahm J, Hanicke W, Matthaei D. 1H NMR chemical shift selective (CHESS) imaging. *Phys Med Biol.* 1985;30(4):341-344. doi:10.1088/0031-9155/30/4/008.

56. Di Sopra L. FREE-RUNNING FRAMEWORK FOR AUTOMATED MULTIDIMENSIONAL AND COMPREHENSIVE MAGNETIC RESONANCE IMAGING OF THE HEART. 2020. https://serval.unil.ch/fr/notice/serval:BIB_359C8A20865C.

57. Bieri O, Scheffler K. Fundamentals of balanced steady state free precession MRI. *J Magn Reson Imaging.* 2013;38(1):2-11. doi:10.1002/jmri.24163.

58. Scheffler K, Lehnhardt S. Principles and applications of balanced SSFP techniques. *Eur Radiol.* 2003;13(11):2409-2418. doi:10.1007/s00330-003-1957-x.

59. Hargreaves B. Rapid gradient-echo imaging. *J Magn Reson Imaging.* 2012;36(6):1300-1313. doi:10.1002/jmri.23742.

60. Deshpande VS, Chung YC, Zhang Q, Shea SM, Li D. Reduction of transient signal oscillations in true-FISP using a linear flip angle series magnetization preparation. *Magn Reson Med.* 2003;49(1):151-157. doi:10.1002/mrm.10337.

61. Deimling M, Heid O. Magnetization Prepared True FISP Imaging. In: *Proc SMRM.* San Francisco, USA; 1994:495. http://cds.ismrm.org/ismrm-1999/PDF7/1882.pdf.

62. Bieri O. An analytical description of balanced steady-state free precession with finite radio-frequency excitation. *Magn Reson Med.* 2011;65(2):422-431. doi:10.1002/mrm.22626.

63. Bastiaansen JAM, Stuber M. Flexible water excitation for fat-free MRI at 3T using lipid insensitive binomial off-resonant RF excitation (LIBRE) pulses. *Magn Reson Med.* 2018;79(6):3007-3017. doi:10.1002/mrm.26965.

64. Shcherbakova Y, van den Berg CAT, Moonen CTW, Bartels LW. PLANET: An ellipse fitting approach for simultaneous T 1 and T 2 mapping using phase-cycled balanced steady-state free precession. *Magn Reson Med.* 2018;79(2):711-722. doi:10.1002/mrm.26717.

65. Bley TA, Wieben O, François CJ, Brittain JH, Reeder SB. Fat and water magnetic resonance imaging. *J Magn Reson Imaging.* 2010;31(1):4-18. doi:10.1002/jmri.21895.

66. Milotta G, Bustin A, Jaubert O, Neji R, Prieto C, Botnar RM. 3D whole-heart isotropic-resolution motion-compensated joint T1/T2 mapping and water/fat imaging. *Magn Reson Med.* 2020;84(6):3009-3026. doi:10.1002/mrm.28330.

67. Bydder GM, Young IR. Mr imaging: Clinical use of the inversion recovery sequence. *J Comput Assist Tomogr.* 1985;9(4):659-675. doi:10.1097/00004728-198507010-00002.

68. Zee CS, Segall HD, Terk MR, et al. SPIR MRI in Spinal Diseases. *J Comput Assist Tomogr.* 1992;16(3):356-360. doi:10.1097/00004728-199205000-00004.

69. Ginami G, Neji R, Phinikaridou A, Whitaker J, Botnar RM, Prieto C. Simultaneous bright- and black-blood whole-heart MRI for noncontrast enhanced coronary lumen and thrombus visualization. *Magn Reson Med.* 2018;79(3):1460-1472. doi:10.1002/mrm.26815.

70. Henningsson M, Koken P, Stehning C, Razavi R, Prieto C, Botnar RM. Whole-heart coronary MR angiography with 2D self-navigated image reconstruction. *Magn Reson Med.* 2012;67(2):437-445. doi:10.1002/mrm.23027.

71. Simonetti OP, Kim RJ, Fieno DS, et al. An Improved MR Imaging Technique for the Visualization of Myocardial Infarction. *Radiology.* 2001;218(1):215-223. doi:10.1148/radiology.218.1.r01ja50215.

72. Kim RJ, Wu E, Rafael A, et al. The Use of Contrast-Enhanced Magnetic Resonance Imaging to Identify Reversible Myocardial Dysfunction. *N Engl J Med.* 2000;343(20):1445-1453. doi:10.1056/NEJM200011163432003.

73. Kellman P, Arai AE, McVeigh ER, Aletras AH. Phase-sensitive inversion recovery for detecting myocardial infarction using gadolinium-delayed hyperenhancement. *Magn Reson Med.* 2002;47(2):372-383. doi:10.1002/mrm.10051.

74. Morris GA, Freeman R. Selective excitation in Fourier transform nuclear magnetic resonance. *J Magn Reson.* 1978;29(3):433-462. doi:10.1016/0022-2364(78)90003-3.

75. Scheffler K, Heid O, Hennig J. Magnetization preparation during the steady state: Fat-saturated 3D TrueFISP. *Magn Reson Med.* 2001;45(6):1075-1080. doi:10.1002/mrm.1142.

76. Derbyshire JA, Herzka DA, McVeigh ER. S5FP: Spectrally selective suppression with steady state free precession. *Magn Reson Med.* 2005;54(4):918-928. doi:10.1002/mrm.20633.

77. Meyer CH, Pauly JM, Macovskiand A, Nishimura DG. Simultaneous spatial and spectral selective excitation. *Magn Reson Med.* 1990;15(2):287-304. doi:10.1002/mrm.1910150211.

78. Hore PJ. Solvent suppression in fourier transform nuclear magnetic resonance. *J Magn Reson.* 1983;55(2):283-300. doi:10.1016/0022-2364(83)90240-8.

79. Schick F, Forster J, Machann J, Kuntz R, Claussen CD. Improved clinical echo-planar MRI using spatial-spectral excitation. *J Magn Reson Imaging.* 1998;8(4):960-967. doi:10.1002/jmri.1880080427.

80. Ye Y, Hu J, Haacke EM. Robust selective signal suppression using binomial off-resonant rectangular (BORR) pulses. *J Magn Reson Imaging.* 2014;39(1):195-202. doi:10.1002/jmri.24149.

81. Lee GR, Tkach JA, Griswold MA. Time-efficient slab-selective water excitation for 3D MRI. *Magn Reson Med.* 2012;67(1):127-136. doi:10.1002/mrm.22994.

82. Stirnberg R, Brenner D, Stöcker T, Shah NJ. Rapid fat suppression for three-dimensional echo planar imaging with minimized specific absorption rate. *Magn Reson Med.* 2016;76(5):1517-1523. doi:10.1002/mrm.26063.

83. Bastiaansen JAM, van Heeswijk RB, Stuber M, Piccini D. Noncontrast free-breathing respiratory self-navigated coronary artery cardiovascular magnetic resonance angiography at 3 T using lipid insensitive binomial off-resonant excitation (LIBRE). *J Cardiovasc Magn Reson.* 2019;21(1):38. doi:10.1186/s12968-019-0543-6.

84. Nayak KS, Cunningham CH, Santos JM, Pauly JM. Real-Time Cardiac MRI at 3 Tesla. *Magn Reson Med.* 2004;51(4):655-660. doi:10.1002/mrm.20053.

85. Börnert P, Stuber M, Botnar RM, Kissinger K V., Manning WJ. Comparison of fat suppression strategies in 3D spiral coronary magnetic resonance angiography. *J Magn Reson Imaging.* 2002;15(4):462-466. doi:10.1002/jmri.10078.

86. Quist B, Hargreaves BA, Cukur T, Morrell GR, Gold GE, Bangerter NK. Simultaneous fat suppression and band reduction with large-angle multiple-acquisition balanced steady-state free precession. *Magn Reson Med.* 2012;67(4):1004-1012. doi:10.1002/mrm.23076.

87. Leupold J, Hennig J, Scheffler K. Alternating repetition time balanced steady state free precession. *Magn Reson Med.* 2006;55(3):557-565. doi:10.1002/mrm.20790.

88. Çukur T, Nishimura DG. Fat-water separation with alternating repetition time balanced SSFP. *Magn Reson Med.* 2008;60(2):479-484. doi:10.1002/mrm.21692.

89. Absil J, Denolin V, Metens T. Fat attenuation using a dual steady-state balanced-SSFP sequence with periodically variable flip angles. *Magn Reson Med.* 2006;55(2):343-351. doi:10.1002/mrm.20766.

90. Hennig J, Speck O, Scheffler K. Optimization of signal behavior in the transition to driven equilibrium in steady-state free precession sequences. *Magn Reson Med.* 2002;48(5):801-809. doi:10.1002/mrm.10274.

91. Paul D, Hennig J, Zaitsev M. Intrinsic fat suppression in TIDE balanced steady-state free precession imaging. *Magn Reson Med.* 2006;56(6):1328-1335. doi:10.1002/mrm.21084.

92. Çukur T. Spectrally selective imaging with wideband balanced steady-state free precession MRI. *Magn Reson Med.* 2016;75(3):1132-1141. doi:10.1002/mrm.25700.

93. Koktzoglou I, Edelman RR. Radial fast interrupted steady-state (FISS) magnetic resonance imaging. *Magn Reson Med.* 2018;79(4):2077-2086. doi:10.1002/mrm.26881.

94. Bastiaansen JAM, Piccini D, Di Sopra L, et al. Natively fat-suppressed 5D whole-heart MRI with a radial free-running fast-interrupted steady-state (FISS) sequence at 1.5T and 3T. *Magn Reson Med.* 2020;83(1):45-55. doi:10.1002/mrm.27942.

95. Küstner T, Bustin A, Jaubert O, Neji R, Prieto C, Botnar R. 3D Cartesian fast interrupted steady-state (FISS) imaging. *Magn Reson Med.* 2019;82(5):1617-1630. doi:10.1002/mrm.27830.

96. Dixon, Thomas W. Simple Proton Spectroscopic Imaging. *Radiology.* 1984;153:189-194. http://mriquestions.com/uploads/3/4/5/7/34572113/dixon_method_1984_radiology.pdf.

97. Glover GH, Schneider E. Three-point dixon technique for true water/fat decomposition with B0 inhomogeneity correction. *Magn Reson Med.* 1991;18(2):371-383. doi:10.1002/mrm.1910180211.

98. Ma J. Dixon techniques for water and fat imaging. *J Magn Reson Imaging.* 2008;28(3):543-558. doi:10.1002/jmri.21492.

99. Reeder SB, Pineda AR, Wen Z, et al. Iterative decomposition of water and fat with echo asymmetry and least-squares estimation (IDEAL): Application with fast spin-echo imaging. *Magn Reson Med.* 2005;54(3):636-644. doi:10.1002/mrm.20624.

100. Yu H, Shimakawa A, McKenzie CA, Brodsky E, Brittain JH, Reeder SB. Multiecho water-fat separation and simultaneous R 2* estimation with multifrequency fat spectrum modeling. *Magn Reson Med.* 2008;60(5):1122-1134. doi:10.1002/mrm.21737.

101. Huang TY, Chung HW, Wang FN, Ko CW, Chen CY. Fat and Water Separation in Balanced Steady-State Free Precession Using the Dixon Method. *Magn Reson Med.* 2004;51(2):243-247. doi:10.1002/mrm.10686.

102. Quist B, Hargreaves BA, Daniel BL, Saranathan M. Balanced SSFP Dixon imaging with banding-artifact reduction at 3 Tesla. *Magn Reson Med.* 2015;74(3):706-715. doi:10.1002/mrm.25449.

103. Gold GE, Reeder SB, Yu H, et al. Articular Cartilage of the Knee: Rapid Three-dimensional MR Imaging at 3.0 T with IDEAL Balanced Steady-State Free Precession—Initial Experience. *Radiology.* 2006;240(2):546-551. doi:10.1148/radiol.2402050288.

104. Hargreaves BA, Vasanawala SS, Nayak KS, Hu BS, Nishimura DG. Fat-suppressed steady-state free precession imaging using phase detection. *Magn Reson Med.* 2003;50(1):210-213. doi:10.1002/mrm.10488.

105. Hargreaves BA, Bangerter NK, Shimakawa A, Vasanawala SS, Brittain JH, Nishimura DG. Dual-acquisition phase-sensitive fat-water separation using balanced steady-state

free precession. *Magn Reson Imaging*. 2006;24(2):113-122. doi:10.1016/j.mri.2005.10.013.

106. Vasanawala SS, Pauly JM, Nishimura DG. Fluctuating equilibrium MRI. *Magn Reson Med*. 1999;42(5):876-883. doi:10.1002/(SICI)1522-2594(199911)42:5<876::AID-MRM6>3.0.CO;2-Z.

107. Vasanawala SS, Pauly JM, Nishimura DG. Linear combination steady-state free precession MRI. *Magn Reson Med*. 2000;43(1):82-90. doi:10.1002/(SICI)1522-2594(200001)43:1<82::AID-MRM10>3.0.CO;2-9.

108. Börnert P, Koken P, Nehrke K, Eggers H, Ostendorf P. Water/fat-resolved whole-heart Dixon coronary MRA: An initial comparison. *Magn Reson Med*. 2014;71(1):156-163. doi:10.1002/mrm.24648.

109. Kourtidou S, Jones MR, Moore RA, et al. MDixon ECG-gated 3-dimensional cardiovascular magnetic resonance angiography in patients with congenital cardiovascular disease. *J Cardiovasc Magn Reson*. 2019;21(1):1-13. doi:10.1186/s12968-019-0554-3.

110. Munoz C, Cruz G, Neji R, Botnar RM, Prieto C. Motion corrected water/fat whole-heart coronary MR angiography with 100% respiratory efficiency. *Magn Reson Med*. 2019;82(2):732-742. doi:10.1002/mrm.27732.

111. Munoz C, Bustin A, Neji R, et al. Motion-corrected 3D whole-heart water-fat high-resolution late gadolinium enhancement cardiovascular magnetic resonance imaging. *J Cardiovasc Magn Reson*. 2020;22(1):1-13. doi:10.1186/s12968-020-00649-5.

112. Lai P, Larson AC, Park J, Carr JC, Li D. Respiratory self-gated four-dimensional coronary MR angiography: A feasibility study. *Magn Reson Med*. 2008;59(6):1378-1385. doi:10.1002/mrm.21617.

113. Park J, Larson AC, Zhang Q, Simonetti O, Li D. 4D radial coronary artery imaging within a single breath-hold: Cine angiography with phase-sensitive fat suppression (CAPS). *Magn Reson Med*. 2005;54(4):833-840. doi:10.1002/mrm.20627.

114. Scheffler K, Hennig J. Frequency resolved single-shot MR imaging using stochastic k-space trajectories. *Magn Reson Med*. 1996;35(4):569-576. doi:10.1002/mrm.1910350417.

115. Noll DC. Multishot rosette trajectories for spectrally selective mr imaging. *IEEE Trans Med Imaging*. 1997;16(4):372-377. doi:10.1109/42.611345.

116. Bucholz EK, Song J, Johnson GA, Hancu I. Multispectral imaging with three-dimensional rosette trajectories. *Magn Reson Med*. 2008;59(3):581-589. doi:10.1002/mrm.21551.

117. Liu Y, Hamilton J, Eck B, Griswold M, Seiberlich N. Myocardial T1 and T2 quantification and water–fat separation using cardiac MR fingerprinting with rosette trajectories at 3T and 1.5T. *Magn Reson Med*. 2021;85(1):103-119. doi:10.1002/mrm.28404.

118. Masala N, Bastiaansen JAM, Piccini D, Stuber M. Fat suppression in 3D bSSFP coronary MRA using lipid-insensitive binomial off-resonant RF excitation (LIBRE) pulses. In:

Proceedings of the Society for Cardiovascular Magnetic Resonance 22nd Annual Scientific Sessions. Bellevue, USA; 2019:QF2-006.

119. Hargreaves B. Bloch Equation Simulation. http://mrsrl.stanford.edu/~brian/bloch/. Accessed June 30, 2017.

120. Masala N, Bastiaansen JAM, Di Sopra L, et al. Free-running 5D coronary MR angiography at 1.5T using LIBRE water excitation pulses. *Magn Reson Med.* 2020;84(3):1470-1485. doi:10.1002/mrm.28221.

121. Atkinson D, Hill DLG, Stoyle PNR, Summers PE, Keevil SF. Automatic correction of motion artifacts in magnetic resonance images using an entropy focus criterion. *IEEE Trans Med Imaging.* 1997;16(6):903-910. doi:10.1109/42.650886.

122. Roy CW, Heerfordt J, Piccini D, et al. Motion Compensated Coronary MRA using Focused Navigation (fNAV). In: *Proceedings of the 2020 ISMRM & SMRT Virtual Conference & Exhibition.* ; 2020:1321.

123. Roy CW, Heerfordt J, Piccini D, et al. Motion compensated whole-heart coronary cardiovascular magnetic resonance angiography using focused navigation (fNAV). *J Cardiovasc Magn Reson.* 2021;23(1):1-17. doi:10.1186/s12968-021-00717-4.

124. Vahle T, Bacher M, Rigie D, et al. Respiratory Motion Detection and Correction for MR Using the Pilot Tone: Applications for MR and Simultaneous PET/MR Examinations. *Invest Radiol.* 2020;55(3):153-159. doi:10.1097/RLI.0000000000000619.

125. Küstner T, Fuin N, Hammernik K, et al. CINENet: deep learning-based 3D cardiac CINE MRI reconstruction with multi-coil complex-valued 4D spatio-temporal convolutions. *Sci Rep.* 2020;10(1):1-13. doi:10.1038/s41598-020-70551-8.

126. Heerfordt J, Whitehead KK, Bastiaansen JAM, et al. Similarity-driven multi-dimensional binning algorithm (SIMBA) for free-running motion-suppressed whole-heart MRA. *Magn Reson Med.* 2021;86(1):213-229. doi:10.1002/mrm.28713.

127. Kennedy J, Eberhart R. Particle swarm optimization. In: *Proceedings of ICNN'95 - International Conference on Neural Networks.* Vol 4. Perth, WA, Australia: IEEE; 1995:1942-1948. doi:10.1109/ICNN.1995.488968.

128. Arn L, Heeswijk RB Van, Coristine AJ, Stuber M, Bastiaansen JAM. Particle swarm optimization (PSO) and comparison of a water selective T2 preparation module for simultaneous robust fat suppression and tissue contrast enhancement at 3T. In: *Proceedings of the Joint Annual Meeting ISMRM-ESMRMB.* Paris, France: ISMRM; 2018:3346.

129. Di Sopra L, Roy CW, Bastiaansen JAM, et al. Fully Self-Gated Cardiac and Respiratory Motion-Resolved Isotropic 5D T1 Mapping of the Heart: Preliminary Results. In: *Proceedings of the ISMRM 27th Annual Meeting and Exhibition.* Montreal, Canada; 2019:0785.

130. Henze Bancroft LC, Strigel RM, Hernando D, et al. Utilization of a balanced steady state free precession signal model for improved fat/water decomposition. *Magn Reson Med.* 2016;75(3):1269-1277. doi:10.1002/mrm.25728.

131. Simonetti OP, Ahmad R. Low-Field Cardiac Magnetic Resonance Imaging: A Compelling Case for Cardiac Magnetic Resonance's Future. *Circ Cardiovasc Imaging.* 2017;10(6):1-8. doi:10.1161/CIRCIMAGING.117.005446.

132. Wetzl J, Lugauer F, Schmidt M, Maier A, Hornegger J, Forman C. Free-Breathing, Self-Navigated Isotropic 3-D CINE Imaging of the Whole Heart Using Cartesian Sampling. In: *Proceedings of the ISMRM 24th Annual Meeting & Exhibition.* ; 2016:411.

133. Roy CW, Yerly J, Bastiaansen JAM, et al. Cardiac and Respiratory Motion-Resolved 5D Imaging Using a Free-Running Framework: Comparison of Cartesian and Radial Trajectories. In: *Proceedings of the ISMRM 27th Annual Meeting and Exhibition.* Montréal, Canada; 2019:4751.

134. Bernstein MA, King KF, Zhou XJ. *Handbook of MRI Pulse Sequences.* Burlington, MA, USA: Elsevier Academic Press; 2004. doi:10.1016/B978-0-12-092861-3.X5000-6.

135. Hilbert T, Schulz J, Marques JP, et al. Fast model-based T2 mapping using SAR-reduced simultaneous multislice excitation. *Magn Reson Med.* 2019;82(6):2090-2103. doi:10.1002/mrm.27890.

136. Look DC, Locker DR. Time saving in measurement of NMR and EPR relaxation times. *Rev Sci Instrum.* 1970;41(2):250-251. doi:10.1063/1.1684482.

137. Haacke EM, Brown RW, Thompson MR, Venkatesan R. *Magnetic Resonance Imaging: Physical Principles and Sequence Design.* First Edit. New York, USA: John Wiley & Sons, Inc.; 1999.

138. Taylor AJ, Salerno M, Dharmakumar R, Jerosch-Herold M. T1 Mapping Basic Techniques and Clinical Applications. *JACC Cardiovasc Imaging.* 2016;9(1):67-81. doi:10.1016/j.jcmg.2015.11.005.

139. Wiesmueller M, Wuest W, Heiss R, Treutlein C, Uder M, May MS. Cardiac T2 mapping: Robustness and homogeneity of standardized in-line analysis. *J Cardiovasc Magn Reson.* 2020;22(1):1-10. doi:10.1186/s12968-020-00619-x.

140. Chandler AG, Pinder RJ, Netsch T, et al. Correction of misaligned slices in multi-slice cardiovascular magnetic resonance using slice-to-volume registration. *J Cardiovasc Magn Reson.* 2008;10(1):1-9. doi:10.1186/1532-429X-10-13.

141. Warntjes JBM, Dahlqvist Leinhard O, West J, Lundberg P. Rapid magnetic resonance quantification on the brain: Optimization for clinical usage. *Magn Reson Med.* 2008;60(2):320-329. doi:10.1002/mrm.21635.

142. Sbrizzi A, Heide O van der, Cloos M, et al. Fast quantitative MRI as a nonlinear tomography problem. *Magn Reson Imaging.* 2018;46(June 2017):56-63.

doi:10.1016/j.mri.2017.10.015.

143. Schmitt P, Griswold MA, Jakob PM, et al. Inversion Recovery TrueFISP: Quantification of T1, T 2, and Spin Density. *Magn Reson Med.* 2004;51(4):661-667. doi:10.1002/mrm.20058.

144. Ehses P, Seiberlich N, Ma D, et al. IR TrueFISP with a golden-ratio-based radial readout: Fast quantification of T1, T2, and proton density. *Magn Reson Med.* 2013;69(1):71-81. doi:10.1002/mrm.24225.

145. Ma D, Gulani V, Seiberlich N, et al. Magnetic resonance fingerprinting. *Nature.* 2013;495(7440):187-192. doi:10.1038/nature11971.

146. Lima da Cruz G, Bustin A, Jaubert O, Schneider T, Botnar RM, Prieto C. Sparsity and locally low rank regularization for MR fingerprinting. *Magn Reson Med.* 2019;81(6):3530-3543. doi:10.1002/mrm.27665.

147. Cauley SF, Setsompop K, Ma D, et al. Fast group matching for MR fingerprinting reconstruction. *Magn Reson Med.* 2015;74(2):523-528. doi:10.1002/mrm.25439.

148. Buonincontri G, Sawiak SJ. MR fingerprinting with simultaneous B1 estimation. *Magn Reson Med.* 2016;76(4):1127-1135. doi:10.1002/mrm.26009.

149. Jiang Y, Ma D, Bhat H, et al. Use of pattern recognition for unaliasing simultaneously acquired slices in simultaneous multislice MR fingerprinting. *Magn Reson Med.* 2017;78(5):1870-1876. doi:10.1002/mrm.26572.

150. Leroi L, Gras V, Boulant N, et al. Simultaneous proton density, T1, T2, and flip-angle mapping of the brain at 7 T using multiparametric 3D SSFP imaging and parallel-transmission universal pulses. *Magn Reson Med.* 2020;84(6):3286-3299. doi:10.1002/mrm.28391.

151. van der Heide O, Sbrizzi A, Luijten PR, van den Berg CAT. High-resolution in vivo MR-STAT using a matrix-free and parallelized reconstruction algorithm. *NMR Biomed.* 2020;33(4):1-16. doi:10.1002/nbm.4251.

152. Gómez PA, Cencini M, Golbabaee M, et al. Rapid three-dimensional multiparametric MRI with quantitative transient-state imaging. *Sci Rep.* 2020;10(1):1-17. doi:10.1038/s41598-020-70789-2.

153. Nguyen D, Bieri O. Motion-insensitive rapid configuration relaxometry. *Magn Reson Med.* 2017;78(2):518-526. doi:10.1002/mrm.26384.

154. Heule R, Ganter C, Bieri O. Triple echo steady-state (TESS) relaxometry. *Magn Reson Med.* 2014;71(1):230-237. doi:10.1002/mrm.24659.

155. Heule R, Bause J, Pusterla O, Scheffler K. Multi-parametric artificial neural network fitting of phase-cycled balanced steady-state free precession data. *Magn Reson Med.* 2020;84(6):2981-2993. doi:10.1002/mrm.28325.

156. Hilbert T, Nguyen D, Thiran JP, Krueger G, Kober T, Bieri O. True constructive

interference in the steady state (trueCISS). *Magn Reson Med.* 2018;79(4):1901-1910. doi:10.1002/mrm.26836.

157. Xiang QS, Hoff MN. Banding artifact removal for bSSFP imaging with an elliptical signal model. *Magn Reson Med.* 2014;71(3):927-933. doi:10.1002/mrm.25098.

158. Fitzgibbon AW, Pilu M, Fisher RB. Direct least squares fitting of ellipses. *Proc - Int Conf Pattern Recognit.* 1996;1(5):253-257. doi:10.1109/ICPR.1996.546029.

159. Shcherbakova Y, van den Berg CAT, Moonen CTW, Bartels LW. Investigation of the influence of B0 drift on the performance of the PLANET method and an algorithm for drift correction. *Magn Reson Med.* 2019;82(5):1725-1740. doi:10.1002/mrm.27860.

160. Gras V, Farrher E, Grinberg F, Shah NJ. Diffusion-weighted DESS protocol optimization for simultaneous mapping of the mean diffusivity, proton density and relaxation times at 3 Tesla. *Magn Reson Med.* 2017;78(1):130-141. doi:10.1002/mrm.26353.

161. Cheng CC, Preiswerk F, Hoge WS, Kuo TH, Madore B. Multipathway multi-echo (MPME) imaging: all main MR parameters mapped based on a single 3D scan. *Magn Reson Med.* 2019;81(3):1699-1713. doi:10.1002/mrm.27525.

162. de Rochefort L. Encoding with Radiofrequency Spoiling, Equilibrium States and Inverse Problem for Parametric Mapping. In: *Proceedings of the ISMRM 23rd Annual Meeting & Exhibition.* Toronto, Canada; 2015:0445. https://archive.ismrm.org/2015/0445.html.

163. Stöcker T, Keil F, Vahedipour K, Brenner D, Pracht E, Shah NJ. MR parameter quantification with magnetization-prepared double echo steady-state (MP-DESS). *Magn Reson Med.* 2014;72(1):103-111. doi:10.1002/mrm.24901.

164. Zhang Y, Wells SA, Hernando D. Stimulated echo based mapping (STEM) of T1, T2, and apparent diffusion coefficient: validation and protocol optimization. *Magn Reson Med.* 2019;81(1):167-181. doi:10.1002/mrm.27358.

165. Blume U, Lockie T, Stehning C, et al. Interleaved T 1 and T 2 relaxation time mapping for cardiac applications. *J Magn Reson Imaging.* 2009;29(2):480-487. doi:10.1002/jmri.21652.

166. Shao J, Zhou Z, Nguyen KL, Finn JP, Hu P. Accurate, precise, simultaneous myocardial T1 and T2 mapping using a radial sequence with inversion recovery and T2 preparation. *NMR Biomed.* 2019;32(11):1-12. doi:10.1002/nbm.4165.

167. Shao J, Ghodrati V, Nguyen KL, Hu P. Fast and accurate calculation of myocardial T1 and T2 values using deep learning Bloch equation simulations (DeepBLESS). *Magn Reson Med.* 2020;84(5):2831-2845. doi:10.1002/mrm.28321.

168. Kvernby S, Warntjes MJB, Haraldsson H, Carlhäll C-J, Engvall J, Ebbers T. Simultaneous three-dimensional myocardial T1 and T2 mapping in one breath hold with 3D-QALAS. *J Cardiovasc Magn Reson.* 2014;16(1):102. doi:10.1186/s12968-014-0102-0.

169. Qi H, Bustin A, Cruz G, et al. Free-running simultaneous myocardial T1/T2 mapping and

cine imaging with 3D whole-heart coverage and isotropic spatial resolution. *Magn Reson Imaging*. 2019;63(July):159-169. doi:10.1016/j.mri.2019.08.008.

170. Bustin A, Lima da Cruz G, Jaubert O, Lopez K, Botnar RM, Prieto C. High-dimensionality undersampled patch-based reconstruction (HD-PROST) for accelerated multi-contrast MRI. *Magn Reson Med*. 2019;81(6):3705-3719. doi:10.1002/mrm.27694.

171. Santini F, Kawel-Boehm N, Greiser A, Bremerich J, Bieri O. Simultaneous T 1 and T 2 quantification of the myocardium using cardiac balanced-SSFP inversion recovery with interleaved sampling acquisition (CABIRIA). *Magn Reson Med*. 2015;74(2):365-371. doi:10.1002/mrm.25402.

172. Akçakaya M, Weingärtner S, Basha TA, Roujol S, Bellm S, Nezafat R. Joint myocardial T 1 and T 2 mapping using a combination of saturation recovery and T 2 -preparation. *Magn Reson Med*. 2016;76(3):888-896. doi:10.1002/mrm.25975.

173. Guo R, Chen Z, Herzka DA, Luo J, Ding H. A three-dimensional free-breathing sequence for simultaneous myocardial T1 and T2 mapping. *Magn Reson Med*. 2019;81(2):1031-1043. doi:10.1002/mrm.27466.

174. Kvernby S, Warntjes M, Engvall J, Carlhäll CJ, Ebbers T. Clinical feasibility of 3D-QALAS – Single breath-hold 3D myocardial T1- and T2-mapping. *Magn Reson Imaging*. 2017;38:13-20. doi:10.1016/j.mri.2016.12.014.

175. Hamilton JI, Jiang Y, Chen Y, et al. MR fingerprinting for rapid quantification of myocardial T 1 , T 2 , and proton spin density. *Magn Reson Med*. 2017;77(4):1446-1458. doi:10.1002/mrm.26216.

176. Hamilton JI, Pahwa S, Adedigba J, et al. Simultaneous Mapping of T1 and T2 Using Cardiac Magnetic Resonance Fingerprinting in a Cohort of Healthy Subjects at 1.5T. *J Magn Reson Imaging*. 2020;52(4):1044-1052. doi:10.1002/jmri.27155.

177. Hamilton JI, Jiang Y, Ma D, et al. Simultaneous multislice cardiac magnetic resonance fingerprinting using low rank reconstruction. *NMR Biomed*. 2019;32(2):e4041. doi:10.1002/nbm.4041.

178. Hamilton JI, Jiang Y, Eck B, Griswold M, Seiberlich N. Cardiac cine magnetic resonance fingerprinting for combined ejection fraction, T1 and T2 quantification. *NMR Biomed*. 2020;33(8):1-17. doi:10.1002/nbm.4323.

179. Jaubert O, Cruz G, Bustin A, et al. Free-running cardiac magnetic resonance fingerprinting: Joint T1/T2 map and Cine imaging. *Magn Reson Imaging*. 2020;68(January):173-182. doi:10.1016/j.mri.2020.02.005.

180. Cruz G, Jaubert O, Qi H, et al. 3D free-breathing cardiac magnetic resonance fingerprinting. *NMR Biomed*. 2020;33(10):1-16. doi:10.1002/nbm.4370.

181. Jaubert O, Cruz G, Bustin A, et al. Water–fat Dixon cardiac magnetic resonance fingerprinting. *Magn Reson Med*. 2020;83(6):2107-2123. doi:10.1002/mrm.28070.

182. Jaubert O, Cruz G, Bustin A, et al. T1, T2, and Fat Fraction Cardiac MR Fingerprinting: Preliminary Clinical Evaluation. *J Magn Reson Imaging.* 2021;53(4):1253-1265. doi:10.1002/jmri.27415.

183. Dey D, Nakazato R, Li D, Berman DS. Epicardial and thoracic fat - Noninvasive measurement and clinical implications. *Cardiovasc Diagn Ther.* 2012;2(2):85-93. doi:10.3978/j.issn.2223-3652.2012.04.03.

184. Christodoulou AG, Shaw JL, Nguyen C, et al. Magnetic resonance multitasking for motion-resolved quantitative cardiovascular imaging. *Nat Biomed Eng.* 2018;2(4):215-226. doi:10.1038/s41551-018-0217-y.

185. Ma S, Nguyen CT, Han F, et al. Three-dimensional simultaneous brain T1, T2, and ADC mapping with MR Multitasking. *Magn Reson Med.* 2020;84(1):72-88. doi:10.1002/mrm.28092.

186. Shaw JL, Yang Q, Zhou Z, et al. Free-breathing, non-ECG, continuous myocardial T 1 mapping with cardiovascular magnetic resonance multitasking. *Magn Reson Med.* 2019;81(4):2450-2463. doi:10.1002/mrm.27574.

187. Yerly J, Di Sopra L, Vincenti G, Piccini D, Schwitter J, Stuber M. Fully Self-Gated Cardiac and Respiratory Motion-Resolved 5D MRI for Rapid Assessment of Left Ventricular Function. In: *Proceedings of the ISMRM 27th Annual Meeting and Exhibition*. Montréal, Canada; 2019:2106.

188. Boyd S, Parikh N, Chu E, Peleato B, Eckstein J. Distributed optimization and statistical learning via the alternating direction method of multipliers. *Found Trends Mach Learn.* 2010;3(1):1-122. doi:10.1561/2200000016.

189. Halir R, Flusser J. Numerically Stable Direct Least Squares Fitting Of Ellipses. 1998.

190. Keskin K, Çukur T. Constrained ellipse fitting for efficient T1-T2 mapping in phase-cycled bSSFP imaging. In: *Proceedings of the ISMRM 27th Annual Meeting and Exhibition*. Montréal, Canada; 2019:4533.

191. Shcherbakova Y, van den Berg CAT, Gavazzi S, Moonen CTW, Bartels LW. Detecting the presence of fat using PLANET-based parameter mapping. In: *Proceedings of the ISMRM 27th Annual Meeting and Exhibition*. Montréal, Canada; 2019:4015.

192. Shcherbakova Y, van den Berg CAT, Moonen CTW, Bartels LW. On the accuracy and precision of PLANET for multiparametric MRI using phase-cycled bSSFP imaging. *Magn Reson Med.* 2019;81(3):1534-1552. doi:10.1002/mrm.27491.

193. Gavazzi S, Shcherbakova Y, Bartels LW, et al. Transceive phase mapping using the PLANET method and its application for conductivity mapping in the brain. *Magn Reson Med.* 2020;83(2):590-607. doi:10.1002/mrm.27958.

194. Iyyakkunnel S, Schäper J, Bieri O. Configuration-based electrical properties tomography. *Magn Reson Med.* 2021;85(4):1855-1864. doi:10.1002/mrm.28542.

195. Wetzl J, Schmidt M, Pontana F, et al. Single-breath-hold 3-D CINE imaging of the left ventricle using Cartesian sampling. *Magn Reson Mater Physics, Biol Med.* 2018;31(1):19-31. doi:10.1007/s10334-017-0624-1.

196. Walsh DO, Gmitro AF, Marcellin MW. Adaptive reconstruction of phased array MR imagery. *Magn Reson Med.* 2000;43(5):682-690. doi:10.1002/(SICI)1522-2594(200005)43:5<682::AID-MRM10>3.0.CO;2-G.

197. Zur Y, Wood ML, Neuringer LJ. Motion-insensitive, steady-state free precession imaging. *Magn Reson Med.* 1990;16(3):444-459. doi:10.1002/mrm.1910160311.

198. Kellner E, Dhital B, Kiselev VG, Reisert M. Gibbs-ringing artifact removal based on local subvoxel-shifts. *Magn Reson Med.* 2016;76(5):1574-1581. doi:10.1002/mrm.26054.

199. Ashburner J, Friston KJ. Unified segmentation. *Neuroimage.* 2005;26(3):839-851. doi:10.1016/j.neuroimage.2005.02.018.

200. Björk M, Ingle RR, Gudmundson E, Stoica P, Nishimura DG, Barral JK. Parameter estimation approach to banding artifact reduction in balanced steady-state free precession. *Magn Reson Med.* 2014;72(3):880-892. doi:10.1002/mrm.24986.

201. Feng L, Chandarana H, Sodickson DK, Otazo R. Unstreaking: radial MRI with automatic streaking artifact reduction. In: *Proceedings of the ISMRM 25th Annual Meeting of ISMRM.* Honolulu, USA; 2017:4001.

202. Biyik E, Ilicak E, Çukur T. Reconstruction by calibration over tensors for multi-coil multi-acquisition balanced SSFP imaging. *Magn Reson Med.* 2018;79(5):2542-2554. doi:10.1002/mrm.26902.

203. Chen C, Liu Y, Schniter P, et al. Sparsity adaptive reconstruction for highly accelerated cardiac MRI. *Magn Reson Med.* 2019;81(6):3875-3887. doi:10.1002/mrm.27671.

204. Forman C, Piccini D, Grimm R, Hutter J, Hornegger J, Zenge MO. High-resolution 3D whole-heart coronary MRA: a study on the combination of data acquisition in multiple breath-holds and 1D residual respiratory motion compensation. *Magn Reson Mater Physics, Biol Med.* 2014;27(5):435-443. doi:10.1007/s10334-013-0428-x.

205. Cukur T. Accelerated Phase-Cycled SSFP Imaging. *IEEE Trans Med Imaging.* 2015;34(1):107-115.

206. Kay SM. *Fundamentals of Statistical Processing, Volume I: Estimation Theory.* Englewood Cliffs, NJ, USA: Prentice-Hall; 1993.

207. Miller KL. Asymmetries of the balanced SSFP profile. Part I: Theory and observation. *Magn Reson Med.* 2010;63(2):385-395. doi:10.1002/mrm.22212.

208. Bieri O, Markl M, Scheffler K. Analysis and compensation of eddy currents in balanced SSFP. *Magn Reson Med.* 2005;54(1):129-137. doi:10.1002/mrm.20527.

APPENDIX

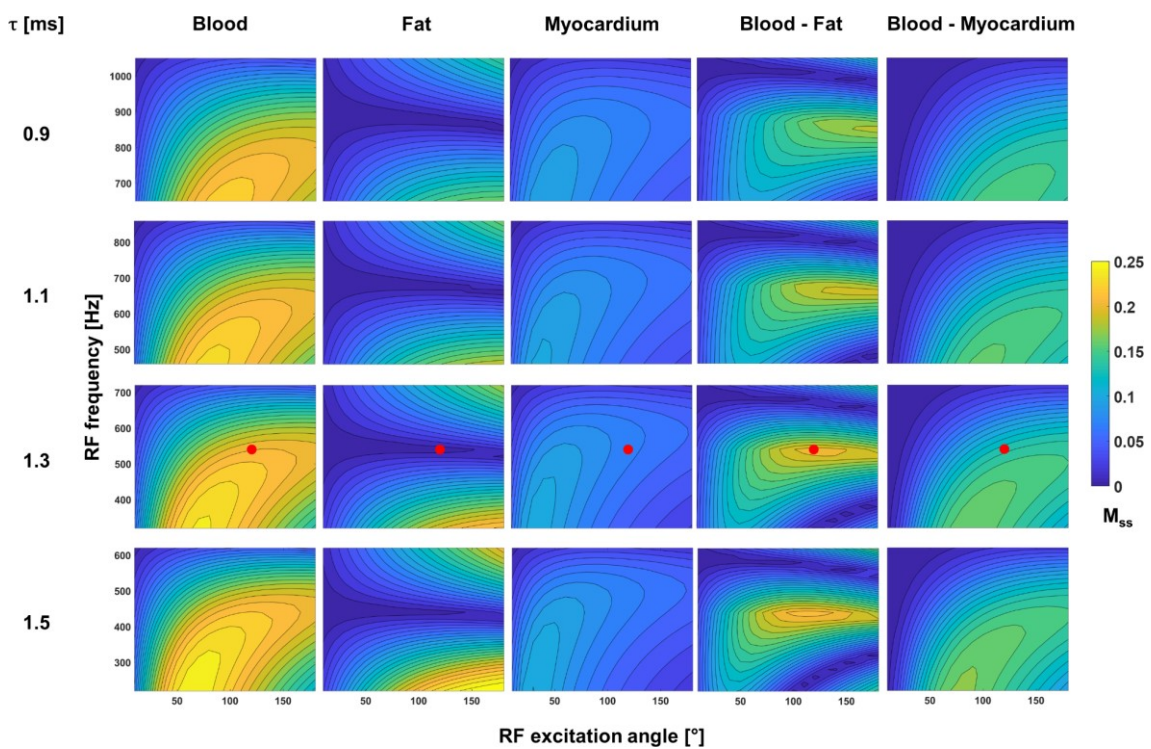*A1. LIBRE numerical optimization using single-peak fat model*

Figure 16. Theoretical LIBRE signal behavior using a single-peak fat model. Transverse steady-state magnetization (M_{ss}), as a function of RF excitation angle and frequency (relative to the Larmor frequency) for different sub-pulse durations (τ) of the LIBRE pulse, for blood, fat, myocardium, blood–fat contrast, and blood–myocardium contrast. The red dot indicates the chosen optimal parameters that maximize the blood–fat contrast.

A2. Reproduction of published PLANET work

We had assumed that PLANET would work "out of the box," so we performed phase-cycled bSSFP acquisitions in mid-2019 using desired parameters with a view of quickly moving towards free-running 5D myocardial mapping. Unfortunately, the map accuracy and homogeneity did not match that of the published results (64), and there

127

were "holes" in the maps due to negative relaxation times, which then led to a phase of attempting to reproduce the published results that lasted until September 2020.

It was initially determined that the calculation of the coil sensitivities was very important. In 2019, we found that an appropriate coil combination was needed, namely the adaptive reconstruction technique described in (196) that according to online forums for Siemens IDEA was similar to what was done at the scanner. We found in early 2020 that the same coil sensitivity map needs to be used for reconstruction of all the phase-cycled images for a given PLANET acquisition. Therefore, from thereon the coil sensitivities were calculated only for the first phase-cycled image (-180°), which corresponded to a normal on-resonance bSSFP scan, and applied to the reconstructions for subsequent phase-cycled images. However, the map homogeneity still did not match that of the published results.

It was around the same time as the work above that it was verified that the code received from Yulia Shcherbakova matched the published algorithm (Section 3.5).

It was then found that the poor map homogeneity and "holes" were due to noise. In the context of PLANET, noise can cause a point on the elliptical signal model to cross the origin of the complex plane, leading to negative relaxation times; ellipses corresponding to neighbouring voxels yielded negative and positive relaxation times due to one point slightly crossing the origin. The effect of noise could be alleviated somewhat with smoothing with a Gaussian kernel or removed using a denoising reconstruction. Using a spatially-regularized denoising reconstruction, increasing the number of iterations improved convergence and removed more holes. A denoising reconstruction improved map homogeneity, accuracy, and precision, on the condition that the appropriate sequence parameters were used.

Increasing the voxel size improved PLANET map accuracy and precision, attributable to an increase in SNR (137), yet the quality of our maps still did not match that of the published maps. Much later, an experiment in which we doubled the number of slices also improved map homogeneity.

The published study used a brain coil that was more compact and should generate a more uniform receive field than the chest coils, used in cardiac scans, that we had been using up until then. We therefore scanned a phantom consisting of vials in a 64-channel brain coil, although this still did not improve the map quality to the published case.

Therefore, thinking that the sharp transitions present in a phantom may be less amenable to PLANET, we scanned the brain of a volunteer, which yielded adequate map quality.

Finally, it was in September 2019 that Dr van Heeswijk had the idea to use the lowest slew rate gradient setting, together with the 64-channel brain coil, since lower slew-rate gradients would reduce eddy current effects that could effect the steady-state signal. This yielded a map homogeneity that matched that of the published study using the same acquisition parameters (Figure 7).